HAL open science

An arsenic-driven pump for invisible gold in hydrothermal systems

G. S. Pokrovski, C. Escoda, M. Blanchard, Denis Testemale, Jean-Louis F Hazemann, S. Gouy, M. A. Kokh, M.-C. Boiron, F. de Parseval, T. Aigouy, et al.

To cite this version:

G. S. Pokrovski, C. Escoda, M. Blanchard, Denis Testemale, Jean-Louis F Hazemann, et al.. An arsenic-driven pump for invisible gold in hydrothermal systems. Geochemical Perspectives Letters, 2021, 17, pp.39-44. 10.7185/geochemlet.2112 . hal-03203427

HAL Id: hal-03203427

https://hal.science/hal-03203427v1

Submitted on 20 Apr 2021

HAL is a multi-disciplinary open access archive for the deposit and dissemination of scientific research documents, whether they are published or not. The documents may come from teaching and research institutions in France or abroad, or from public or private research centers.

L'archive ouverte pluridisciplinaire **HAL**, est destinée au dépôt et à la diffusion de documents scientifiques de niveau recherche, publiés ou non, émanant des établissements d'enseignement et de recherche français ou étrangers, des laboratoires publics ou privés.

Distributed under a Creative Commons Attribution - NoDerivatives 4.0 International License

Geochemical Perspectives Letters

© 2021 The Authors
Published by the European Association of Geochemistry

An arsenic-driven pump for invisible gold in hydrothermal systems

G.S. Pokrovski[1*], C. Escoda[1], M. Blanchard[1], D. Testemale[2], J.-L. Hazemann[2], S. Gouy[1], M.A. Kokh[1,8], M.-C. Boiron[3], F. de Parseval[1], T. Aigouy[1], L. Menjot[1], P. de Parseval[1], O. Proux[4], M. Rovezzi[4], D. Béziat[1], S. Salvi[1], K. Kouzmanov[5], T. Bartsch[6], R. Pöttgen[6], T. Doert[7]

OPEN ACCESS
doi: 10.7185/geochemlet.2112

Abstract

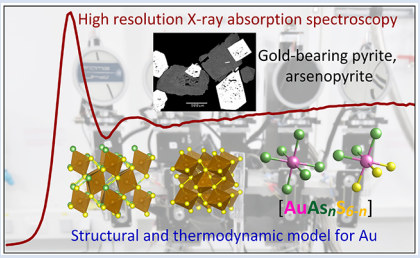

Pyrite (FeS_2), arsenopyrite (FeAsS) and löllingite ($FeAs_2$) are exceptional gold concentrators on Earth; yet the exact redox and structural state of this "invisible" gold and the forces driving its intake and release by these minerals remain highly controversial. Here we applied high resolution X-ray absorption spectroscopy to Au-bearing pyrite and iron sulfarsenides from hydrothermal deposits and their synthetic analogues. We show that Au preferentially enters octahedral Fe structural sites [Au(As,S)$_6$] enriched in As, by forming respectively [$AuAs_{1-3}S_{5-3}$], [$AuAs_3S_3$···$AuAs_6$] and [$AuAs_6$] atomic units in arsenian pyrite (>0.1–1.0 wt. % As), arsenopyrite and löllingite, implying a formal oxidation state of Au^{II} in the minerals. In contrast, in As-poor pyrite, Au is dominantly chemisorbed as [$Au^{I}S_2$] moieties in much lower concentrations. Combined with experimental data on Au mineral-fluid partitioning, our findings imply a universal control exerted by arsenic on gold incorporation in iron sulfides and sulfarsenides *via* coupled Au-As redox reactions. These reactions account for the observed variations in invisible gold contents in the minerals from different hydrothermal deposit types and enable quantitative prediction of iron sulfarsenide ability in controlling gold concentration and distribution in hydrothermal systems.

Received 18 December 2020 | Accepted 17 March 2021 | Published 20 April 2021

Introduction

Pyrite, arsenopyrite and löllingite are the key minerals in hydrothermal systems capable of concentrating gold by up to 10^6 times its mean crustal and mantle abundance (~1 ng/g). A large part of gold hosted by these minerals is "invisible" or "refractory" (*i.e.* optically undetectable) occurring both as metal nanoparticles (Au^0) and chemically bound Au, the latter being often the dominant gold state and commonly associated with arsenic on the (sub)micron scale (*e.g.*, Cathelineau *et al.*, 1989; Cook and Chryssoulis, 1990; Reich *et al.*, 2005). Thus, the redox and structural state of chemically bound Au and its link with As may define a deposit's economic potential (*e.g.*, Kusebauch *et al.*, 2019), determine the type and cost of Au recovery from ore (*e.g.*, Adams, 2005) and, more generally, affect the gold distribution at the Earth's crust scale (*e.g.*, Large *et al.*, 2011). Despite significant advances in micro/nanoanalytical techniques over the past 20 years, the fundamental causes of the Au-As relationship and processes that could drive gold, the most chemically inert metal of the Periodic Table, to such levels of enrichment in a host mineral yet remain enigmatic. Existing interpretations vary from the formation of aqueous Au-As complexes or Au^0 electrochemical deposition and $Au(HS)_2^-$ chemisorption on arsenian pyrite and arsenopyrite surfaces or precipitation of gold sulfide phases, to Au entering Fe, S or As crystallographic sites, along with other cation substitutions or structural vacancies, and with the formal oxidation state of chemically bound Au spanning from –1 to +3 and coordination from 2 to 6 (*e.g.*, Arehart *et al.*, 1993; Möller and Kersten, 1994; Simon *et al.*, 1999; Deditius *et al.*, 2014; Pokrovski *et al.*, 2019; Merkulova *et al.*, 2019; Filimonova *et al.*, 2020).

In an attempt to elucidate fundamental factors controlling the nature of invisible Au in arsenian pyrite and Fe sulfarsenides and the role played by As in Au intake, we used high energy resolution fluorescence detection X-ray absorption spectroscopy (HERFD-XAS), which is the most direct method to provide information about a trace element redox state, chemical bonding, and coordination at the atomic scale (*e.g.*, Proux *et al.*, 2017). Both X-ray absorption near-edge (XANES) and extended X-ray

[1] Géosciences Environnement Toulouse (GET), UMR 5563 CNRS, Université Paul Sabatier Toulouse III, IRD, CNES, Observatoire Midi-Pyrénées, 14 av. Edouard Belin, F-31400 Toulouse, France
[2] Université Grenoble Alpes, CNRS, Institut Néel, 25 av. des Martyrs, F-38042 Grenoble Cedex 9, France
[3] Université de Lorraine, CNRS, CREGU, F-54000 Nancy, France
[4] Université Grenoble Alpes, CNRS, IRD, Irstea, Météo France, OSUG, FAME, F-38000 Grenoble, France
[5] University of Geneva, Department of Earth Sciences, rue des Maraîchers 13, CH-1205, Geneva, Switzerland
[6] Institut für Anorganische und Analytische Chemie, Universität Münster, Corrensstraße 30, D-48149 Münster, Germany
[7] Technische Universität Dresden, Faculty of Chemistry and Food Chemistry, Helmholtzstraße 10, D-01062 Dresden, Germany
[8] Universität Potsdam, Institut für Geowissenschaften, Campus Golm, Haus 27, Karl-Liebknecht-Str. 24-25, D-14476 Potsdam, Germany
* Corresponding author (email: gleb.pokrovski@get.omp.eu; glebounet@gmail.com)

absorption fine structure (EXAFS) spectra were acquired on a set of thoroughly characterised Au-bearing pyrite and arsenopyrite samples from major metamorphic and sedimentary-hosted gold deposits and their synthetic analogues (including löllingite) prepared in controlled laboratory experiments (Supplementary Information). The obtained spectroscopic and fluid-mineral partitioning data were interpreted using quantum chemistry and thermodynamic approaches to generate a new structural and physico-chemical model that reveals the fundamental role played by arsenic in gold incorporation in pyrite and Fe sulfarsenides.

Atomic State of Gold from Spectroscopic Data

XANES spectra of chemically bound gold in all natural and synthetic arsenopyrite, löllingite and As-rich pyrite (≥1 wt. % As) samples examined here significantly differ from those of metallic Au^0 and other reference compounds in which Au is coordinated by 2 to 4 As/S/Cl atoms or by 6 Sb/Te atoms, implying a different Au local environment in sulfarsenides (Figs. 1, S-6). In contrast, spectra of As-poor pyrites (<0.1 wt. % As) display distinctly lower energy and amplitudes that indicate a lower Au coordination and/or different electronic configuration than in more As-enriched samples. Quantum chemistry simulated XANES spectra of various Au positions in the mineral structure (Supplementary Information) show that Au enters $(Au,Fe)(As,S)_6$ octahedral sites variably enriched in As (Fig. 2). For löllingite, the measured spectra are perfectly matched by a simulated one for the $AuAs_6$ site. For arsenopyrite, the spectra are consistent with $AuAs_3S_3$-$AuAs_6$ units, rather than simple Au-to-Fe substitution in a stoichiometric $FeAs_3S_3$ site (Fig. S-8). These interpretations are fully supported by EXAFS analyses that yield 6 ± 1 As atoms at 2.53 ± 0.01 Å bound to Au in löllingite, and 4.5 ± 0.5 As at 2.51 ± 0.02 Å plus 1.5 ± 0.5 S atoms at 2.42 ± 0.05 Å in arsenopyrite (Table S-4). The remarkable similarity of bound Au atomic environment among all natural and synthetic arsenopyrite samples from various geological settings and experimental conditions demonstrates the universality of the Au substitution mechanism. For arsenian pyrites studied here, both XANES and EXAFS data (Figs. 2, S-9) demonstrate Au to be in an As-enriched Fe site, $AuAs_3S_3$. In contrast, for As-poor pyrite, spectra indicate quasi-linear AuS_2 geometries, which are typical of Au^I aqueous (poly)sulfide species and most thiol and sulfide solids (Pokrovski *et al.*, 2015, 2019). The difference in Au atomic environment between As-poor pyrite on one hand and arsenian pyrite, arsenopyrite and löllingite on the other hand is strong evidence that As directly impacts the mode of Au incorporation.

Structural Model for Chemically Bound Gold in Pyrite and Iron Sulfarsenides

Our spectroscopic results combined with available data are consistent with the structural model shown in Figure 3. The degree of Au enrichment in pyrite generally depends on As content, being the lowest in As-poor pyrite and increasing with As content, as demonstrated by the large body of micro-to-nano scale analyses of Au and As concentrations in the mineral (Reich *et al.*, 2005; Deditius *et al.*, 2014), and also directly evidenced by our and recent experiments (Kusebauch *et al.*, 2019). In As-poor pyrite, Au is dominantly surface-chemisorbed as Au^I (poly)sulfide clusters that may be partly incorporated into structural defects and dislocations depending on crystal growth kinetics (*e.g.*, Wu *et al.*, 2019), and partly expulsed as Au^0 nanoparticles due to the very limited capacity of pyrite to intake Au in the absence of As (Pokrovski *et al.*, 2019). The pronounced change

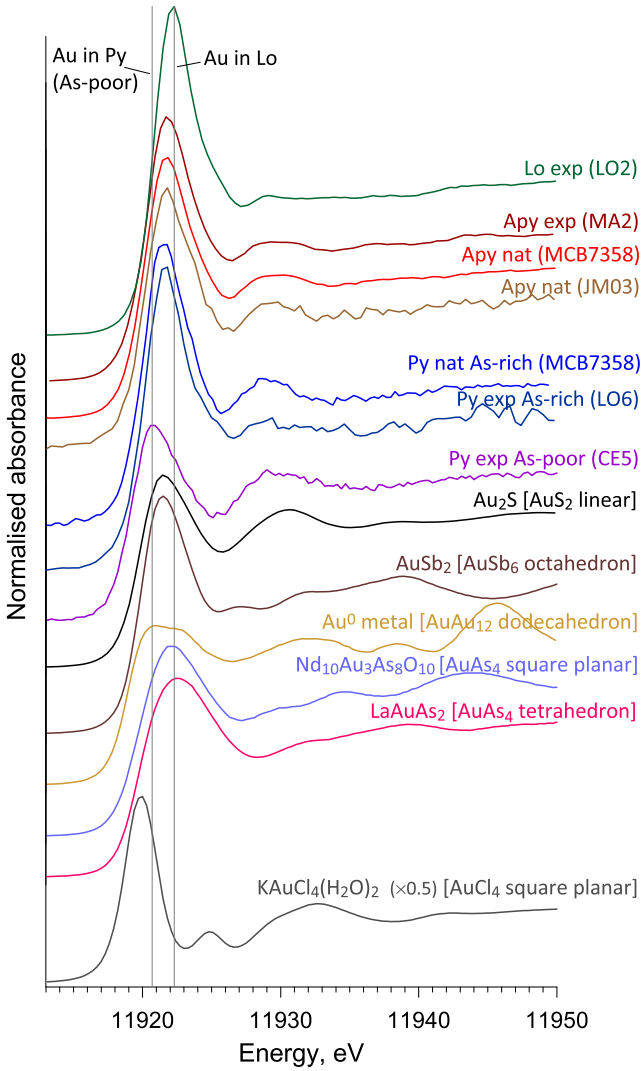

Figure 1 Gold L_3-edge HERFD XANES spectra (offset vertically) of representative Au-bearing natural (nat) and experimental (exp) pyrite (Py), arsenopyrite (Apy) and löllingite (Lo) samples, and selected reference compounds with indicated Au first shell atomic coordination (see Supplementary Information for details).

in the Au solubility pattern with increasing As content above 0.01–0.1 wt. % As (Fig. 3), as documented in many natural studies, implies a fundamental change in the gold intake mechanism to increased Au partitioning into As-enriched $Fe(As,S)_6$ sites compared to the pyrite FeS_6 crystallographic site, as evidenced by the direct detection of As in the Au nearest atomic shell (Figs. 2, S-9). The number of As atoms bound to Au (n) may display large variability, from below detection limit ($n < 1$) to $n \geq 3$, as reported in recent XAS studies of some natural and synthetic pyrites with >1 wt. % As (Merkulova *et al.*, 2019; Filimonova *et al.*, 2020). Thus, Au in arsenian pyrite is likely to exhibit a range of $Au(As_nS_{6-n})$ environments, from S-rich ($n \leq 1$) to As-rich ($n \geq 3$). This trend is followed by the continued enhancement of Au binding to As in arsenopyrite and löllingite ($n > 4$; Fig. 3). Formation of Au chemical bonds with As^{-I}, which is the dominant As redox state in the three minerals in most settings, provides a fundamental explanation for the systematically higher invisible Au contents analysed at the micron scale in arsenopyrite and löllingite compared to coexisting pyrite in many hydrothermal deposits (Tables S-3, S-11), as well as for experimentally measured very high Au partition coefficients between iron sulfarsenides and aqueous fluid (>10^5; Table S-8).

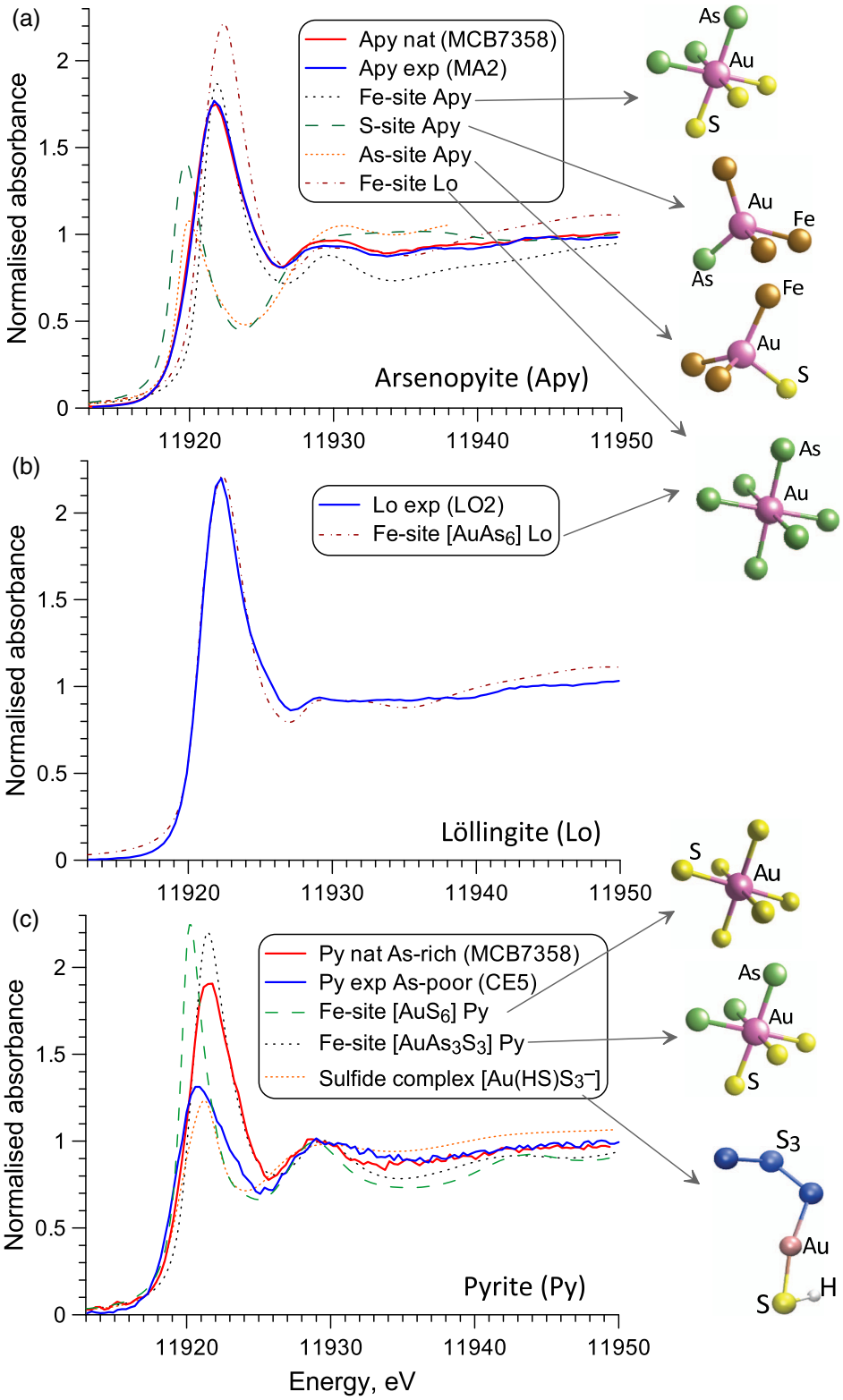

Figure 2 Comparison of Au L_3-edge HERFD XANES spectra of representative samples with quantum chemistry simulated spectra of Au in different structural sites as pictured by the displayed atomic clusters. The spectra of **(a)** Apy, **(b)** Lo, and **(c)** As-rich Py are consistent with Au in an As-enriched $[Au(As,S)_6]$ octahedral site, whereas Au in As-poor Py **(c)** is in $[AuS_2]$ moieties similar to those in exemplified Au^I-(poly)sulfide complexes.

The available XAS data on natural pyrite and arsenopyrite samples do not reveal atoms other than As or S in the Au nearest shell that might accompany Au incorporation. Thus, direct Au^{II} to Fe^{II} substitution favoured by As^{-I} would be a universal mechanism that does not require specific structural vacancies or charge compensations from other minor elements in different redox states (Cu^I, Sb^{III}, Fe^{III}, As^{III}). Although the notion of redox state for strongly covalent bonds such as Au-As or Au-S has no strict sense (Cabri *et al.*, 2000), the formal Au^{II} state would be consistent with the three key features of gold coordination chemistry: i) the great majority of formally Au^I and Au^{III} compounds have either 2 (linear) or 4 (square/tetrahedral) Au coordination

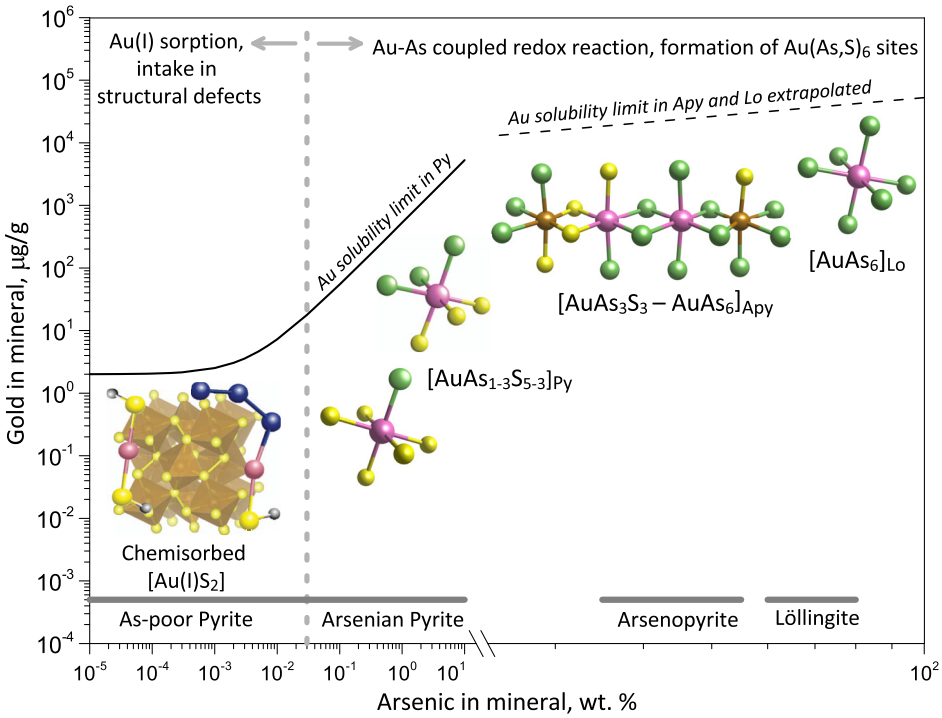

Figure 3 Structural model for chemically bound Au in pyrite, arsenopyrite and löllingite (not to scale). The Au coordination is shown by ball-and-stick atomic clusters (Au = pink, S = yellow, As = green, Fe = brown, S_3 = blue, H = grey). Horizontal gray bars indicate the typical range of As contents in each mineral. Empirical Au solubility limit in arsenian pyrite (solid curve; Reich *et al.*, 2005) was extrapolated to Apy and Lo (dashed curve). Note a fundamental transition in the Au incorporation mechanism (vertical dashed line, indicative position), from chemisorption as Au^{I}-polysulfide complexes at low As content in pyrite to coupled Au-As redox reactions driving Au entry in As-enriched Fe crystallographic sites of the three minerals.

(Cotton and Wilkinson, 1988) poorly compatible with an octahedral site, ii) complexes of Au^{II} coordinated by 4 to 6 ligands (S, P, Se), and often paralleled by [Au···Au] clustering as found in arsenopyrite in this study (Fig. S-8), are well known in chemistry (Laguna and Laguna, 1999), iii) gold in many arsenide and chalcogenide compounds ($AuAs_2$, $AuSb_2$, $AuTe_2$, AuSe) has a formal oxidation state of Au^{II} and a coordination of 6 (ICSD, 2020). Therefore, the favourable coordination geometry coupled with redox-driven Au binding to As are the two key requirements allowing Au enrichment in iron sulfarsenides. These key features distinguish these minerals from other hydrothermal sulfides such as pyrrhotite, chalcopyrite, bornite, or sulfosalts that host very little invisible Au (*e.g.*, George *et al.*, 2017, 2018).

Thermodynamic Model for Gold Solubility in Arsenopyrite and Löllingite

Gold incorporation in iron sulfarsenides may thus be interpreted as a coupled redox reaction between the dominant Au^{I}/As^{III} redox states in the hydrothermal fluid and Au^{II}/As^{-I} in the mineral. Because Au in arsenopyrite occurs in a combination of arsenopyrite and löllingite-type sites (Fig. 3), Au solubility and partitioning may be formally approximated by a hypothetical sulfarsenide end member AuAsS-$AuAs_2$ (equivalent to $AuAs_{1.5}S_{0.5}$) "dissolved" in arsenopyrite:

$$Au(HS)_2^- + H^+ + 1.5\,As(OH)_3 = [AuAs_{1.5}S_{0.5}]_{Apy} + 1.125\,O_2 + 1.5\,H_2S + 2.25\,H_2O \quad \text{(Eq. 1)}$$

$$Au^0(\text{metal}) + 1.5\,As(OH)_3 + 0.5\,H_2S = [AuAs_{1.5}S_{0.5}]_{Apy} + 0.875\,O_2 + 2.75\,H_2O \quad \text{(Eq. 2)}$$

where $[AuAs_{1.5}S_{0.5}]_{Apy}$ is the mole fraction of the Au-sulfarsenide end member in the arsenopyrite solid solution, and $Au(HS)_2^-$ and $As(OH)_3$ are the activities of the major Au and As aqueous species in the fluid (Perfetti *et al.*, 2008; Pokrovski *et al.*, 2015). The thermodynamic constants of reactions (Eq. 1) and (Eq. 2), derived from experimental mineral-fluid partition coefficients at 450 °C and 700 bar are $\log_{10}K_1 = -18.2 \pm 0.3$ and $\log_{10}K_2 = -22.4 \pm 0.3$, respectively (1 s.d.; Table S-9). An analogous model of the $AuAs_2$-$FeAs_2$ solid solution is valid for löllingite (Table S-10). The generated constants enable, for the first time, direct predictions of Au mineral-fluid partitioning and solubility in sulfarsenides as a function of the key hydrothermal fluid parameters such as As/S content, redox and pH (Fig. 4). Applying similar quantitative models to pyrite would require more systematic experimental and natural data to account for the large range in the $Au(As_nS_{6-n})$ site stoichiometry (Fig. 3). The empirical gold solubility limit reported for arsenian pyrite is likely to be defined by reactions analogous to (Eq. 1) and (Eq. 2), thereby reflecting the natural variability limits of the fluid parameters.

Implications

Our new findings help to clarify one of the oldest enigmas of geochemistry about the unique role played by arsenic in Au fate in hydrothermal systems. Our results demonstrate that both arsenopyrite and löllingite are capable of accommodating large concentrations of bound Au (100s to 1000s µg/g) even from Au-poor fluids (<0.1 µg/g Au) in relatively reduced metamorphic and ultramafic rock settings (f_{O_2} < NNO; Fig. 4a), whereas in more oxidised orogenic- and porphyry-related systems little Au is incorporated, in full agreement with natural observations (*e.g.*, Deditius *et al.*, 2014). Our quantitative predictions are currently limited at 450 °C, but lower temperatures may further

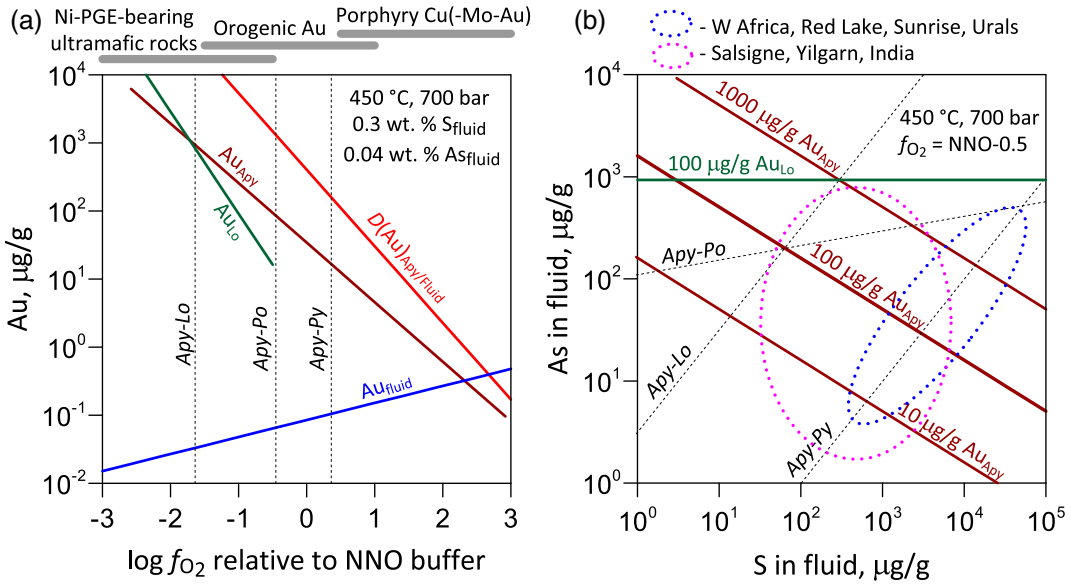

Figure 4 Gold solubility in arsenopyrite (Apy) and löllingite (Lo) in equilibrium with hydrothermal fluid and native gold, predicted as a function of **(a)** log f_{O2} (in bars, relative to the nickel-nickel oxide O_2 buffer, NNO) at typical H_2S and $As(OH)_3$ fluid phase concentrations for the indicated major types of gold deposits, and **(b)** As and S fluid phase content at f_{O2} of NNO–0.5 within the Apy stability domain (Perfetti *et al.*, 2008) in metamorphic gold deposits (circles; Table S-11 for compilation). Also plotted are equilibrium $Au(HS)_2^-$ concentrations in fluid (blue curve), Au Apy/Fluid partition coefficient ($D(Au)_{Apy/Fluid}$, mass units ratio, same y scale, red curve), and Apy-Lo, Apy-pyrrhotite (Po), and Apy-pyrite (Py) equilibrium lines.

favour Au-As redox reactions and Au intake in sulfarsenides, consistent with enhanced equilibrium As partitioning into pyrite (Xing *et al.*, 2019). Surface sorption and mineral growth rate factors may also contribute to Au scavenging (*e.g.*, Wu *et al.*, 2019), but the fundamental arsenic-driven redox control will equally hold. Changes in redox, pH and dissolved As/S contents upon fluid evolution adequately account for the large variability of Au content widely documented in different mineral generations within individual deposits and across mineralised domains in different deposit types (Fig. 4b). Gold intake by and release from sulfarsenides driven by variations in fluid composition appear to be key factors for hydrothermal gold deposit formation. For example, in giant Carlin-type deposits, these factors may have driven focused coupled Au and As-pyrite deposition (Kusebauch *et al.*, 2019). In orogenic-type deposits, first order Au "pumping" from the fluid by pyrite and arsenopyrite, followed by large scale Au liberation from those minerals during further metamorphism, may have provided a gold source and strongly influenced metal endowment, timing of mineralisation, and spatial distribution (Large *et al.*, 2011; Velásquez *et al.*, 2014; Fougerouse *et al.*, 2016). Future advances of *in situ* spectroscopy will offer more systematic quantification of invisible gold along with other valuable trace metals hidden in iron sulfarsenide minerals, thereby enabling a better understanding of trace element geochemical cycles and improving resource assessment, exploration and recovery.

Acknowledgments

This work was funded by the French National Research Agency (RadicalS ANR-16-CE31-0017, SOUMET ANR-2011-Blanc-SIMI-5-6-009), the Institut des Sciences de l'Univers of the Centre National de la Recherche Scientifique, INSU-CNRS (CESSUR-OrPy-AsOrPy), the Institut Carnot ISIFoR (OrPet), and the West African Exploration Initiative (WAXI-P934A). We acknowledge the European Synchrotron Radiation Facility (ESRF) for providing access to beam time and infrastructure, and AMIRA International for support in field-related aspects. The FAME-UHD project is supported by the French Grand Emprunt EquipEx (EcoX ANR-10-EQPX-27-01), the CEA-CNRS CRG consortium and the INSU-CNRS. DFT calculations were performed using HPC resources from CALMIP (2020-P1037). We thank A.-M. Cousin for invaluable help with figure layout, S. Foulon for tube welding, A. Manceau and B. Tagirov for sharing XAS data and references, and Y. Joly for advice on XANES modeling. Comments by Editor S. Redfern and an anonymous referee greatly improved this article.

Editor: Simon Redfern

Additional Information

Supplementary Information accompanies this letter at https://www.geochemicalperspectivesletters.org/article2112.

© 2021 The Authors. This work is distributed under the Creative Commons Attribution Non-Commercial No-Derivatives 4.0 License, which permits unrestricted distribution provided the original author and source are credited. The material may not be adapted (remixed, transformed or built upon) or used for commercial purposes without written permission from the author. Additional information is available at https://www.geochemicalperspectivesletters.org/copyright-and-permissions.

Cite this letter as: Pokrovski, G.S., Escoda, C., Blanchard, M., Testemale, D., Hazemann, J.-L., Gouy, S., Kokh, M.A., Boiron, M.-C., de Parseval, F., Aigouy, T., Menjot, L., de Parseval, P., Proux, O., Rovezzi, M., Béziat, D., Salvi, S., Kouzmanov, K., Bartsch, T., Pöttgen, R., Doert, T. (2021) An arsenic-driven pump for invisible gold in hydrothermal systems. *Geochem. Persp. Let.* 17, 39–44.

References

Adams, M.D. (Ed.) (2005) *Advances in Gold Ore Processing*. Elsevier Science, Amsterdam.

Arehart, G.B., Chryssoulis, S.L., Kesler, S.E. (1993) Gold and arsenic in iron sulfides from sediment-hosted disseminated gold deposits: Implication for depositional processes. *Economic Geology* 88, 171–185.

Cabri, L.J., Newville, M., Gordon, R.A., Crozier, E.D., Sutton, S.R., McMahon, G., Jiang, D.-T. (2000) Chemical speciation of gold in arsenopyrite. *Canadian Mineralogist* 38, 1265–1281.

Cathelineau, M., Boiron, M.-C., Holliger, P., Marion, P., Denis, M. (1989) Gold in arsenopyrites: Crystal chemistry, location and state, physical and chemical conditions of deposition. *Economic Geology Monograph* 6, 328–341.

Cook, N.J., Chryssoulis, S.L. (1990) Concentrations of "invisible" gold in the common sulfides. *Canadian Mineralogist* 28, 1–16.

Cotton, A.F., Wilkinson, G. (1988) *Advanced Inorganic Chemistry*. Fifth Edition, Wiley, New York.

Deditius, A.P., Reich, M., Kesler, S.E., Utsunomiya, S., Walshe, J., Chryssoulis, S.L., Ewing, R.C. (2014) The coupled geochemistry of Au and As in pyrite from hydrothermal deposits. *Geochimica et Cosmochimica Acta* 140, 644–670.

Filimonova, O.N., Tagirov, B.R., Trigub, A.L., Nickolsky, M.S., Rovezzi, M., Belogub, E.V., Reukov, V.L., Vikentiev, I.A. (2020) The state of Au and As in pyrite studied by X-ray absorption spectroscopy of natural minerals and synthetic phases. *Ore Geology Reviews* 121, 103475.

Fougerouse, D., Micklethwaite, S., Tomkins, A.G., Mei, Y., Kilburn, M., Guagliardo, P., Fisher, L.A., Halfpenny, A., Gee, M., Paterson, D., Howard, D.L. (2016) Gold remobilisation and formation of high grade ore shoots driven by dissolution-reprecipitation replacement and Ni substitution into auriferous arsenopyrite. *Geochimica et Cosmochimica Acta* 178, 143–159.

George, L.L., Cook, N.J., Ciobanu, C.L. (2017) Minor and trace elements in natural tetrahedrite-tennantite: Effects of element partitioning among base metal sulphides. *Minerals* 7, 17.

George, L.L., Cook, N.J., Crowe, B.B.P., Ciobanu, C.L. (2018) Trace elements in hydrothermal chalcopyrite. *Mineralogical Magazine* 82, 59–88.

ICSD (2020) *Inorganic Crystal Structure Database*. ICSD, FIZ Karlsruhe. https://icsd.products.fiz-karlsruhe.de, accessed 2 April 2021.

Kusebauch, C., Gleeson, S.A., Oelze, M. (2019) Coupled partitioning of Au and As into pyrite controls the formation of giant Au deposits. *Science Advances* 5, eaav5891.

Laguna, A., Laguna, M. (1999) Coordination chemistry of gold(II) complexes. *Coordination Chemistry Reviews* 193–195, 837–856.

Large, R.R., Bull, S.W., Maslennikov, V.V. (2011) A carbonaceous sedimentary source-rock model for Carlin-type and orogenic gold deposits. *Economic Geology* 106, 331–358.

Merkulova, M., Mathon, O., Glatzel, P., Rovezzi, M., Batanova, V., Marion, P., Boiron, M.-C., Manceau, A. (2019) Revealing the chemical form of "invisible" gold in natural arsenian pyrite and arsenopyrite with high energy-resolution X-ray absorption spectroscopy: *ACS Earth Space Chemistry* 3, 1905–1914.

Möller, P., Kersten, G. (1994) Electrochemical accumulation of visible gold on pyrite and arsenopyrite surfaces. *Mineralium Deposita* 29, 404–413.

Perfetti, E., Pokrovski, G.S., Ballerat-Busserolles, K., Majer, V., Gibert, F. (2008) Densities and heat capacities of aqueous arsenious and arsenic acid solutions to 350 °C and 300 bar, and revised thermodynamic properties of $As(OH)_3^0$(aq), $AsO(OH)_3^0$(aq) and iron sulfarsenide minerals. *Geochimica et Cosmochimica Acta* 72, 713–731.

Pokrovski, G.S., Kokh, M.A., Guillaume, D., Borisova, A.Y., Gisquet, P., Hazemann, J.-L., Lahera, E., Del Net, W., Proux, O., Testemale, D., Haigis, V., Jonchière, R., Seitsonen, A.P., Ferlat, G., Vuilleumier, R., Saitta, A.M., Boiron, M.-C., Dubessy, J. (2015) Sulfur radical species form gold deposits on Earth. *Proceedings of the National Academy of Sciences* 112, 13484–13489.

Pokrovski, G.S., Kokh, M.A., Proux, O., Hazemann, J.-L., Bazarkina, E.F., Testemale, D., Escoda, C., Boiron, M.-C., Blanchard, M., Ajgouy, T., Gouy, S., de Parseval, P., Thibaut, M. (2019) The nature and partitioning of invisible gold in the pyrite-fluid system. *Ore Geology Reviews* 109, 545–563.

Proux, O., Lahera, E., Del Net, W., Kieffer, I., Rovezzi, M., Testemale, D., Irar, M., Thomas, S., Aguilar-Tapia, A., Bazarkina, E.F., Prat, A., Tella, M., Auffan, M., Rose, J., Hazemann, J.-L. (2017) High energy resolution fluorescence detected X-ray absorption spectroscopy: a new powerful structural tool in environmental biogeochemistry sciences. *Journal of Environmental Quality* 46, 1146–1157.

Reich, M., Kesler, S.E., Utsunomiya, S., Palenik, C.S., Chryssoulis, S.L., Ewing, R.C. (2005) Solubility of gold in arsenian pyrite. *Geochimica et Cosmochimica Acta* 69, 2781–2796.

Simon, G., Huang, H., Penner-Hahn, J.E., Kesler, S.E., Kao, L.-S. (1999) Oxidation state of gold and arsenic in gold-bearing arsenian pyrite. *American Mineralogist* 84, 1071–1079.

Velásquez, G., Béziat, D., Salvi, S., Siebenaller, L., Borisova, A.Y., Pokrovski, G.S., de Parseval, P. (2014) Formation and deformation of pyrite and implications for gold mineralization at the El Callao mining district, Venezuela. *Economic Geology* 109, 457–486.

Wu, Y.-F., Fougerouse, D., Evans, K., Reddy, S.M., Saxey, D.W., Guagliardo, P., Li, J.-W. (2019) Gold, arsenic, and copper zoning in pyrite: A record of fluid chemistry and growth kinetics. *Geology* 47, 641–644.

Xing, Y., Brugger, J., Tomkins, A., Shvarov, Y.V. (2019) Arsenic evolution as a tool for understanding formation of pyritic gold ores. *Geology* 47, 335–338.

Geochemical Perspectives Letters

© 2021 The Authors
Published by the European Association of Geochemistry

An arsenic-driven pump for invisible gold in hydrothermal systems

G.S. Pokrovski, C. Escoda, M. Blanchard, D. Testemale, J.-L. Hazemann, S. Gouy, M.A. Kokh, M.-C. Boiron, F. de Parseval, T. Aigouy, L. Menjot, P. de Parseval, O. Proux, M. Rovezzi, D. Béziat, S. Salvi, K. Kouzmanov, T. Bartsch, R. Pöttgen, T. Doert

Supplementary Information

The Supplementary Information includes:

- 1. Materials: Description of Experimental and Natural Sulfarsenide Samples
- 2. Methods: Analytical, Spectroscopic and Theoretical Methods
- 3. Supplementary Text: Additional Notes on Thermodynamic Approaches
- Tables S-1 to S-11
- Figures S-1 to S-12
- Supplementary Information References

1. Materials: Description of Experimental and Natural Sulfarsenide Samples

1.1. Experimental samples

Three types of experiments at controlled laboratory conditions have been performed to produce synthetic Au-bearing sulfarsenide minerals (Tables S-1, S-2). Two hydrothermal types (MA, CE and LO series, Table S-1) in the presence of aqueous solution were conducted at temperature (*T*) of 450 °C and pressures (*P*) of 700–750 bar. The choice of these *T-P* parameters for hydrothermal MA, CE et LO series is dictated by the following reasons: *i)* they the pertinent to *T-P* conditions of hydrothermal ore deposits hosting sulfarsenide minerals in the Earth's crust (~150–600 °C and <5 kbar) being roughly in the middle of the typical *T-P* window for magmatic porphyry Cu-Mo-Au and metamorphic Au ore deposits (*e.g.*, Goldfarb *et al.*, 2005; Kouzmanov and Pokrovski, 2012; Kolb *et al.*, 2015; references therein); *ii)* the experimental *T* is sufficiently high to allow efficient chemical transfer and to reach fluid-mineral and mineral-mineral equilibrium within the intrinsically limited duration of laboratory experiments; and *iii)* the thermodynamic properties and related equations of state for aqueous and mineral species at these *T-P* conditions are sufficiently well constrained to date (see section 2.6 in this document) to enable thermodynamic validation of the Au speciation model proposed here. The third type (SF series, Table S-2) was conducted in a water-free system at 600 °C and pressures of <10 bar, following standard protocols of high-temperature 'dry' mineral synthesis widely used for sulfide minerals, to check whether the state of chemically bound gold would be the same as that in the presence of hydrothermal fluid.

The first type of synthesis, hereafter called *gold-capsule experiments*, of most arsenopyrite (Apy) and löllingite (Lo) and some pyrite (Py) samples (MA and LO series, Table S-1) was based on the following formal reactions in aqueous solution:

$Fe_2O_3 + 4\ As + 2\ S = 2\ FeAsS\ (Apy) + As_2O_3$ (Eq. S-1)

$Fe_2O_3 + 6\ As = 2\ FeAs_2\ (Lo) + As_2O_3$ (Eq. S-2)

$FeS + As = FeAsS\ (Apy)$ (Eq. S-3)

$Fe + 2\ As = FeAs_2\ (Lo)$ (Eq. S-4)

$FeS + >0.9\ S + <0.1\ As \approx FeS_{>1.9}As_{<0.1}\ (Py)$ (Eq. S-5)

Reactions (S-1) and (S-2), inspired from Wu and Delbove (1989) who succeeded to hydrothermally synthesise Au-rich arsenopyrite crystals hosting up to 17,000 ppm Au at 500 °C and 2 kbar, correspond to oxidizing conditions with high As^{III} and low S^{-II} activity in solution. In contrast, more direct reactions (S-3) and (S-4), correspond to more reducing conditions with lower As^{III} and/or higher S^{-II} activity, as demonstrated by thermodynamic modeling (Tables S-8 to S-10). The chosen reactions thus provide contrasting conditions in terms of oxygen fugacity, arsenic and sulfur activity and redox and the resulting gold solubility at equilibrium, but do yield the same thermodynamically stable arsenopyrite or löllingite phase. A couple of arsenian pyrite samples were also synthesised in this type of experiments based on reaction (S-5).

Experiments were conducted in gold capsules (4 mm i.d., 4.4 mm o.d., 40 mm length), which were loaded with a ground mixture of reagent-grade powders of Fe_2O_3, FeS, As, Fe, and S (all >98 % purity, Sigma Aldrich) in the corresponding proportions matching the reaction stoichiometry and a 2 molal (mol/kg H_2O) NaCl or NaOH aqueous solution, yielding a high solid/fluid mass ratio (~1:1), allowing efficient fluid-mineral equilibration, further favoured by the small sample chamber volume. The capsules were then welded shut and put in a titanium batch reactor, filled with water as a pressure medium (estimated by the degree of filling and *PVT* properties of H_2O) and placed in a temperature controlled (±1 °C) oven. At the end of the run lasting respectively 30 and 73 to 81 days for the MA and LO series, the

reactor was cooled down in water for 15 min, the capsules were opened and the solids were recovered, washed with hot water to remove precipitated salt and As_2O_3, dried at 50 °C and analysed as described in section 2. The quenched fluid phase could not be systematically recovered owing to its too small amounts (<0.1 mL) and partial loss during the capsule opening.

The second type of hydrothermal synthesis, hereafter *batch-reactor experiments* (CE series), also conducted at 450 °C and ~700 bar, used titanium-alloy batch reactors of ~20 mL volume whose design and handling are described in detail elsewhere (Pokrovski *et al*., 2002a, 2019). This type of synthesis is based on reaction (S-3) for arsenopyrite, whereas for pyrite the starting solid was FeS_2 that was directly reacted with a gold-bearing sulfidic solution with or without dissolved arsenic:

$$FeS_2 + <0.05\ As(OH)_3(aq) \approx FeS_{>1.95}As_{<0.05} \quad \text{(Eq. S-6)}$$

Compared to the gold-capsule experiments above, this type of synthesis enables accurate recovery and analyses of both solid and fluid phase, due to larger amounts of reagents and higher fluid/solid ratios (~10:1), but inevitably generates a lesser amount of data points. A weighed piece of gold foil (99.99 % purity, Heraeus) was attached to a titanium container suspended in the upper part of the reactor. A weighed amount of iron(II) disulfide (FeS_2, 325 mesh, 99.8 % trace metals basis, Sigma Aldrich) for Py runs, or a stoichiometric 1:1 mixture of ground reagent-grade powders of FeS and As for Apy runs, was placed into the container, avoiding direct contact with the gold foil. The reactor was then loaded with a weighed amount of aqueous potassium thiosulfate solution with or without arsenious acid $As(OH)_3$ (for Py runs) or with aqueous NaCl-HCl solution with addition of native sulfur to favour Au solubility (for Apy runs). These solution compositions were carefully chosen based on our previous experience (Pokrovski *et al.*, 2019) and using thermodynamic modeling (see section 2.6) to ensure the stability of the dominant target phase in the experiment (Py or Apy) and, in the case of Py runs, large Au solubility due to the presence of both reduced and oxidised sulfur generated by thiosulfate breakdown (*e.g.*, Pokrovski *et al.*, 2015), to promote more efficient exchange of Au-bearing fluid with the preexisting FeS_2. The reactors were placed in an oven; the pressure at the run temperature (±1 °C) was estimated from the degree of filling of the reactor (which is equivalent of the fluid density at experimental *T-P*) and the *T-P-X*-density properties of the well-known NaCl-H_2O system (Driesner and Heinrich, 2007). These pressure estimations have an uncertainty of less than ±50 bar at 450 °C and total *P* value of 700 bar at our solution compositions (*e.g.*, Pokrovski *et al.*, 2009a). The run duration was up to 20 days for most experiments, which was considered long enough to attain the solid-fluid chemical equilibrium as shown by extensive previous experiments on Au solubility (Pokrovski *et al*., 2009a, 2015, 2019). At the end of the experiment, the reactor was placed in cold water, resulting in a fast separation of the container with the solid phase from the fluid that almost immediately condensed into liquid in the lower part of the reactor thus avoiding eventual fluid-solid reverse reactions during further cooling. The reactor was then cooled for 20 min, unloaded, and washed 3 times with hot aqua regia to remove all gold that was dissolved in the fluid at the run temperature but may partly have precipitated on reactor walls during cooling. The resulting washout solution was treated and analysed for Au. The solid phase was rinsed with water to remove traces of salt and dried at 50 °C.

A third type of Apy and Py synthesis in a *water-free system* (SF series) was based on the reactions:

$$Fe + As + S = FeAsS\ (Apy) \quad \text{(Eq. S-7)}$$

$$Fe + >1.9\ S + <0.1\ As \approx FeS_{>1.9}As_{<0.1}\ (Py) \quad \text{(Eq. S-8)}$$

This type of experiment that follows classical procedures of high-temperature mineral synthesis, has been performed at 600 °C in vacuumed flame-sealed fused silica tubes loaded with a piece of gold metal foil and ground mixtures of elemental Fe, As and S (purity >99 %, Sigma) in corresponding proportions (Table S-2) and a 1:1 NaCl-$AlCl_3$ salt mixture as the fluxing reagent with a melting temperature of <500 °C. After 7 to 17 days from the experiment start, the tube was quenched in air, cut, and the solids were recovered and carefully washed with water to remove the salt and dried at 50 °C.

The three methods of synthesis yielded well-crystalline fine-grained arsenopyrite, löllingite or pyrite as the major mineral phase with, in some cases, microscopic metallic gold particles and some minor impurities (<5 % of volume) of FeS, AsS, and salts (NaCl, As_2O_3), depending on the experiment, most of them likely having precipitated on cooling (Fig. S-1, Tables S-1, S-2). These minor phases did not contain detectable invisible Au, which was all hosted by the Py, Apy or Lo phases as demonstrated by the analyses.

1.2. Natural samples

Three natural Au-bearing arsenopyrite and two arsenian pyrite samples were examined in this study (Table S-3, Fig. S-2).

Arsenopyrite and pyrite samples, MCB7358-Apy and MCB7358-Py, are from the Villeranges metamorphic gold deposit, Massif Central, France (Boiron *et al.,* 1989, and references therein) taken from the same mineral assemblage in a quartz-ankerite vein in tuff representative of the main ore mineralization stage (Fig. S-2a). Hydrothermal fluids operating at this stage at temperatures of 150-200 °C and redox conditions between the conventional NNO (nickel-nickel oxide) and HM (hematite-magnetite) buffers were low-saline and possibly slightly acidic. Euhedral pyrite and arsenopyrite crystals in ore are zoned, with uneven Au distribution, but typically with ~10 times more Au in Apy than in the coexisting Py (Table S-3). Invisible gold is present exclusively in a chemical bound state in both minerals as shown by Mössbauer spectroscopy, even though the exact Au redox and structural position could not be constrained (Marion *et al*., 1986). Detailed analyses of this (see below) and previous (Boiron *et al*., 1989) studies showed that this and other arsenopyrite samples from this deposit are generally slightly depleted in As (by ~1 to 3 at. %) compared to the stoichiometric As/S ratio of 1:1. Gold concentrations ranged from about 200 to 4000 ppm (mean = 2000 ± 1600 ppm, ±1 s.d.). Antimony was the only significant minor element with concentrations comparable to Au in the Apy sample studied here (up to 5000 ppm Sb). The coexisting Py sample had Au contents ranging from ~2 to 120 ppm (mean = 46 ± 33 ppm) and positively correlating with As contents, which ranged from 0.3 to 4 wt. % (mean = 2.6 ± 0.8 wt. %)[1]. Other trace elements detected by LA-ICPMS analyses were typically in the range 10–100 ppm (Cu, Ag, Co, Ni, Pb, Bi) and showed no correlation with Au.

Arsenopyrite samples MW15 and JM03 (Fig. 2b-d) are from the West African Craton orogenic gold deposits Tabakoroni (Mali) and Buesichem (Ghana), respectively, described in detail elsewhere (Olson *et al.,* 1992; Allibone *et al.,* 2002; Parra-Avila *et al.,* 2015; Ballo *et al.,* 2016; Traoré *et al.,* 2016). Sample MW15 is from an arsenopyrite-pyrite-carbonate-quartz dissemination in mineralised metabasalt (Fig. S-2b). Gold contents attain a maximum of 176 ppm in arsenopyrite (with a formal average of 58 ± 56 ppm in the sample examined here) and 38 ppm in coexisting pyrite (not studied here) and show relatively smooth LA-ICPMS transient signals attesting the absence of >0.1 µm gold particles (Traoré *et al.,* 2016). Sample JM03 is from a quartz-carbonate vein hosted by black shale (Fig. S-2c,d), with Au concentrations from 150 to 600 ppm as found in LA-ICPMS spots (mean = 270 ± 160 ppm). Both samples are S-enriched and As-depleted (by ~3 at. %) compared to the stoichiometric 1:1 value. Mineralizing fluids in both deposits likely corresponded to *T-P* conditions of greenschist facies metamorphism (300–500 °C, <8 kbar).

Pyrite sample KK03 is from the Gold Strike Carlin-type gold deposit from the Northern Carlin trend, Nevada, USA (Muntean, 2018, and references therein). The pyrite-bearing rock is a carbonaceous shale comprised of quartz, dolomite, kaolinite and muscovite with less than 1 vol % of Au-bearing pyrite of two grain types: *i)* individual euhedral crystals of variable size (<1 to ~30 µm) likely precipitated by hydrothermal fluids, and *ii)* agglomerates of small crystals (<few microns) of so called 'framboidal pyrite'

[1] EPMA and LA-ICPMS point-by-point analytical data of experimental and natural samples are available as a Microsoft Excel file upon request to the corresponding author.

likely representing biogenic pyrite (Fig. S-2e,f). Euhedral crystals were found to have very fine zones (<few μm thick) with higher As contents. Both EPMA and LA-ICPMS measurements yielded relatively low, though fairly heterogeneous, As contents (from <0.02 to ~0.2 wt. %, with an average close to 0.05 wt. %, Table S-3). Electron probe microanalyses (spot size ~2 μm) showed Au to be below the detection limit (d.l. ~200 ppm). More sensitive (d.l. ~0.1 ppm) but less spatially resolved (spot size ×10 larger) LA-ICPMS analyses yielded ~20 ppm Au on average. No distinction could be made in Au-As patterns between the two types of pyrite, because of the two small grain size, but the two elements on average showed a good positive correlation (R^2 = 0.93). To enable the analysis of this pyrite sample by synchrotron X-ray absorption spectroscopy, pyrite was separated from the carbonate-silicate matrix by repeated extractions with heavy liquids (tetrabromoethane, density 2.97 g/cm^3) of the finely ground whole rock powder, followed by centrifugation, and repeated washing with acetone and final drying. The pyrite material (>90 % purity) was then pressed in a pellet for synchrotron analyses, similar to the other samples.

All natural and experimental arsenian pyrites and arsenopyrites and experimental löllingites of this study showed very good 1:1 negative correlations between As and S tenors among individual datapoints analysed, with a slope close to −1 in at. % units (*e.g.*, Fig. S-3), attesting for the ubiquitous isomorphic As^{-I} to S^{-I} substitution in the mineral structure, as reported previously by most natural and experimental studies (*e.g.*, Cathelineau *et al.*, 1989; Boiron *et al.*, 1989; Fleet and Mumin, 1997; Reich *et al.*, 2005; Filimonova *et al.*, 2020). Invisible gold manifested positive correlations with As in arsenian pyrites (*e.g.*, MCB 7358 sample; Fig. S-3), in agreement with general trends for many natural pyrites (Reich *et al.*, 2005), and negative 1:1 correlations with Fe in Au-rich (up to ~2 at. %) experimental löllingite (*e.g.*, LO2; Fig. S-3), indicating Au-to-Fe substitution. Gold correlations with As, Fe or S tenors in arsenopyrites were poorly expressed, which would be expected considering relatively low Au concentrations (typically <0.3 at. %) compared to the major element contents (>30 ± 0.5 at. %) and their associated analytical uncertainties obscuring eventual correlations (if any).

2. Methods: Analytical, Spectroscopic and Theoretical Methods

2.1. Conventional analyses

All experimentally synthesised and selected natural samples were analysed for phase composition and major and trace element contents by optical microscopy (OM), powder X-ray diffraction (XRD), scanning electron microscopy with energy dispersive spectroscopy (SEM-EDS), transmission electron microscopy (TEM), electron probe micro analyser (EPMA), laser ablation - inductively coupled plasma mass spectrometry (LA-ICPMS), and inductively coupled plasma - atomic emission spectrometry (ICP-AES).

The OM, XRD and SEM analyses show the dominant presence of pyrite, arsenopyrite, or löllingite, respectively, in the corresponding experiments designed to synthetise each of those phases, with very minor (<5 % of total volume) other Au-free phases (As_2O_2, FeS, Au, AsS, NaCl, depending on the initially loaded fluid and solid compositions; Tables S-1, S-2). Natural well-crystallised samples examined in this study show pyrite and arsenopyrite, with minor easily identifiable Au-free silicate, quartz or carbonate impurities in some samples.

A few TEM analyses were performed on Au-bearing arsenopyrite (and arsenian pyrite) of sample MW15 from the Tabakoroni deposit (Table S-3). Images and electron diffraction and energy dispersive X-ray fluorescence spectra were acquired using a MET-JEOL-JEM-2100F electron microscope of the Centre de Micro Caractérisation Raimond Castaing, Toulouse (accelerating voltage 200 kV, spatial resolution ~3

Å) on micron-thick samples prepared using a precision ion polishing system (PIPS). No metallic gold or other Au mineral nanoparticles have been detected in arsenopyrite and pyrite, demonstrating that Au is likely to be in a chemically bound state, which is also in agreement with the <1 Å resolution XAS data of this study.

Major element contents (Fe, S and As in Py, Apy and Lo) have been quantified by EPMA (Cameca SXFive, electron beam spot ~3 µm, accelerating voltage 15 kV, current 20 nA, counting time 60 s) according to adopted procedures (Velásquez *et al*., 2014). Experimentally synthetised arsenopyrites were found to be slightly enriched in As compared to S (by ~1–2 at. %), whereas natural arsenopyrites investigated here were slightly As-depleted (~3 at. %). Experimental pyrites from CE (hydrothermal) and SF (dry) series (Tables S-1, S-2) were all As-poor (<0.1 wt. %), with CE samples being stoichiometric ($FeS_{2.00}$) and SF samples slightly enriched in S ($Fe_{0.95}S_{2.05}$), whereas the LO series pyrite (LO6) contained up to 1 at. % As. Invisible Au could only be quantified using EPMA in arsenopyrites and löllingites, whereas in pyrites Au was below detection limit (Cameca SXFive FEG microprobe, electron beam spot ~1 µm, accelerating voltage 25 kV, current 100 nA, counting time 240 s, detection limit 200 ppm Au).

Gold (in experimental samples) together with other trace elements (in natural samples) was additionally analysed in large arsenopyrite and pyrite crystals (>10–20 µm) by LA-ICPMS using a Finnigan MAT Element equipped with a femtosecond UV laser (laser spot diameter ~20 µm yielding an ablation crater of 25–30 µm, energy 0.003 mJ, fluency 0.94 J/cm^2, power 12 %, frequency 5 Hz, background time 30 s, ablation time 60 s; Pokrovski *et al*., 2019). Transient ablation signals were converted to concentration using the SILLS software (Guillong *et al*., 2008), and using Au-bearing FeS (LaFlamme Po726 standard reference material, 46 ± 2 ppm Au; Sylvester *et al*., 2005), polymetal sulfide MASS-1 (Wilson *et al*., 2002), natural arsenopyrite (Pokrovski *et al*., 2002a), and silicate glass NIST SRM-610 (Pearce *et al*., 1997) external trace element-bearing standards, and ^{57}Fe in pyrite and ^{57}Fe or ^{75}As in arsenopyrite as an internal standard. Despite the meagre set of such analyses due to small grain size in most experimental samples, they are in good agreement for gold with those obtained by EPMA above and those by X-ray absorption spectroscopy (Tables S-1 to S-3). Invisible gold contents in natural and experimental Apy samples neither correlate with As total contents, nor, more generally, with the degree of As depletion or enrichment in arsenopyrite, in contrast to some previous suggestions based on specific natural samples (*e.g.,* Johan *et al*., 1989).

Bulk Au, Fe, S and As contents were also analysed in the natural arsenopyrite and pyrite MCB7358 samples by ICP-AES after complete digestion of the crystals in aqua regia and following the established protocols (Kokh *et al*., 2016, 2017), in order to calibrate bulk Au standards for direct analyses of the other pyrite and arsenopyrite samples by X-ray absorption spectroscopy. Dissolved Au was also analysed by ICP-AES in solutions recovered in some hydrothermal experiments (CE series) followed by solution evaporation and aqua-regia treatment as described in detail in Kokh *et al*. (2017).

2.2. High-resolution X-ray absorption spectroscopy (HR-XAS)

2.2.1. Spectroscopic setup

High energy resolution fluorescence detection - X-ray absorption spectroscopy (HERFD-XAS, hereafter HR-XAS for simplicity) Au L_3-edge (11.919 keV) analyses of experimental and natural samples were performed at FAME (BM30b) beamline (Proux *et al*., 2005) and, more recently, at FAME-UHD (BM16) beamline (Proux *et al*., 2017) of the European Synchrotron Radiation Facility, Grenoble, France, after its major upgrade in 2019-2020 (Fig. S-4). The measurements used a recently developed crystal analyser spectrometer operating in HERFD mode (Llorens *et al*., 2012) and followed a similar protocol as in Pokrovski *et al.* (2019). Compared to conventional XAS spectroscopy, HR-XAS has two major advantages indispensable for studies of gold and similar metals in sulfarsenides: *i)* a significant gain in

spectral resolution compared to nominal resolution defined by the core hole width of the absorption edge; this gain allows accurate detection of different features in X-ray absorption near-edge structure (XANES) spectral region, which are indicative of Au redox state and coordination geometry, but are generally poorly expressed in nominal-resolution spectra (*e.g.,* Pokrovski *et al*., 2009a, 2019), and *ii)* the ability to efficiently filter off all unwanted contributions from elastic scattering and fluorescence from other elements in the sample (and, in particular, from arsenic whose intense Kα fluorescence line, ~10.5 keV, is close to the probed Au Lα fluorescence line, ~9.7 keV), and thus significantly improve both the limit of detection for Au and signal-to-noise spectral ratio.

The X-ray optics on both beamlines incorporated a Si(220) double crystal monochromator with sagittal focusing (beam spot full width at half maximum, FWHM, at the sample ~200 × 300 μm^2 at FAME and ~200 × 200 μm^2 at FAME-UHD), Rh-coated mirrors for harmonic rejection, and a crystal analyser spectrometer with 5 Si(660) crystals (FAME) and 12 Si(660) crystals (FAME-UHD) placed in a Rowland circle geometry (Fig. S-4c, Bragg angle = 85.71°), enabling a spectral resolution of 1.3 ± 0.1 eV at the $L\alpha_1$ Au fluorescence line, which corresponds to a significant gain in resolution compared to classical mode (core-hole lifetime broadening is 5.54 eV at Au L_3-edge; Campbell and Papp, 2001). High-resolution fluorescence XANES together with EXAFS spectra were recorded using a Vortex EX-90 mono-element detector (Fig. S-4a,b). The use of such an energy-resolved detector (bandwidth around 200 eV) allowed collection of the photons diffracted by the spectrometer crystals in Bragg conditions for Au $L\alpha_1$ and removal of all other contributions (mainly the As $K\alpha_{1,2}$ contribution), thereby greatly improving the signal-to-noise ratio. Grains of natural pyrite and arsenopyrite were carefully selected under binocular microscope. Experimental Py, Apy and Lo fine-grained samples were also cleaned up under microscope by manually removing large visible impurities and gold particles. All samples were then homogenised by mild grinding (to ~10 μm size), which is necessary for obtaining HR-XAS signals devoid of harmonics, diffraction peaks, spectral distortions, and self-absorption artifacts which are common for inhomogeneous samples (*e.g.,* Curis *et al.,* 2005, and references therein). The powders were pressed into 5-mm diameter pellets, affixed with silicon grease to a copper-metal holder (for better heat transmission) and placed in a liquid He cryostat (~10–15 K) to reduce X-ray beam-induced damage common for redox-sensitive elements like Au (*e.g*., Pokrovski *et al.,* 2009b). The crystal analysers are placed in a sealed Plexiglas box, filled with He to reduce the absorption of the Au fluorescence signal by air, and equipped with a large Kapton-film window (thickness ~50 μm) to efficiently collect the photons, which leaves only a very short path (a few cm) between the cryostat or detector and the window (Fig. S-4a).

2.2.2. Structural references and energy calibration

A large range of reference Au-bearing compounds with known crystal structures in which Au is in 0, I, II or III formal oxidation state and has a nearest coordination geometry spanning from the most common linear (2) to dodecagon (12), such as: Au (Suh *et al*., 1988), $Na_3Au(S_2O_3)\times 2H_2O$ (Ruben *et al*., 1974), Au-thiomalate (Bau, 1988), $KAuCl_4\times H_2O$ (Berrodier *et al*., 2004), Au_2S (Ishikawa *et al*., 1995), AuAgS (Seryotkin *et al*., 2014), $AuSb_2$ (Furuseth *et al*., 1965), $AuTe_2$ (Schutte and De Boer, 1988) Au-doped CuS (Tagirov *et al*., 2016), $LaAuAs_2$ (Rutzinger *et al*., 2010), $Nd_{10}Au_3As_8O_{10}$ and $Sm_{10}Au_3As_8O_{10}$, (Bartsch *et al*., 2015), and $AuCl(PO_3)(CH_3)_3$, $AuAuClP(Phen)_3$ and $AuCl(P(Phen)_3)_2$ (where Phen is the phenol cycle C_6H_5OH; Benfield *et al*., 1994), were ground and diluted by mixing with boron nitride powder to obtain an Au concentration of 1–2 wt. %, comfortable for fluorescence measurements but low enough to avoid self-absorption effects that may lead to damping of XANES amplitudes. The prepared mixtures were pressed in pellets, placed in the cryostat at temperatures of 10 to 15 K, and recorded both in transmission (nominal resolution) and fluorescence (high resolution) modes, similar to the sulfide and sulfarsenide samples. Energy calibration of the beamline was performed using a 5-μm gold metal foil placed behind the sample, and its spectrum was periodically monitored to correct for eventual energy drift; as a result,

maximum absolute uncertainty in the energy position among the spectra of different samples recorded in 4 different beam-time sessions at the two beam lines is ±0.5 eV.

2.2.3. Determination of chemically bound and metallic gold

Because some of our natural and experimental samples contain both visible (> ~1 μm) and invisible (nano-particulate and/or structure-bound) gold, care was taken to avoid gold particles larger than ~1 μm and to ensure relative homogeneity of the invisible Au concentration across the whole beam spot size, which is essential for obtaining accurate and reproducible XAS spectra. The beam spots for spectra acquisition were thus carefully chosen by scanning each pellet in the vertical direction (*e.g.*, Fig. S-5), which is the most sensitive to the beam spot position in the present setup (see Fig. S-4). The X-ray beam was positioned sufficiently far from intense fluorescence peaks arising from large gold particles to allow us to probe essentially invisible and relatively homogeneously distributed gold in the sample. Multiple HR-XAS scans (2 to 30, ~35 min per scan) were recorded and, after careful examination and eventual correction for energy drift, were merged to increase the signal-to-noise ratio. The concentration of invisible gold in Py and Apy samples was directly determined from the absorption edge height of the fluorescence spectrum using, respectively, natural Au-bearing pyrite and arsenopyrite standards from the Villeranges deposit, France (samples MCB7358-Py with 61 ± 15 ppm Au, and MCB7358-Apy with 1300 ± 200 ppm Au on average; Table S-3) in which gold is present dominantly (at least >95 %) in a non-metallic chemically bound state as demonstrated by Mössbauer spectroscopy (Boiron *et al.*, 1989). Total concentrations of Fe, S, As and Au in those samples were determined by ICP-AES after complete acid digestion. For löllingite, sample LO3 extensively analysed by EPMA (1500 ± 500 ppm Au) was adopted as a standard for the other $FeAs_2$-dominated samples. Because the incoming beam and the outgoing fluorescence signal are absorbed by the sample as a function of the dominant atomic number, our procedure ensures that the standards have the same atomic number matrix as each corresponding type of sample (FeS_2, FeAsS and $FeAs_2$). The sample Au concentration may thus be directly estimated using proportionality between absorption edge height in fluorescence mode ($\Delta\mu_{fl}$) and Au concentrations of sample (i) (where i = Py or Apy or Lo) and the standard (st) of a similar matrix:

$$C_{Au}(i) = \Delta\mu_{fl}(i) \times C_{Au}(st)/\Delta\mu_{fl}(st) \qquad \text{(Eq. S-9)}$$

The acquired HR-XAS spectra were normalised to the absorption edge height with the Athena software (Ravel and Newville, 2005) to compare with spectra of reference compounds (*e.g.*, Fig. 1, S-6) and perform linear combination fits (LCF) to directly quantify the contributions from native nano-particulate gold Au^0 and chemically bound gold (*e.g.*, Fig. S-7). This analysis is greatly facilitated by the contrasting features in the spectra of metallic and chemically bound Au. For example, the presence of the very intense characteristic Au^0 feature at 11945 eV, combined with the Au^0 low-intensity double-resonance white line that strongly contrasts with those of other Au chemical compounds (Fig. 1, S-6), enables Au^0 to be detected in experimental and natural sulfarsenide samples at atomic fractions as low as 3–5 % (Tables S-1 to S-3). The resulting concentration of chemically bound Au in sample (i) is thus calculated as the product of the [100 − Au^0] fraction (%) and the total $C_{Au}(i)$ concentration derived from Eq. S-9 above. Furthermore, the spectral contrast enhanced by high-resolution mode between Au^0 and chemically bound Au allows the LCF determined contribution of Au^0 to be accurately subtracted from the sulfarsenide spectra, thus greatly facilitating their cross-comparisons and further XANES and EXAFS analysis described in the following section.

2.2.4. XANES and EXAFS spectra analyses

To enable interpretation of measured Fe sulfide and sulfarsenide spectra in terms of Au atomic environment, in the absence of matching reference compounds, the XANES spectra were compared with quantum-chemistry simulated ones for different Au cluster geometries and substitution models in pyrite,

arsenopyrite and löllingite (Fig. 2, S-8). The XANES part of the spectrum is particularly sensitive to Au redox state and structural site geometry and adjacent sites arrangement, but is less sensitive to the exact identity of the Au coordinating atoms (As vs S) and their interatomic distances within a similar coordination geometry (*e.g.*, octahedron). In contrast, the EXAFS part of the spectrum does not require calibration by reference compounds, and being almost insensitive to the exact site geometry, allows accurate distinguishing between lighter (S) and heavier (As) atoms, enabling the number and distances of individual neighbors to be better constrained, provided sufficient signal-to-noise spectral statistics. The latter aspect is far more critical for EXAFS than for XANES and thus requires much longer counting times and multiple scans, posing challenges for the long-term beam line stability (10s hours).

Very good-quality EXAFS spectra (exploitable to ~13 $Å^{-1}$) have been obtained on six experimental arsenopyrite and löllingite (MA1-MA4, LO2 and LO4) and one natural arsenopyrite and one arsenian pyrite (MCB7358) (Fig. S-9). They were analysed with the Demeter program (Ravel and Newville, 2005) according to recommended protocols and taking account of spectral statistics (Kelly *et al.*, 2008), to obtain the Au-neighbor identity (*i.e.* Au, S, Au, Fe) and number of atoms and interatomic distances for the nearest and more distant shells (where possible; Table S-4). The uncertainties on the obtained parameters have been carefully evaluated by comparing different fit models and using statistical criteria (*e.g.*, Kelly *et al.*, 2008; Tella and Pokrovski, 2009; Bazarkina *et al.*, 2010). Typical EXAFS detection limits for As in an S-dominated Au nearest shell (*e.g.*, in pyrite) and for S in an As-dominated shell (in arsenopyrite and löllingite) of 6-fold coordination are typically 0.5 and 1 atom, respectively, which is inherent to the intrinsic uncertainties of EXAFS in quantifying exact coordination numbers. Note that with poorer spectral statistics and shorter exploitable EXAFS spectral range (typically to 10–11 $Å^{-1}$ in previous studies of pyrite samples, *e.g.*, Filimonova *et al.*, 2020), the statistically detectable limit for As in an $Au(As,S)_6$ shell in pyrite increases to >1 As atom. These uncertainties further increase for outer Au atomic shells due to increasing disorder (*e.g.*, Teo, 1986). Therefore, to allow for more robust fits, some first-shell and outer-shell total coordination numbers were constrained to their crystallographic values as imposed by the mineral structure, and alternative Au second-shell neighbors (Fe, Au, As) were also considered (Table S-4).

For other, less Au-concentrated samples or those dominated by metallic gold, the insufficient signal-to-noise ratio did not allow acquisition of accurate EXAFS spectra; consequently, the interpretation of those samples is based on their XANES spectra only, by comparing them with theoretical models described in the following section.

2.3. Quantum-chemistry ab-initio modeling of XANES spectra using FDMNES

Ideally, direct and unambiguous interpretation of XANES spectra, particularly in high-resolution mode, would require reference compounds with Au redox and structural environments being as close as possible to those of the samples. Because of the lack of such reference compounds in the Au-Fe-S-As system, a theoretical simulation of XANES spectra is the method of choice. The increasingly growing application of this method to synthetic and natural materials has been boosted owing to recent progress in quantum-chemical modelling of full electron potential in the near-edge absorption region, coupled with increasing computer power enabling the use of Fine Difference Methods (FDM) for solving the Schrödinger equation on the node points of a three-dimensional grid (Amestoy *et al.*, 2006; Guda *et al.*, 2015) as implemented in the FDMNES code (Joly, 2001; Bunau and Joly, 2009). Using this code, we simulated Au L_3-edge HR-XANES spectra of different possible Au local structures in pyrite, arsenopyrite and löllingite, by considering Au substitution in the Fe, As or S crystallographic sites and with different numbers of As and S neighbors around Au, to compare them with the experimental spectra. Details of the method are given elsewhere (Pokrovski *et al.*, 2019).

Briefly, calculations were performed in FDM mode and accounting for relativistic effects and spin-orbit interactions intrinsic to heavy atoms such as gold and using self-consistent potentials allowing accurate determination of the Fermi energy level (code keywords *SCF, Relativism, Spinorbit*; Joly, 2020). The obtained raw calculations are further convoluted with a Lorentzian function (keyword *Arc*) with a width of 1.3 eV (keyword *Gamma_hole*), which corresponds to the energy resolution of our HERFD setup. To allow robust comparisons in energy position between theoretical and experimental spectra, the simulated convoluted spectra were shifted according to differences in their calculated initial orbital energy (*Epsii*; Joly, 2020). This correction was found to be mineral (atomic matrix) dependent and to have a typical uncertainty of ±0.5 eV, which is comparable with that of the experimental energy calibration. The FDMNES simulations explored a large choice of different structural models of Au in the three minerals generated by DFT calculations of structure relaxation as described below.

2.4. DFT calculations of Au in the sulfide and sulfarsenide structures

Density Functional Theory (DFT) calculations were performed using the PWscf code of the Quantum ESPRESSO package (Giannozzi *et al*., 2009; http://www.quantum-espresso.org). The ionic cores of iron, sulfur, arsenic, and gold were described by ultra-soft pseudopotentials from the Garrity-Bennett-Rabe-Vanderbilt (GBRV) library (Garrity *et al*., 2014). We used the generalised gradient approximation (GGA) to the exchange-correlation functional with the Perdew-Burke-Ernzerhof (PBE) parametrization (Perdew *et al*., 1996). Using 40 and 480 Ry cutoffs for the expansion in plane waves of the electronic wave functions and charge density leads to a convergence of the total energy to better than 0.5 mRy/atom. The first Brillouin zone of pyrite and arsenopyrite was sampled according to the Monkhorst-Pack scheme (Monkhorst and Pack, 1976), using a shifted 4×4×4 *k*-point grid, whereas a shifted 4×4×8 *k*-point grid was used for löllingite. Cell parameters and atomic positions were optimised leading to equilibrium structures in good agreement with the experimental ones (Table S-5, Fig. S-10). The DFT unit-cell volumes are only 0.8 % smaller than the experimental volumes for both pyrite and arsenopyrite, and 1.2 % larger for löllingite. Regarding bond distances, DFT slightly underestimates Fe-S bonds and overestimates the other bonds (Fe-As, S-S and As-S), but theoretical bond lengths are still within 1.7 % of the crystallographic XRD values.

Various models of gold-bearing sulfarsenide minerals were built by putting 1 or 2 Au atom(s) in Fe, As or S site of neutral supercells, all containing 96 atoms in total (2×2×2 supercells were used for pyrite and arsenopyrite, and a 2×2×4 supercell for löllingite). Only the centre of the Brillouin zone is sampled (so called Γ-point) and the structure is fully relaxed (*i.e.* cell volume and atomic positions are optimised). Table S-6 compiles the optimised structural parameters of the models considered here for pyrite (Py), arsenopyrite (Apy) and löllingite (Lo), and named according to the atomic site hosting Au atom in a given coordination. These Au local atomic structures were then used to calculate theoretical XANES spectra using the FDMNES code (Fig. 2, S-8).

The three models simulating a classical Au substitution in the Fe site of pyrite, arsenopyrite and löllingite, keeping the original coordination (*i.e.* Fe-site [AuS_6] in Py, Fe-site [$AuAs_3S_3$] in Apy, and Fe-site [$AuAs_6$] in Lo) were already considered in Trigub *et al*. (2017). Our results are fully consistent with theirs, obtained from the same code and same functional but different pseudopotentials. In both studies, bond lengths involving the Au atom are the same within ±0.01 Å. In the three minerals, Fe is in octahedral site. Substituting an Au atom for an Fe atom expands the size of the octahedron. On average, the Au-S and Au-As bonds are 0.2 Å and 0.1 Å longer than the Fe-S and Fe-As bonds, which is consistent with the larger covalent radius of Au compared to low-spin Fe^{II} (~1.4 Å *vs* ~1.3 Å). Substituting an Au atom for a S or As atom in arsenopyrite leads to similar expansion of the bonds formed between Au and the nearest Fe neighbours but the S-As dimer (becoming Au-As or S-Au after substitution) is almost unaffected (Table S-6). More elaborated models of Au in the Fe site of pyrite and arsenopyrite of variable As/S stoichiometry,

$Au(As_nS_{6-n})$, matching the EXAFS-derived As and S coordination numbers (Table S-4), were also considered to account for significant deviations of the calculated XANES spectra for Au in a regular Fe site from the measured ones (Figs. 2, S-8). These models produced very similar average Au-S and Au-As nearest-shell distances as the regular models (*i.e.* indistinguishable by EXAFS fits), but did allow much better constraints on the post-edge XANES resonances, which are sensitive to the exact arrangement and atomic composition of neighbouring octahedra. Furthermore, coupled substitution models such as Au^I + As^{III} to $2Fe^{II}$ in adjacent octahedral sites in Apy were also considered. They produced DFT-calculated XANES spectra (not shown) very similar to those of the regular Au-to-Fe substitution, but average calculated Au-S distances (2.50 Å) significantly longer than the EXAFS-derived distances for Apy samples (2.42 ± 0.03 Å; Table S-4). In addition, inclusion of As in the second Au shell in the EXAFS fits of Py or Apy spectra did not improve the fitting, being indistinguishable from fits with 2nd shell Fe, or yielding too small or negative mean square relative displacement factors (MSRD, $\sigma^2 < 0.001$ Å^2) for the Au-As2 shell. Similarly, unambiguous detection of Au-(As/S)-Au pairs in Apy EXAFS spectra was not possible owing to intrinsically large uncertainties of the method for distant shells and the presence of multiple overlapping Fe/S/As contributions (*e.g.*, Fig. S-9, Table S-4).

Finally, two fictitious Au end-members of arsenide compounds (*i.e.* AuAsS and $AuAs_2$) were tentatively modeled in order to explore the evolution of Au local atomic structure and its potential stability in a complete solid solution. Starting configurations correspond to the substitution of all Fe atoms for Au atoms in arsenopyrite and löllingite structures. We also considered the pyrite structure of $AuAs_2$ stoichiometry. DFT-optimised structures are shown in Figure S-11 and Table S-7. The $AuAs_2$ solid stays in the starting structure despite the full structural relaxation without imposing any symmetry. However, the cubic pyrite structure is found to be 2.2 kJ/mol more stable than the löllingite structure (*i.e.* difference of internal energies computed at 0 K). As expected, Au-As bond length increases here compared to the 'dilute' cases of Au-bearing pyrite and löllingite (Au-As distances are ~6 % and 7 % longer, respectively), and the cell parameters also expand accordingly. It is interesting to note that in the case of AuAsS, the structural relaxation leads to a strong elongation in the *b* direction making the structure layered, and Au coordination adopts a distorted square geometry instead of an octahedron. Within layers, Au-As bonds display the same length as in the Au-bearing arsenopyrite whereas Au-S bonds show only a slight elongation (by 1.4 %). This significant change of Au coordination number from 6 to 4, with the arsenopyrite As/S stoichiometry, might provide a support for the spectroscopic and thermodynamic data that suggest a more As-rich Au coordination (this study; Merkulova *et al.*, 2019) than the simple stoichiometric (Au,Fe)AsS substitution postulated earlier (Trigub *et al.*, 2017). Therefore, additional As atoms in the local atomic environment of gold may help stabilizing Au incorporation like in the suggested model 'Fe-site [$AuAs_3S_3$ + $AuAs_6$] Apy' (Table S-6), which is in agreement with both XANES and EXAFS data obtained in this study and with independent thermodynamic considerations (section 3).

2.5. XANES and EXAFS method comparison with available studies

The obtained XAS structural parameters for our hydrothermally synthetised löllingite samples (Fig. 2, Table S-4) are in excellent agreement with those recently reported for samples prepared using conventional dry solid-state synthesis (Trigub *et al.*, 2017). This agreement attests for the universality of Au incorporation in the mineral at atomic level, by substitution for Fe in the octahedral site across a wide range conditions, both water-free and hydrothermal.

The agreement between our and the few available data for arsenopyrite is less straightforward. All our natural and experimental samples obtained in a wide range of hydrothermal solution compositions and from various geological contents show a very similar Au bonding environment, corresponding on to As-enriched combined Apy-Lo Fe crystallographic sites, with an average Au first-shell atomic environment of

[$Au(As_{4.5 \pm 0.5}S_{1.5 \pm 0.5})$] as attested by both XANES and EXAFS modeling and the Au fluid-mineral partitioning trends (section 3). In contrast, rare published HR-XAS data suggest a more variable Au environment, ranging from stoichiometric Au-to-Fe substitution, [$AuAs_3S_3$], postulated based on spectra of bulk samples synthesised under water-free conditions (Trigub *et al*., 2017), to 'purely As' environment for Au in [$AuAs_6$] sites, as inferred from a single micro-XAS measurement of an arsenopyrite sample from the Villeranges deposit (Merkulova *et al*., 2019), which likely was similar to our MCB7358-Apy sample. However, this apparent discrepancy on the number of As neighbors around Au may easily be reconciled by taking into account a detection limit of 1 S atom in the As-dominated Au first shell of Apy, as evaluated in this study. Furthermore, the exceptionally good signal-to-noise ratio for XAS spectra obtained in our study (Fig. S-8, S-9) allowed us to accurately analyse the post-edge XANES features, more sensitive to the Au octahedra arrangement and number of As/S neighbors, which was not possible in those previous studies given the less favourable spectral statistics. Finally, an independent discrimination among the possible structural models for Au in Apy is provided by the thermodynamic analysis of this study (section 3).

The existing interpretations of the state of chemically bound Au in pyrite based on XAS data from available studies exhibit the largest apparent discrepancy compared to the sulfarsenides. Our recent HR-XAS study of hydrothermally synthetised As-free pyrites (Pokrovski *et al*., 2019) unambiguously demonstrated, based on XANES spectra coupled with DFT and FDMNES simulations and direct Au fluid-pyrite partition coefficient measurements, that Au^I is dominantly chemisorbed on pyrite surfaces as Au^I(poly)sulfide species typical to those well-documented in hydrothermal fluid (Pokrovski *et al*., 2009a, 2015). For arsenian pyrites, both synthetic and natural, examined in the present study, Au bound state is distinctly different as attested by both HR-XANES and EXAFS spectra analyses, demonstrating that Au enters an As-enriched Fe site $AuAs_nS_{6-n}$, with n of up to 3 (Figs 1, 2, Table S-4). These findings are in excellent agreement with some of the available synthetic As-pyrite samples with negligible fractions of arsenopyrite (<5 %) from Filimonova *et al*.'s (2020) study, but differ from other similar samples from their study that were rather interpreted by a mixture of spectral contributions from Au in the FeS_6 structural site and an Au sulfide solid, Au_2S(s). We note, however, that the structure of Au_2S(s), with 2 S atoms around Au at 2.17 Å in the first shell, and 12 Au atoms at 3.55 Å in the next-nearest shell (Ishikawa *et al*., 1995), is inconsistent with the reported Au-S distances of >2.30 Å, nor with the number of S and Au neighbors in most samples as reported in Filimonova *et al*.'s (2020) study based on least-square fits of EXAFS spectra. Furthermore, the formation of Au_2S(s), which is a thermodynamically unstable Au compound in hydrothermal experiments saturated with respect to Au metal, points to some extreme disequilibrium phenomena, which would be difficult to conceive. Therefore, in the absence of more direct evidence, such as linear combination fits of XANES spectra or powder X-ray diffraction and/or transmission electron microscopy, Au state in pyrite from Filimonova *et al*.'s (2020) study would be more consistent with a mixture of contributions arising chemisorbed Au-polysulfide species and Au partly incorporated in the Fe crystallographic site variably enriched in As ($1 < n < 3$), in line with our own findings. Finally, another recent HR-XAS study of an arsenian pyrite sample (~2 at. % As), taken from a mine tailing in Columbia (Merkulova *et al*., 2019), reported Au to be in a regular Fe crystallographic site AuS_6, based on EXAFS fits and XANES-FDMNES comparisons of spectra acquired from a single beam spot position (4 × 4 μm) by micro-XAS. We emphasise, however, that the presence of As at $n < 1$ in such an S-dominated site would be hardly detectable within the spectral resolution. Moreover, the studied sample contained anomalously high invisible Au concentrations (0.48 wt. % Au), which is a factor of 10 above the solubility limit of Au in arsenian pyrite established on the basis of a large set of data from different gold deposit types (Reich *et al*., 2005; Deditius *et al*., 2014). Such anomalous Au concentrations might be related to cyanide treatment of original pyritic ore before its storage in tailings from which the studied sample originated.

2.6. Thermodynamic calculations in experimental fluid-mineral systems

Gold speciation and solubility in the fluid phase and mineral phases formed at equilibrium in the hydrothermal experiments (Table S-1) were modelled using available thermodynamic data to derive Au fluid-mineral (Py, Apy and Lo) partition coefficients and establish a model of Au solubility in the mineral. Calculations were performed using the HCh software package and associated Unitherm database, allowing chemical equilibrium simulations in multicomponent fluid-mineral systems based on the minimization of the system Gibbs energy (Shvarov, 2008, 2015), and accounting for non-ideality of the fluid using the extended Debye-Hückel equation (Helgeson *et al*., 1981). The selection of thermodynamic data sources for Au, S, As and Fe is briefly summarised here and was discussed in more detail elsewhere for each corresponding element (see Perfetti *et al*., 2008; Pokrovski and Dubessy, 2015; Pokrovski *et al*., 2015, 2019; Kokh *et al*., 2017, 2020).

The thermodynamic properties of pure minerals (*e.g*., solid and liquid sulfur, pyrite, pyrrhotite), major fluid components (salts), and some common ionic sulfur aqueous species (*e.g*., sulfate, sulfide) were taken from the updated SUPCRT (Johnson *et al*., 1992), JANAF (Chase, 1998), and Robie and Hemingway (1995) databases, complemented by recent data for ionic sulfur forms including $S_3^{\bullet-}$ (Pokrovski and Dubessy, 2015) obtained within the revised and extended HKF (Helgeson-Kirkham-Flowers) equation of state (Oelkers *et al*., 2009; Sverjensky *et al*., 2014; and references therein) to 500 °C and 30 kbar, and $S_2^{\bullet-}$ in a more limited *T-P* range (450 °C, 500–1500 bar; Pokrovski *et al*., 2019). The data for ferrous iron Fe^{II} species, Fe^{2+}, $FeCl^+$, $FeCl_2$ were taken from Sverjensky *et al*. (1997) and those of $FeCl_4^{2-}$ from Testemale *et al.* (2009) which is complementary to the existing dataset. Ferric iron Fe^{III} chloride species reported in the literature in oxidised (*i.e.* hematite-dominated) saline fluids at $T > 300$ °C (Saunier *et al*., 2011) were found to be negligible at the redox conditions of the present study (NNO ± 3). The properties of the dominant aqueous As^{III} hydroxide complexes and pure iron sulfarsenide minerals (FeAsS, $FeAs_2$, and FeAs) were adopted from Perfetti *et al*. (2008). The thermodynamic properties of the molecular sulfur aqueous forms, H_2S, SO_2, and dissolved H_2 and O_2 were used according to the Akinfiev and Diamond (2003) model for aqueous non-electrolytes, which allows a more accurate description over the *P-T* range relevant to our study (450 °C; <1 kbar) than the HKF model. Noteworthy, the thermodynamic data from Akinfiev and Diamond (2003) were also used in derivation of the thermodynamic properties of the Au species (see below) and thus were chosen here to maintain thermodynamic consistency.

The major As aqueous species over the entire range of our conditions is $As^{III}(OH)_3$. We also included and examined a recent model of As solid solutions in marcasite and arsenopyrite proposed by Xing *et al*. (2019) based on the published thermodynamic properties for the pure phases from Perfetti *et al*. (2008) and on Density Functional Theory and Monte Carlo theoretical calculations of As substitution for S in the FeS_2 and FeAsS structures (Reich and Becker, 2006). This model yielded equilibrium As tenors in pyrite and arsenopyrite from our hydrothermal syntheses being similar within errors to the analytically determined values (samples of MA and CE series, Table S-1). The model, however, had a negligible impact on the calculated Au solubility and oxygen and sulfur fugacity compared to calculations using pure pyrite and arsenopyrite end-members. For experiments of löllingite synthesis (LO series), the model predicted almost S-free ($X_S < 10^{-6}$) and insufficiently abundant (less than 50 % of total sulfarsenide amount along with FeS) löllingite compared to the experiments in which löllingite was the largely dominant phase (>95 %). These model predictions thus contrast with the large abundance of löllingite and significant S fractions found in the experimental Lo samples (X_S ~0.1–0.2; Table S-1). Such discrepancies are likely due to the intrinsic limitations of Xing *et al.*'s (2019) model for the $FeAs_2$-rich solid solution region, for which the model was not calibrated and thus should be regarded with caution. Therefore, we have not considered the Xing *et al.*'s (2019) model for the Lo-rich compositions of our study.

The thermodynamic properties of 'traditional' hydrogensulfide (AuHS, $Au(HS)_2^-$) and hydroxide (AuOH) species were taken from the compilation of Pokrovski *et al*. (2014), consistent with most experimental data, whereas those for the di-chloride species ($AuCl_2^-$) from Zotov *et al.* (2018), and those for the recently discovered gold complex with the trisulfur ion, $Au(HS)S_3^-$ from Pokrovski *et al*. (2015). Species such as AuCl, $AuCl_3^{2-}$, and $Au(OH)_2^-$, tentatively suggested in some previous compilations, were ignored in the present modeling owing to the large uncertainties associated with their stability constants at elevated temperatures. Among the chosen species, $Au(HS)_2^-$ was the dominant complex in the experiments considered in thermodynamic modeling of Au fluid-mineral partitioning. In addition, AuHS and $Au(HS)S_3^-$ also contributed to gold solubility at acidic pH (<5) in S-poor and S-rich solutions, respectively. The precision of our predictions of equilibrium Au concentrations at a given experimental fluid composition is typically better than 50 % of the value, as conditioned by intrinsic uncertainties of the thermodynamic data and activity coefficient models chosen here. The calculated Au solubility in the CE series of samples are comparable, within similar uncertainties, to those directly analysed in quenched fluids (Table S-8), supporting the validity of our predictions and demonstrating the attainment of fluid-mineral equilibrium in the experiments. In the following thermodynamic analysis of Au mineral/fluid partitioning, we therefore adopted, for the sake of consistency, the calculated Au solubility and $Au(HS)_2^-$ activity for the whole set of hydrothermal experiments considered in this study.

3. Supplementary Text: Additional Notes on Thermodynamic Approaches

The new structural model of chemically bound Au in arsenopyrite and löllingite established in this study (Figs. 3, S-8), coupled with the robust physical-chemical constraints on the experimental systems (section 2.6) and the Au fluid-mineral distribution coefficients (Table S-8), enables, for the first time, to test a quantitative thermodynamic model of Au partitioning and solubility in iron sulfarsenides.

3.1. Equilibrium between invisible gold, hydrothermal fluid and minerals

Metallic gold detected in some of the experimental samples studies here, both visible and submicronic, is likely to originate from direct precipitation from the fluid upon quench and/or during the run due to minor temperature gradients that might favour gold redistribution within the experimental container. Additionally, eventual partial transformation of the chemically bound gold formed at high temperature to Au^0, in response to changes in the fluid parameters and composition on cooling, should be considered. Indeed, this phenomenon is likely to be responsible for the origin of Au^0 detected in some of the natural samples investigated here that have undergone a complex history of fluid-mineral re-equilibration and crystal growth at geological time scales (Table S-3). It is, however, unlikely to be significant for the experimental samples due to incomparably faster cooling rates (minutes) compared to natural systems. Therefore, it can be assumed that the concentration of chemically bound gold, determined in experimental solids as described above (Eq. S-9), represents the 'true' dissolved Au concentration in the mineral in equilibrium with both the fluid and metallic gold at the experimental *T-P* conditions.

The arsenopyrite and löllingite samples from hydrothermal experiments of this study were found to be relatively homogeneous for major elements (Fe, S and As) and Au distribution, compared to natural ones, which points to close-to-equilibrium conditions, even though some local minor heterogeneity is observed at the micron scale (*e.g.*, Fig. S-3). Close-to-equilibrium conditions are further confirmed by thermodynamic equilibrium calculations that predicted largely dominant Py, Apy and Lo phases, in full agreement with observations of the experimental products (Fig. S-1). Finally, measured Au concentrations

in the fluid after runs of CE series agree well with the predicted Au aqueous contents in equilibrium with metallic gold (Table S-8). Therefore, the chemically bound Au concentrations in those samples and measured mineral-fluid partition coefficients may be interpreted in terms of equilibrium thermodynamics.

3.2. Thermodynamic state of gold and arsenic

All experimental and natural arsenopyrite samples in a wide range of *T-P*, redox and natural contexts examined in this work yield a virtually identical bound gold environment, which may be described as a combination of Au substituted for Fe in arsenopyrite-type, $(Au,Fe)As_3S_3$, and löllingite-type, $(Au,Fe)As_6$, crystallographic sites. These two sites are likely to be mutually stabilised in the arsenopyrite structure (section 2.4), and are not independently distributed in variable proportions given the identical Au XAS spectral signature in all Apy samples investigated here. From a thermodynamic point of view, such bound Au may be regarded as a solid solution between arsenopyrite, FeAsS, and a hypothetical Au-bearing sulfarsenide, $AuAsS$-$AuAs_2$ (or $AuAs_{1.5}S_{0.5}$), as the end-members. In the case of löllingite, in which Au substitutes for Fe in the crystallographic site forming $AuAs_6$ atomic geometries, as demonstrated in this study (Fig. 2), this substitution may be thermodynamically regarded as a solid solution between the $FeAs_2$ and $AuAs_2$ end-members. Note that in those compounds, gold is formally in an oxidation state of Au^{II}, similar to Fe^{II}, which would allow a regular solid solution without the necessity for additional cations, anions or vacancies to compensate for the apparent charge imbalance that would be required if Au^{I} were assumed as the formal redox state in arsenopyrite or löllingite (*e.g.*, Trigub *et al.*, 2017; Merkulova *et al.*, 2019). It should be emphasised, however, that such imbalance would have been only apparent. This is because the notion of oxidation state for Au, the softest metal of the Periodic Table in strongly covalent chemical bonds with As and S, would have little physical sense (*e.g.*, Cabri *et al.*, 2000; Vaughan and Rosso, 2006). Due to the strong electronic orbital overlap, the partial electrical charge of the Au atom in such compounds is far less than the formal charge of +2 as would have been in an ideal purely ionic compound. The much smaller Au partial charge in sulfarsenides is also confirmed in this study by DFT calculations of Bader's charges, yielding values from −0.5 to +0.5 for Au in the three minerals. In contrast, gold in sulfidic aqueous solution, both in our experiments and natural hydrothermal fluids, is largely dominated by the aurous (Au^{I}) bis-hydrogensulfide complex, $Au(HS)_2^-$, with some moderate contributions of mono-hydrogensulfide, AuHS, and poly(sulfide) complexes such as $Au(HS)S_3^-$, depending of the *T-P*, pH, redox, and S total content, as shown by the great majority of available solubility and spectroscopic data (*e.g.*, Pokrovski *et al.*, 2009a, 2014, 2015, 2019, and references therein). Therefore, in the following thermodynamic analysis, $Au(HS)_2^-$ was used.

Arsenic in the three minerals is dominantly present in substitution for S, implying a formal redox state of As^{-I}, as shown by a great majority of experimental, analytical, computational, and direct spectroscopic work (*e.g.*, Morimoto and Clark, 1961; Simon *et al.*, 1999; Savage *et al.*, 2000; Reich and Becker, 2006), and also confirmed by EPMA analyses (Fig. S-3) and indirectly by XANES and EXAFS modeling of Au environment (Fig. 2, S-9) in this study. In the recent years, reports of formally As^{II} and/or As^{III} substituting for Fe in the octahedral site of natural and synthetic arsenian pyrite, based on microanalytical (*e.g.,* EPMA, TEM) and spectroscopic methods (XAS, XPS), have also appeared (*e.g.*, Deditius *et al.*, 2008; Qian *et al.*, 2013; Le Pape *et al.*, 2018). However, the environments in which pyrite may incorporate significant fractions of such oxidised arsenic are limited to either particular low-temperature experimental conditions or relatively oxidised natural epithermal settings in which very little Au is usually hosted by pyrite (*e.g.*, Deditius *et al.*, 2014), implying that As^{III} in the mineral is unlikely to be a controlling factor for Au incorporation in pyrite. Furthermore, our own EPMA, XANES and EXAFS data on pyrite and arsenopyrite do not show evidence for As in the Fe site (sections 2.2–2.4). In contrast, As in hydrothermal solution and silicate melts across a wide range of *T-P*-redox conditions exists in a

trivalent state as the hydroxide $As^{III}(OH)_3$ complex (*e.g.*, Pokrovski *et al.*, 2002b; Perfetti *et al.*, 2008; Borisova *et al.*, 2010). Therefore, As^{-I}-S^{-I} solid solution substitution in Apy and Lo and the $As^{III}(OH)_3$ species in aqueous solution were used as the base for the thermodynamic model of gold incorporation in sulfarsenide minerals as discussed below.

3.3. Controlling Au-As coupled redox reactions

Based on the above considerations, the following thermodynamic reactions should control the partitioning of gold between arsenopyrite (or löllingite) and fluid, and the solubility of metallic gold in arsenopyrite (or löllingite):

$Au(HS)_2^- + H^+ + 1.5\ As(OH)_3 = [AuAs_{1.5}S_{0.5}]_{Apy} + 1.125\ O_2 + 1.5\ H_2S + 2.25\ H_2O$ (Eq. S-10a)

$Au(metal) + 1.5\ As(OH)_3 + 0.5\ H_2S = [AuAs_{1.5}S_{0.5}]_{Apy} + 0.875\ O_2 + 2.75\ H_2O$ (Eq. S-10b)

$Au(HS)_2^- + H^+ + 2\ As(OH)_3 = [AuAs_2]_{Lo} + 1.75\ O_2 + 2\ H_2S + 2.5\ H_2O$ (Eq. S-11a)

$Au(metal) + 2\ As(OH)_3 = [AuAs_2]_{Lo} + 1.5\ O_2 + 3\ H_2O$ (Eq. S-11b)

where $[AuAs_{1.5}S_{0.5}]_{Apy}$ and $[AuAs_2]_{Lo}$ represent the mole fractions (X_{Au}) of the end-member Au solids, AuAsS-$AuAs_2$ and $AuAs_2$, respectively, in the arsenopyrite and löllingite ideal solid solution. In the absence of data on the exact activity-concentration relationships for Au-Fe substitution, the present assumption of ideality is a reasonable first-order approximation. It has, however, little impact of the final results, because at such low Au substitution degrees ($X_{Au} < 0.01$; Tables S-9, S-10) the resulting contribution to the excess energy of mixing is of the order of a few J/mol by analogy with known sulfide solid solutions (*e.g.*, Sack and Ebel, 2006). Such a contribution would be negligibly small compared to the energy change induced by the redox reactions (S-10) and (S-11), which are of the order of 100s kJ/mol.

The thermodynamic partition coefficient between fluid and mineral for dissolved gold in the form of the dominant $Au(HS)_2^-$ complex is defined as

$Q_{Apy/Fluid} = X_{Au}$ (in Apy or Lo)/$a_{Au(HS)_2^-}$ (in fluid) (Eq. S-12)

The thermodynamic constants of reactions (10a) and (11a) are therefore written as

$\log K(10a) = \log(Q_{Apy/Fluid}) + 1.125 \log(f_{O_2}) + 1.5 \log(a_{H_2S}) - 1.5 \log(a_{As(OH)_3}) + pH$ (Eq. S-13a)

$\log K(11a) = \log(Q_{Lo/Fluid}) + 1.75 \log(f_{O_2}) + 2 \log(a_{H_2S}) - 2 \log(a_{As(OH)_3}) + pH$ (Eq. S-13b)

where the activities of aqueous components are expressed in molality units (mol/kg H_2O) and the fugacity of gaseous species (O_2) in bar, in accordance with the thermodynamic framework of the databases used, as calculated at equilibrium for each experiment using the thermodynamic properties of the components discussed in section 2.6 (Tables S-9 and S-10).

It can be seen in Tables S-9 and S-10 that despite the fact that the Au partition coefficient values $Q_{Apy/Fluid}$ in the experiments span a 5 order-of-magnitude range, the calculated reaction (S-10a) constant values are almost identical within the corresponding uncertainties yielding an average $\log K(10a)$ value of −18.2 ± 0.3 (±1 s.d.) at 450 °C and 700 bar. A similar constancy is observed among the two Lo experiments covering a 1.5 log unit range in their respective $Q_{Lo/Fluid}$ values, even though our dataset is yet meagre, $\log K(11a) = -34.3 \pm 0.5$ (±1 s.d.). This constancy strongly supports the validity of our thermodynamic model of the equilibrium fluid-mineral partitioning for gold. The analogous calculated gold solubility reaction constants (Eq. S-10b, S-11b, Tables S-9, S-10) also display a consistent and almost constant set of values, but the range of constituting variables (in particular X_{Au}) is rather narrow making these reactions less sensitive to the choice of the exact substitution model.

3.4. Additional tests of the model

To further test the validity of the choice of Au solid solution endmembers, the so called 'stoichiometric slope analysis', similar to that commonly used for deriving the stoichiometry of aqueous species from solubility experiments (*e.g.*, Pokrovski *et al.*, 2015), has also been performed. An example is shown in Figure S-12 for three alternative models of Au substitution in arsenopyrite invoked in the literature: the $AuAs_{1.5}S_{0.5}$ model of this study, a simple AuAsS model of Au substitution in a stoichiometric Fe site in Apy as postulated by Trigub *et al.* (2017), and an $Au^{I}As_2$ model in which Au^{I} is in Fe-site surrounded by 6 As atoms and accompanied by an Fe-site neighboring vacancy to satisfy the formal apparent charge balance, as proposed by Merkulova *et al.* (2019). The Au fluid-mineral partitioning thermodynamic reactions corresponding to the latter two structural models are written as follows, and their respective constants calculated similarly to that of reaction (S-10a):

$$Au(HS)_2^- + H^+ + As(OH)_3 = [AuAsS]_{Apy} + 0.5\ O_2 + H_2S + 2\ H_2O \qquad \text{(Eq. S-14a)}$$

$$Au(HS)_2^- + 2\ As(OH)_3 = [AuAs_2^-]_{Apy} + 2\ O_2 + 2\ H_2S + 2\ H_2O \qquad \text{(Eq. S-14b)}$$

It can be seen in Figure S-12a that a plot of $\log Q_{Apy/Fluid}$ versus ($\log Q_{Apy/Fluid} - \log K$) for reaction (S-10a) proposed in this study displays a consistent linear trend with very small scatter for the experimental data points, and with a very high squared correlation coefficient ($R^2 \sim 0.98$), and a slope (0.97) very close to the theoretical slope of 1 required by such a relationship. Similarly, the plot for löllingite (reaction S-11a, Fig. S-12d) yields a slope (1.06) very close to 1. In contrast, both reactions (S-14a) and (S-14b) for the 5 Apy data points yield a much larger data point scatter and the resulting poorer plot statistics and slopes significantly deviating from one (Fig. S-12b,c), indicating that such models are less appropriate for the available dataset than the one suggested in this study. Furthermore, an additional structural argument against a simple stoichiometric (Au,Fe)AsS substitution in arsenopyrite (as tested in Fig. S-12b) is the results of DFT simulations of this study demonstrating that the pure AuAsS solid as the end-member has a stable structure very different from that of FeAsS itself, with a layered structure and Au being in a distorted square coordination geometry (Fig. S-11), which would be incompatible with the Au octahedral coordination evidenced in our study. Even though we cannot completely exclude, within the actual errors, that alternative Au models might be applicable to some specific Apy samples as those considered in the previous studies or from different geological settings, we note that the XANES and EXAFS data alone reported in the previous studies would equally be compatible, within their signal-to-noise ratio and the resulting fit statistics, with the Apy model proposed here, which is furthermore strongly supported by the independent thermodynamic analysis given above (Fig. S-12).

3.5. Error analysis

The uncertainties on the calculated fluid thermodynamic variables (As, S, and Au aqueous activities, O_2 fugacity, and pH) are reported in Tables S-8 to S-10. Note that they partially cancel in Eq. S-10 and S-11 (*e.g.*, $Au(HS)_2^-$ activity is directly proportional to that of H_2S and O_2), which leads to partial cancellation of the resulting errors on the K(10a,b) and K(11a,b) values. Combined with the uncertainties related to the determination of the gold arsenide end-member stoichiometry, with $[AuAs_{1.5 \pm 0.5}S_{0.5 \pm 0.5}]$ as a pessimistic estimation, the resulting $Q_{Apy/Fluid}$ and $Q_{Lo/Fluid}$ values and Au solubility in Apy and Lo may be predicted with an uncertainty of ±0.5 log units at 450 °C and 700 bar in As-S-O_2 space (Fig. 4 of the main text). Pressure variations are expected to induce a very small change in those values because both fluid and solid are only weakly compressible in the liquid-type fluid domain (from ~500 to 5000 bar; *e.g.*, Oelkers *et al.*, 2009; Pokrovski *et al.*, 2015). It is impossible at present to quantitatively predict the effect of temperature on Au solubility and partitioning in sulfarsenides. Based on *i)* natural observations of generally

larger enrichment by Au (and As) of lower-temperature arsenopyrite (and arsenian pyrite) (see Table S-11 and associated references), and *ii)* experimental evidence of enhanced Au uptake from the fluid by arsenian pyrite (200–300 °C, Fleet and Mumin, 1997; Kusebauch *et al*., 2019; Filimonova *et al*., 2020), it is expected that lower temperatures, more typical of epithermal and sediment-hosted gold deposits, may further favour redox reactions Eq. S-10 and S-11, as well as analogous reactions for arsenian pyrite.

Supplementary Tables

Table S-1 Hydrothermal experiments for Au-bearing pyrite, arsenopyrite and löllingite synthesis at 450 °C and 700 bar: initial solid and fluid composition, final solid phase composition, Au solid-phase concentrations and fraction of chemically bound Au, measured by XANES, EPMA and LA-ICPMS (errors 1 s.d.)[a].

Run	days	Initial solids composition (mol %)	Aqueous solution composition (mol/kg H_2O)	Final major phase mean composition SEM, EPMA	Minor phases SEM, EPMA	Au, ppm in solid XANES (±20 %)	% Au bound (±5 %)	Au, ppm in major phase EPMA (pts)	Au, ppm in major phase LA-ICPMS (pts)	As, wt. % in major phase EPMA (pts)
Gold capsule experiments										
MA1	30	Fe_2O_3(14.0) + As(57.0) + S(29.0)	NaCl(2.2)	Apy, $Fe_{0.99}As_{1.03}S_{0.98}Au_{0.003}$	As_2O_3, FeS, NaCl, Au	3670	79	4000 ± 1700 (34)	2690 ± 1020 (8)	45.4 ± 1.7 (34)
MA2	30	Fe_2O_3(14.7) + As(57.0) + S(28.3)	NaOH(2.2)	Apy, $Fe_{0.98}As_{1.07}S_{0.94}Au_{0.007}$	AsS, Au, FeO	4110	64	8200 ± 4500 (34)	5510 ± 2300 (3)	47.5 ± 2.3 (34)
MA3	30	FeS(46.1) + As(45.1) + S(8.9)	NaCl(2.2)	Apy	As_2O_3, Au	1630	65	–	–	–
MA4	30	FeS(44.1) + As(44.9) + S(11.0)	NaOH(2.2)	Apy	As_2O_3, Au	5420	65	–	–	–
LO1	73	Fe_2O_3(13.8) + As(86.2)	NaOH(2.0)	Lo, $Fe_{1.00}As_{2.00}$	As_2O_3, As	241	35	<200 (10)	170 ± 170 (10)	72.2 ± 0.3 (10)
LO2	81	Fe_2O_3(13.2) + As(81.3) + S(5.5)	NaOH(2.0)	Lo, $Fe_{0.97}As_{1.79}S_{0.21}Au_{0.03}$	–	1440	>90	20,000 ± 15,000 (22)	3700 ± 2200 (11)	66.3 ± 4.0 (22)
LO3	81	Fe(33.9) + As(66.1)	NaOH(2.0)	Lo, $Fe_{1.03}As_{1.97}Au_{0.002}$	FeO, Au	1500[c]	23	1500 ± 500 (10)	800 ± 200 (10)	71.1 ± 1.0 (10)
LO4	73	Fe(30.6) + As(63.6) + S(5.9)	NaOH(2.0)	Lo, $Fe_{1.02}As_{1.88}S_{0.10}Au_{0.001}$	FeAsS[b], FeO	1200	70	1200 ± 800 (9)	2970 ± 690 (20)	68.9 ± 1.3 (9)
LO5	81	FeS(48.1) + S(49.4) +As(2.4)	NaCl(2.3) + HCl(0.1)	Py	–	208	8	–	–	–
LO6	73	FeS(47.2) + S(47.5) + As(5.3)	NaCl(2.3) + HCl(0.1)	Py, $Fe_{1.00}S_{1.97}As_{0.03}$	As_2O_3	284	35	<300 (19)	31 ± 21 (18)	1.8 ± 1.5 (19)[d]
Batch reactor experiments										
CE1	9	FeS(49) + As(51)	NaCl(1.2) + HCl(0.06) + S(0.1)	Apy	–	–	–	–	–	–
CE2	20	FeS(49) + As(51)	NaCl(1.2) + HCl(0.06) + S(0.1)	Apy, $Fe_{1.01}As_{1.03}S_{0.96}$	NaCl	203	62		464 ± 403 (22)	46.5 ± 2.4 (5)
CE3	20	FeAsS(100)	NaCl(1.2) + HCl(0.06) + S(0.1)	Apy	NaCl, Au	–	–	–	–	–
CE4	19	FeS_2(100)	$K_2S_2O_3$(0.5) + HCl(0.2)	Py, $Fe_{1.00}S_{2.00}$	Au	47	88		0.1-80 (4)	<0.06 (6)
CE5	19	FeS_2(100)	$K_2S_2O_3$(0.5) + HCl(0.2) + $As(OH)_3$(0.15)	Py, $Fe_{1.00}S_{2.00}$	Au	42	>97		0.1-32 (14)	0.09 ± 0.06 (17)
CE6	20	FeS(50) + As(50)	Pure H_2O	Apy	FeS, As	–	–	–	–	–

[a] XANES detection limit is ~1 ppm Au; EPMA detection limit ~200 ppm Au; LA-ICPMS detection limit ~0.1 ppm Au; '–' = not analysed; chemical formulas are recalculated from EPMA analyses on a three-atom basis.

[b] EPMA spot analyses of the minor arsenopyrite phase (<5 % of the major löllingite phase), yielded 2000 ± 1500 ppm Au and 46.4 ± 4.9 wt. % As, with average 3-atom-basis formula of $Fe_{1.06}As_{1.06}S_{0.88}Au_{0.002}$ (8 pts).

[c] LO3 used as the standard (1500 ppm Au by EPMA) for Au concentration determination in the other löllingite-dominated samples using Eq. S-9.

[d] The average As content by LA-ICPMS in the same laser spots as Au in LO6 is 0.72 ± 0.51 wt. % (18 pts), with Au and As contents positively correlated (R^2 = 0.65).

Table S-2 Dry-system experiments for Au-bearing pyrite and arsenopyrite synthesis at 600 °C and <10 bar: initial and final solid phase composition, and Au total solid-phase concentrations measured by XANES, EPMA and LA-ICPMS and fraction of chemically bound Au (XANES).

Run	days	Initial solids (mol %)	Final major phase composition	Minor phases	Au, ppm total XANES (±10 %)	% Au bound XANES (±5 %)	Au, ppm in major phase LA-ICPMS (pts)	As, wt. % in major phase EPMA (pts)
SF1	7	Fe(33.4) + S(33.2) + As(33.4)	Apy	NaCl, Au	4451	<5.0	–	–
SF2	17	Fe(33.5) + S(33.2) + As(33.3)	Apy	NaCl, Au	NA	–	–	–
SF3	17	Fe(33.5) + S(33.2) + As(33.3)	Apy, $Fe_{0.98}As_{1.04}S_{0.980}$	NaCl, Au, FeS, As_2S_3	237	51	189 ± 66 (3)	47.3 ± 0.1 (3)
SF4	17	Fe(33.4) + S(63.2) + As(3.3)	Py, $Fe_{0.95}S_{2.05}As_{<0.001}$	NaCl, As, S, Au	127	83	–	0.023 ± 0.007 (5)
SF5	7	Fe(33.4) + S(63.3) + As(3.3)	Py, $Fe_{0.96}S_{2.04}As_{<0.001}$	NaCl, Au, S, Fe, As	106	100	64 ± 50 (14)	0.035 ± 0.020 (5)

Table S-3 Summary of natural samples of Au-bearing pyrite and arsenopyrite investigated in this study by HR-XANES.

name	Locality, deposit, reference	Au-bearing mineral (mean formula)[a]	Vein and host rock mineralogy[b]	Au XANES[c], ppm	Au LA-ICPMS[c], ppm (nb pts)	% Au bound[d]	As, wt. % (nb pts)
MCB7358	Villeranges (French Massif Central), orogenic, Boiron *et al.* (1989)	Arsenopyrite $Fe_{1.01}As_{0.88}S_{1.10}Sb_{0.01}$	Apy-Py-Qtz-Ank veins in tuff	1300 ± 200	2100 ± 1600 (12)	>98	42.2 ± 1.0 (8)
MCB7358	Villeranges (French Massif Central), orogenic, Boiron *et al.* (1989)	Pyrite $Fe_{1.009}As_{0.005}S_{1.986}$	Apy-Py-Qtz-Ank veins in tuff	61 ± 15	46 ± 33 (15)	>95	2.6 ± 0.8 (15)
MW15	Tabakoroni (West Africa), orogenic, Traoré *et al.* (2016)	Arsenopyrite $Fe_{1.00}As_{0.90}S_{1.10}$	Apy-Py-Qtz-Carb veins and disseminations in metabasalt	47 ± 10	58 ± 56 (7)	>90	43.2 ± 1.6 (6)
JM03	Buesichem (West Africa), orogenic, Parra-Avila *et al.* (2015)	Arsenopyrite $Fe_{1.01}As_{0.90}S_{1.09}$	Py-Apy-Qtz-Carb veins and disseminations in black shale	100 ± 30	272 ± 157 (7)	79	42.7 ± 0.8 (12)
KK03	Gold Strike (Nevada), Carlin, this study and Muntean (2018)	Pyrite $Fe_{0.990}As_{<0.001}S_{2.005}$	Disseminated euhedral grains and framboids in carbonate black shale	16 ± 10	18 ± 16 (8)[e]	45	0.05 ± 0.04 (19)[f] 0.11 ± 0.07 (8)[g]

[a] Mineral mean formulas are from EPMA analyses, other elements represent <0.003 at. %.
[b] Mineral names abbreviations are according to Whitney and Evans (2010): Apy, arsenopyrite; Py, pyrite; Qtz, quartz; Ank, ankerite; Carb, generic carbonate (ankerite-dolomite-calcite).
[c] LA-ICPMS represent the average (±1 s.d.) Au concentration value of those from individual laser ablation spots of different Apy or Py grains, whereas XANES reports the average (±1 s.d.) Au concentration from fluorescence scans obtained on hand-picked samples of the corresponding mineral (Apy or Py) ground and pressed in a pellet to avoid artifacts of sample heterogeneity in XAS spectra acquisition.
[d] Estimated from LCF analyses using, as standards, XANES spectra of Au metal and MCB7358 Apy and Py in which Au in chemically bound in the mineral as demonstrated by FDMNES simulated XANES spectra of Au substituted for Fe^{II} in the FeAsS and FeS_2 structure.
[e] Au average content from LA-ICPMS (<200 ppm by EPMA).
[f] As average contents from EMPA in euhedral pyrite and framboidal pyrite are 0.02 ± 0.01 (7 pts) and 0.11 ± 0.03 (12 pts) wt. % As, respectively.
[g] As average content from LA-ICPMS; no distinguishing between euhedral vs framboidal types could be made because of the too small grain size compared with the ablation spot. The Au and As LA-ICPMS contents are positively correlated (R^2 = 0.94).

Table S-4 Gold local structure in the mineral samples determined by fitting Au L_3-edge EXAFS spectra.

Sample name	Atom	N, atoms	R, Å	σ^2, Å^2	Δe, eV	*R*-factor	chi_{red}^2
MCB7358 Py	S1	3.1 ± 0.5	2.41 ± 0.02	0.006	7.0	0.019	23
	As1	2.9 ± 0.5	2.48 ± 0.01	0.006			
	As2 (Fe2)	2.0 ± 1.0	3.2	0.010			
	S2	6 ± 2	3.7	0.020			
	Fe2	12f	3.9	0.015			
	S3	6f	4.5	0.015			
MCB7358 Apy	S1	1.7 ± 0.5	2.43 ± 0.03	0.003	6.0	0.012	30
	As1	4.5 ± 0.5	2.50 ± 0.02	0.003			
	Fe2 (Au2)	1f	3.3 (3.3)	0.005			
	S2	4f	3.7	0.006			
	As2	4f	4.0	0.005			
	Fe3	4f	4.1	0.005			
MA1 Apy	S1	1.6 ± 0.4	2.45 ± 0.05	0.004	5.0	0.053	82
	As1	4.4d	2.52 ± 0.02	0.004			
	Fe2 (Au2)	1f	3.0 (3.2)	0.005			
	S2	4f	3.8	0.007			
	As2	4f	3.8	0.007			
	Fe3	4f	4.1	0.007			
MA2 Apy	S1	1.5 ± 0.5	2.41 ± 0.10	0.005	5.9	0.040	90
	As1	4.4 ± 0.4	2.51 ± 0.02	0.002			
	Fe2 (Au2)	1f	3.0 (3.2)	0.004			
	S2	4f	3.6	0.007			
	As2	4f	4.1	0.009			
	Fe3	4f	3.8	0.009			
MA3 Apy	S1	1.2 ± 0.5	2.41 ± 0.15	0.007	5.0	0.040	65
	As1	4.8d	2.50 ± 0.03	0.002			
	Fe2 (Au2)	1f	3.6 (3.5)	0.003			
	S2	4f	3.6	0.013			
	As2	4f	3.8	0.005			
	Fe3	4f	4.0	0.005			
MA4 Apy	S1	1.2 ± 0.5	2.44 ± 0.08	0.004	5.0	0.055	100
	As1	4.8d	2.50 ± 0.02	0.002			
	Fe2 (Au2)	1f	3.0 (3.2)	0.003			
	S2	4f	3.7	0.008			
	As2	4f	4.2	0.005			
	Fe3	4f	4.1	0.005			
LO2 Lo	As1	7.4 ± 1.5	2.53 ± 0.01	0.002	5.0	0.036	20
	Fe2	2f	3.06 ± 0.05	0.002			
	As2	8f	3.9	0.007			
	Fe3	8f	4.3	0.007			
	As3	10f	4.8	0.007			
LO4 Lo	As1	6.2 ± 1.5	2.52 ± 0.01	0.0015	5.3	0.043	90
	Fe2	2f	3.00 ± 0.02	0.001			
	As2	8f	4.0	0.005			
	Fe3	8f	4.3	0.007			
	As3	10f	4.8	0.005			
Error (unless indicated)			*±0.1*	*±50 %*	*±2*		

R = Au-S/As/Fe mean distance, N = Au-S/As/Fe coordination number (fixed for the indicated atoms to their crystallographic value based on DFT calculations of FeAsS, FeS_2 and $FeAs_2$ structures), σ^2 = Mean Squared Relative Displacement (MSRD) factor, Δe = non-structural parameter accounting for energy shift between the experimental EXAFS and FEFF calculation, *R*-factor and chi_{red}^2 = statistical criteria of goodness of the total fit in R-space (Newville, 2001). The amplitude reduction factor S_0^2 = 1.00 ± 0.05 as found from fits of model compounds with known Au coordination. For Apy and Py samples, the fitted k-and R-ranges were respectively 2.8-13.0 Å^{-1} and 1.3-4.5 Å, and for Lo samples 2.8-13.0 Å^{-1} and 1.3-5.2 Å (not corrected for phase shift). The number of variables in the fit (N_{var} < 8-10) was much lower than the number of independent points (N_{ind} = 16-23). The Au^0 contribution in MA and LO samples was subtracted from the spectra before EXAFS fitting, based on LCF analyses of XANES spectra. 'f' - N value was fixed in the fit to expected crystallographic value; 'd' - N value for As1 was defined as 6-N_{S1} to increase fit stability, where 6 is the crystallographic value for Au in the Fe-site. Note that the detection limit of As in an S-dominated nearest atomic shell of Au (*e.g.,* in Py) is 0.5 to 1.0 atom, depending on the signal-to-noise spectral characteristics; likewise, the detection limit of S in an As-dominated nearest atomic shell of Au (in Apy and Lo) is from 0.5 to 1.0 atom. Atoms in parentheses for 2nd shell in Apy and Py samples denote possible alternative neighbors, which cannot be discriminated given the fit statistics.

Table S-5 Theoretical and experimental structural parameters of pyrite (FeS_2, $Pa\bar{3}$ space group), arsenopyrite (FeAsS, $P2_1/c$ space group), and löllingite ($FeAs_2$, *Pnnm* space group) and mean interatomic distances.

Structural parameters	Pyrite DFT	Pyrite exp*	Arsenopyrite DFT	Arsenopyrite exp*	Löllingite DFT	Löllingite exp*
a (Å)	5.403	5.418	5.743	5.761	5.313	5.268
b (Å)	5.403	5.418	5.670	5.684	6.000	5.963
c (Å)	5.403	5.418	5.761	5.767	2.894	2.901
α (°)	90.00	90.00	90.00	90.00	90.00	90.00
β (°)	90.00	90.00	111.97	111.72	90.00	90.00
γ (°)	90.00	90.00	90.00	90.00	90.00	90.00
Fe-S (Å)	2.254	2.262	2.199	2.231	-	-
Fe-As (Å)	-	-	2.406	2.397	2.380	2.373
S-S (Å)	2.197	2.177	-	-	-	-
As-S (Å)	-	-	2.416	2.374	-	-

* Experimental data for pyrite, arsenopyrite and löllingite are from Brostigen and Kjekshus (1969), Bindi *et al*. (2012) and Ondrus *et al*. (2001), respectively.

Table S-6 Optimised unit cell parameters and average bond lengths involving Au atom (in Å, β angle in degree) of gold-bearing pyrite, arsenopyrite, and löllingite models. Angles other than the β arsenopyrite angle are all equal to 90.0°. The reported interatomic distances are average values over the 1st or 2nd shell atomic cluster.

Model	*a*	*b*	*c*	β	Au-S	Au-As	Au-Fe/Au/As*
Fe-site [AuS_6] Py	5.421	5.421	5.421	-	2.454	-	3.850 (12Fe)
Fe-site [$AuAs_3S_3$] Py	5.443	5.443	5.443	-	2.434	2.495	3.905 (12Fe)
Fe-site [$AuAs_3S_3$] Apy	5.775	5.687	5.793	111.92	2.460	2.517	3.104 (Fe), 3.626(Fe)
Fe-site [$AuAs_3S_3$ + $AuAs_6$] Apy Au#1	5.808	5.715	5.833	112.13	2.454	2.529	3.436(Fe), 3.390(Au)**
Fe-site [$AuAs_3S_3$ + $AuAs_6$] Apy Au#2	5.808	5.715	5.833	112.13	-	2.497	3.578(Fe), 3.390(Au)**
Fe-site [$AuAs_3S_3$ + $AsAs_3S_3$] Apy	5.802	5.715	5.821	112.00	2.500	2.520	3.237(As), 3.627(Fe)
Fe-site [$AuAs_6$] Apy	5.786	5.711	5.810	112.51	-	2.515	2.909(Fe), 3.666(Fe)
S-site [$AuAsFe_3$] Apy	5.761	5.689	5.787	112.30	-	2.423	2.483(Fe)
As-site [$AuSFe_3$] Apy	5.765	5.681	5.775	112.32	2.407	-	2.541(Fe)
Fe-site [$AuAs_6$] Lo	5.288	6.016	2.937	-	-	2.546	3.058 (2Fe)

* The identity and number of 2nd shell neighbouring atoms are indicated in brackets.
** #1 and #2 denote each individual Au site in the combined structure.

Table S-7 Optimised structural parameters of $AuAs_2$ and AuAsS fictitious solids built from the pyrite, löllingite and arsenopyrite structures.

Structural parameter	$AuAs_2$ (Py-struct)	$AuAs_2$ (Lo-struct)	AuAsS (Apy-struct)
a (Å)	6.311	4.956	5.873
b (Å)	6.311	6.341	8.530
c (Å)	6.311	4.134	5.867
α (°)	90.00	90.00	90.00
β (°)	90.00	90.00	98.15
γ (°)	90.00	90.00	90.00
Au-S (Å)	-	-	2.493, 2.497
Au-As (Å)	2.641 (×6)	2.626 (×2), 2.646 (×4)	2.514 (×2)

Table S-8 Fluid pH, oxygen fugacity and Au chemical speciation and concentration in the hydrothermal experiments of this study conducted at 450 °C and 700 bar, and derived mineral/fluid empirical partition coefficients for chemically bound gold.

Run	Au-bearing phase	pH fluid[c]	$\log_{10} f_{O_2}$ (bar) *vs* NNO[c]	As^{III}, wt. % in fluid, calc[c]	Au^{I}, ppm in fluid, calc[c]	Major Au aqueous species in fluid, calc[c]	Au^{I}, ppm in fluid, exp[b]	Au, ppm bound in solid[a]	Empirical partition coefficient D_{Au} solid/fluid[d]
Gold capsule experiments									
MA1	Apy	6.2	2.4	21.1	0.022	$Au(HS)_2^-$, AuOH, AuHS	–	2896	1.32×10^5
MA2	Apy	7.2	2.6	28.8	0.078	$Au(HS)_2^-$, AuHS	–	2627	33,680
MA3	Apy	5.8	1.3	1.6	6.07	$Au(HS)_2^-$	–	1061	175
MA4	Apy	7.8	1.1	1.6	811	$Au(HS)_2^-$	–	3520	4.5
LO1	Lo	8.5	1.3	16.8	0.006	AuOH	–	85	14,169
LO2	Lo	8.4	1.3	11.9	0.31	$Au(HS)_2^-$	–	1297	4229
LO3	Lo	11.1	-3.2	0.06	6×10^{-4}	AuOH	–	345	6.24×10^5
LO4	Lo	9.1	0.0	4.7	14.3	$Au(HS)_2^-$	–	828	58
LO5	Py	5.0	1.2	1.4	1.5	$Au(HS)_2^-$	–	17	11
LO6	Py	5.0	1.2	1.4	1.5	$Au(HS)_2^-$	–	160	109
Batch reactor experiments									
CE1	Apy	5.4	0.9	0.42	0.26	$Au(HS)_2^-$, AuHS	0.4	–	–
CE2	Apy	5.4	1.0	0.48	0.30	$Au(HS)_2^-$, AuHS	0.4	126	416
CE3	Apy	6.1	1.0	0.48	0.61	$Au(HS)_2^-$	0.5	–	–
CE4	Py	6.0	3.1	–	554	$Au(HS)_2^-$, $Au(HS)S_3^-$	237	42	0.08
CE5	Py	6.0	3.1	1.22	547	$Au(HS)_2^-$, $Au(HS)S_3^-$	81	42	0.08
CE6	Apy	5.3	-0.5	0.09	0.011	AuHS, AuOH	0.06	–	–
Error		*±0.2*	*±0.2*	*±50 %*	*±50 %*		*±50 %*	*±10 %*	*±50 %*

[a] Calculated as the product of Au^{I} fraction and the total Au concentration from edge height of fluorescence spectra (Eq. S-9).
[b] Measured in the quenched fluid phase recovered and processed after batch-reactor experiments.
[c] Predicted in the fluid phase at 450 °C and 700 bar by thermodynamic equilibrium calculations with the HCh software (Shvarov, 2008) using the initial system composition and the thermodynamic properties of aqueous and mineral species reported in Pokrovski *et al*. (2002a, 2002b, 2019), Perfetti *et al*. (2008), and Kokh *et al*. (2016, 2017, 2020). NNO = Nickel-Nickel Oxide, $\log f_{O_2}$ (NNO) = –24.9 at 450 °C and 700 bar.
[d] Empirical partition coefficient $D_{Au} = C_{Au}$ in solid / C_{Au} in fluid, where C_{Au} is Au dissolved concentration in the corresponding phase (ppm units); for consistency, theoretical Au fluid-phase concentrations were used in D_{Au} calculations for all runs.
'–' not available or not measured.

Table S-9 Derivation of thermodynamic constants for arsenopyrite/fluid partitioning and solubility of chemically bound gold in arsenopyrite from hydrothermal experiments of this study at 450 °C and 700 bar.

Run	Mole fraction of bound Au in Apy, $\log_{10}X_{Au}$	Activity of $Au(HS)_2^-$ in fluid, $\log_{10}a_{Au}$	Therm. partition coefficient [a] $\log_{10}Q_{Apy/Fluid}$	pH fluid 450 °C, 700 bar	Oxygen fugacity, $\log_{10}f_{O_2}$ (bar)	Activity of $As(OH)_3$ in fluid, $\log_{10}a_{As(OH)_3}$	Activity of H_2S in fluid, $\log_{10}a_{H_2S}$	$\log_{10}K$(10a) Au partition [b]	$\log_{10}K$(10b) Au solubility [c]
MA1	-2.62	-8.13	5.50	6.2	-22.58	0.70	-2.19	-18.0	-22.3
MA2	-2.66	-7.01	4.35	7.2	-22.33	0.86	-2.15	-18.1	-22.4
MA3	-3.06	-5.19	2.14	5.8	-23.62	-0.60	-0.43	-18.4	-22.6
MA4	-2.54	-3.08	0.54	7.8	-23.84	-0.77	-0.33	-17.8	-22.1
CE2	-3.98	-6.66	2.67	5.4	-23.99	-1.16	-0.89	-18.6	-22.8
Error	*±0.10*	*±0.20*	*±0.27*	*±0.2*	*±0.20*	*±0.20*	*±0.20*	*±0.3*	*±0.3*
Mean								**-18.2 ± 0.3**	**-22.4 ± 0.3**

[a] Thermodynamic partition coefficient of dissolved Au between arsenopyrite and fluid, $Q_{Apy/fluid} = X_{Au}$ (Apy)/$a_{Au(HS)_2^-}$ (fluid).

[b] reaction (S-10a): $Au(HS)_2^- + H^+ + 1.5\ As(OH)_3 = [AuAs_{1.5}S_{0.5}]_{Apy} + 1.125\ O_2 + 1.5\ H_2S + 2.25\ H_2O$.

[c] reaction (S-10b): $Au(metal) + 1.5\ As(OH)_3 + 0.5\ H_2S = [AuAs_{1.5}S_{0.5}]_{Apy} + 0.875\ O_2 + 2.75\ H_2O$.

Table S-10 Derivation of thermodynamic constants for löllingite/fluid partitioning and solubility of chemically bound gold in löllingite from hydrothermal experiments in S-bearing systems of this study at 450 °C and 740 bar.

Run	Mole fraction of bound Au in Lo, $\log_{10}X_{Au}$	Activity of $Au(HS)_2^-$ in fluid, $\log_{10}a_{Au}$	Therm. partition coefficient [a] $\log_{10}Q_{Lo/Fluid}$	pH fluid 450 °C, 740 bar	Oxygen fugacity, $\log_{10}f_{O_2}$ (bar)	Activity of $As(OH)_3$ in fluid, $\log_{10}a_{As(OH)_3}$	Activity of H_2S in fluid, $\log_{10}a_{H_2S}$	$\log_{10}K$(11a) Au partition [b]	$\log_{10}K$(11b) Au solubility [c]
LO2	-2.87	-6.38	3.51	8.35	-23.69	-0.10	-2.42	-34.2	-38.2
LO4	-3.06	-4.79	1.74	9.07	-24.96	-1.04	-1.77	-34.3	-38.4
Error	*±0.20*	*±0.20*	*±0.30*	*±0.20*	*±0.20*	*±0.20*	*±0.20*	*±0.5*	*±0.5*
Mean								**-34.3 ± 0.5**	**-38.3 ± 0.5**

[a] Thermodynamic partition coefficient of dissolved Au between löllingite and fluid, $Q_{Lo/Fluid} = X_{Au}$ (Lo)/$a_{Au(HS)_2^-}$ (fluid).

[b] reaction (S-11a): $Au(HS)_2^- + H^+ + 2.0\ As(OH)_3 = [AuAs_2]_{Lo} + 1.75\ O_2 + 2\ H_2S + 2.5\ H_2O$.

[c] reaction (S-11b): $Au(metal) + 2.0\ As(OH)_3 = [AuAs_2]_{Lo} + 1.5\ O_2 + 3.0\ H_2O$.

Table S-11 Short compilation of data on invisible gold tenors in arsenopyrite (and associated löllingite and pyrite, where available) from selected representative hydrothermal gold deposits worldwide considered in Fig. 4 of the main text.

Deposit name, locality	major mineral assemblage	Au contents in Apy (Py, Lo), entire range, ppm	mean or common Au contents, ppm (where reported)	Analytical method	T °C	P, kbar	other remarks	reference
Sunrise Dam, Yilgarn Craton, West Australia	Apy-Py	<1 to 5767	562	LA-ICPMS	-	-	D4a stage, As-deficient Apy	Sung *et al.* (2009)
Salsigne, France	Apy-Po(-Lo) Apy-Po(-Py) Apy-Py	500-800 <100 <10	650	INAA	400-450 150-250 150-250	>1 <1 <1	1st stage (biotite) 3rd stage (chlorite) 6th stage (quartz-sulfide veins)	Boiron *et al.* (1990) Demange *et al.* (2006)
Buesichem, West Africa	Apy(-Py)	130-600	272	LA-ICPMS	-	-	graphite-rich shale	Parra-Avila *et al.* (2015)
Tabakoroni, West Africa	Apy-Py(-Po)	2-176	57	LA-ICPMS	-	-		Traoré *et al.* (2016)
Campbell, Red Lake, Canada	Apy-Py	122-5600		SIMS	-	-	peak metamorphism, garnet	Tarnocai *et al.* (1997)
Bhukia-Jagpura, Southern Rajasthan, India	Apy-Lo-Py	0.3-10 35-51 (Lo)		LA-ICPMS	380-570	3-5	peak metamorphism, followed by different retrograde phases	Deol *et al.* (2012)
Ashanti belt deposits, Ghana, West Africa	Apy-Py-Po	<1-2500 <100 (Py)	190-280 10 (Py)	SIMS	300-450	2-5		Mumin *et al.* (1994) Obertur *et al.* (1997)
Enisei and Kolyma districts, Siberia, Russia	Apy(-Py-Po)	<0.1-2300 <0.1 to 13 (Py)		INAA, SIMS	-	-	As-depleted Apy	Genkin *et al.* (1998)
Villerange, Massif Central, France	Apy-Py	100-1200 <100 (Py)		INAA	150-250	1	quartz-ankerite veins, f_{O_2} <HM	Boiron *et al.* (1989)
Wattle Dam and Mariners, West Australia	(Fe,Ni,Co)As	<1-500 (NiAs)	20-40 (NiAs)	LA-ICPMS	-	-	dominant NiAs and NiAsS	Le Vaillant *et al.* (2018)
Tanami province, North-Central Australia	Apy(-Py)	2-4500 <4 (Py)	10-300 0.1-1 (Py)	LA-ICPMS	-	-	As-enriched Apy	Cook *et al.* (2013)
Vorontsovka, Northen Urals, Russia	Apy(-Py) early Apy-Lo(-As) late	<50-2500 <50-12300		EPMA	270-400 250-370	0.2-0.6 0.2	Early: Apy(-sulfosalt-Py) in marble, logf_{S2} = -7 to -9; As/S in Apy = 0.89 ± 0.04; Late: Apy-Lo-As in siltstone, logf_{S2} = -12 to -17, As/S in Apy = 1.04 ± 0.03	Kovalchuk *et al.* (2019)
El Valle, NW Spain	Apy-Py(-Mc)	<250-4700 <250-800 (Py)	1300-3000	EPMA	200-250	-	Multiple Apy and Py generations, all Apy with similar Au contents, in marble-hosted oxidised and argillised skarn	Cepedal *et al.* (2008)

Supplementary Figures

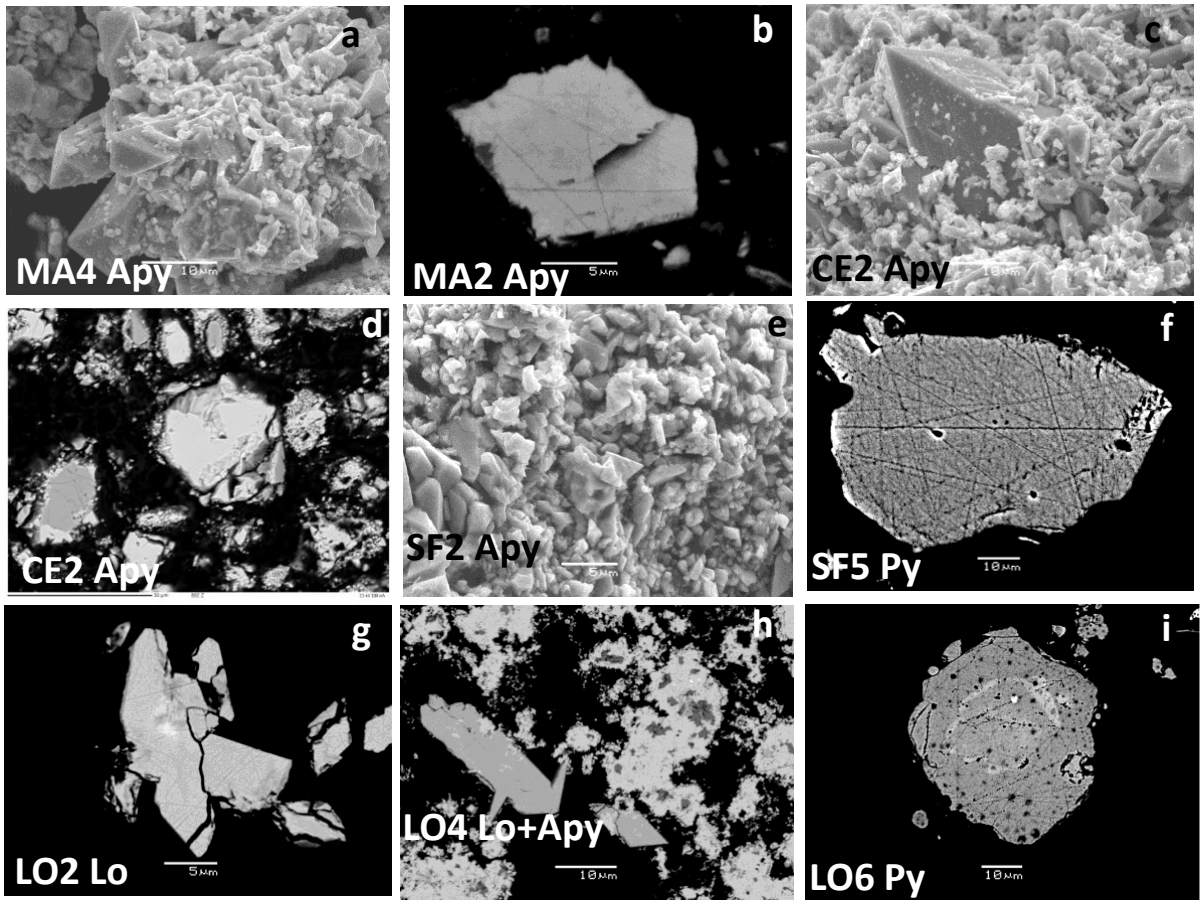

Figure S-1 Scanning Electron Microscopy (SEM) photomicrographs in **(b, d, f–i)** back scattered electron and **(a, c, e)** secondary electron modes of representative synthetic Au-bearing arsenopyrite, pyrite and löllingite samples (see Tables S-1 and S-2 for sample identity and composition). **(a, c, d)** Arsenopyrite crystal agglomerates of variable size as seen in powder samples recovered from the indicated experiments. **(b, d, f)** Individual euhedral arsenopyrite or pyrite grains as seen in polished sections of the indicated samples. In **(d)** arsenopyrite is bright and unreacted FeS is grey. In **(g)** bright spots within the löllingite crystals indicate high gold contents (>1 wt. %). In **(h)** light-gray and dark-gray crystals are löllingite (dominant) and arsenopyrite (minor), respectively. In **(i)**, the light grey rim inside a pyrite crystal indicates unreacted or transformed to pyrrhotite FeS.

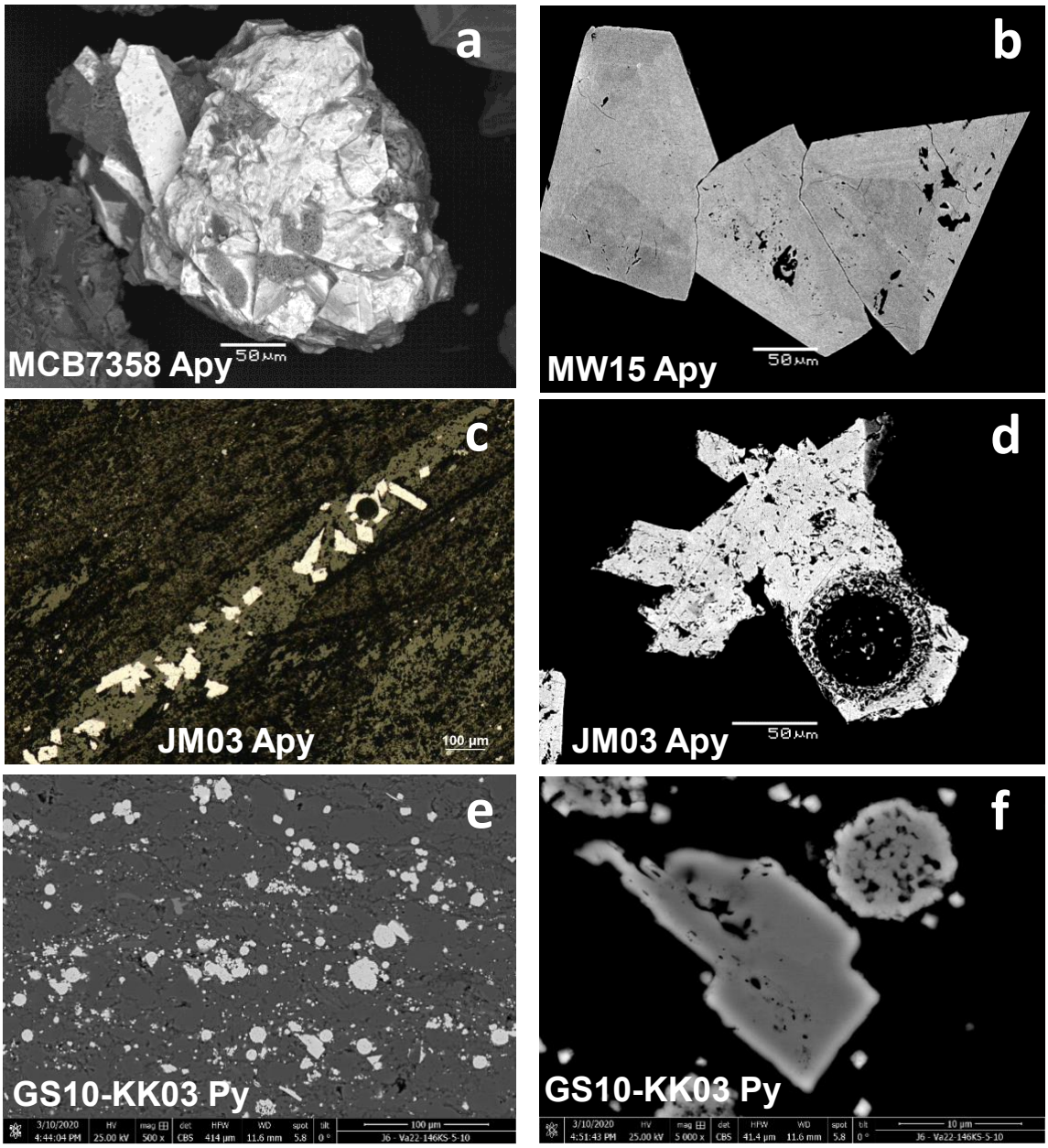

Figure S-2 Scanning Electron Microscopy (SEM) photomicrographs in back-scattered electron mode of representative natural Au-bearing arsenopyrite and pyrite (see Table S-3 for sample identity and composition). **(a, b)** grains of the indicated arsenopyrite samples from the Villeranges and Tabakoroni orogenic deposits, hand-picked for preparation of XAS samples. **(c)** Euhedral crystals of arsenopyrite in a quartz-carbonate vein in black shale and **(d)** a zoom on a LA-ICPMS-shot crystal from the Buesichem orogenic deposit. **(e)** Disseminated grains of arsenian pyrite from the Gold Strike Carlin-type deposit and **(f)** a zoom showing two types of pyrite grains: agglomerates of small crystals and larger euhedral crystals.

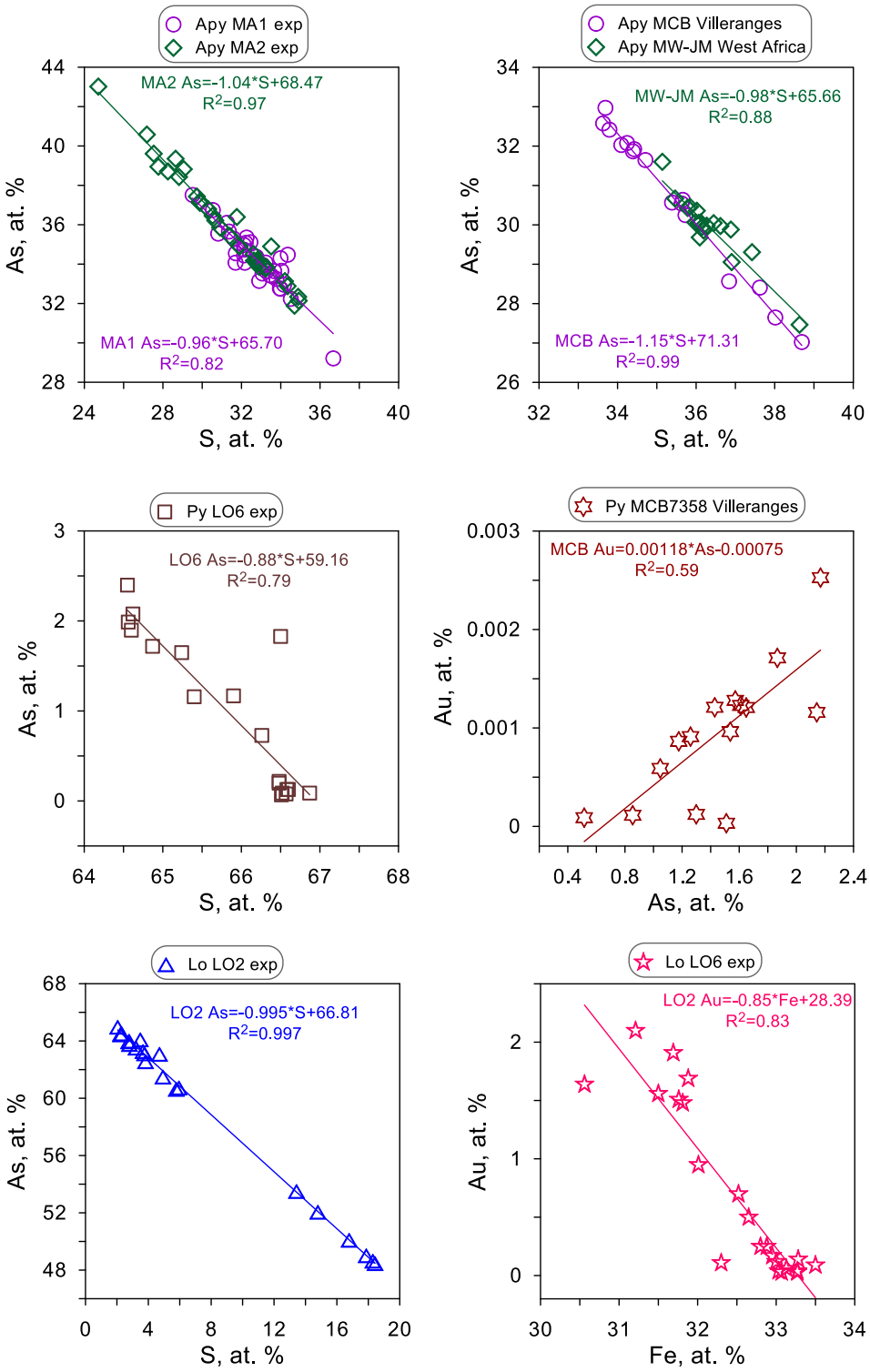

Figure S-3 Examples of As-S, Au-As and Au-Fe elemental correlations in the indicated experimental (exp) and natural (nat) samples of arsenopyrite (Apy), pyrite (Py) and löllingite (Lo) analysed by EPMA or LA-ICPMS (see section 2.1 for details). Symbols stand for microanalytical data points whereas the lines represent linear regression through the data with indicated regression coefficients and squared correlation coefficient (R^2). It can be seen that all samples investigated show very good As-S negative correlations with a slope close to the stoichiometric value of –1 indicative for As^{-I}-to-S^{-I} substitution in the structure of the three minerals. Au is positively correlated with As in arsenian Py, in agreement with detection of Au-As bonds by XAS, and is negatively correlated with Fe in Au-rich löllingite, indicating a substitution to the Fe site, as demonstrated by XAS in this study.

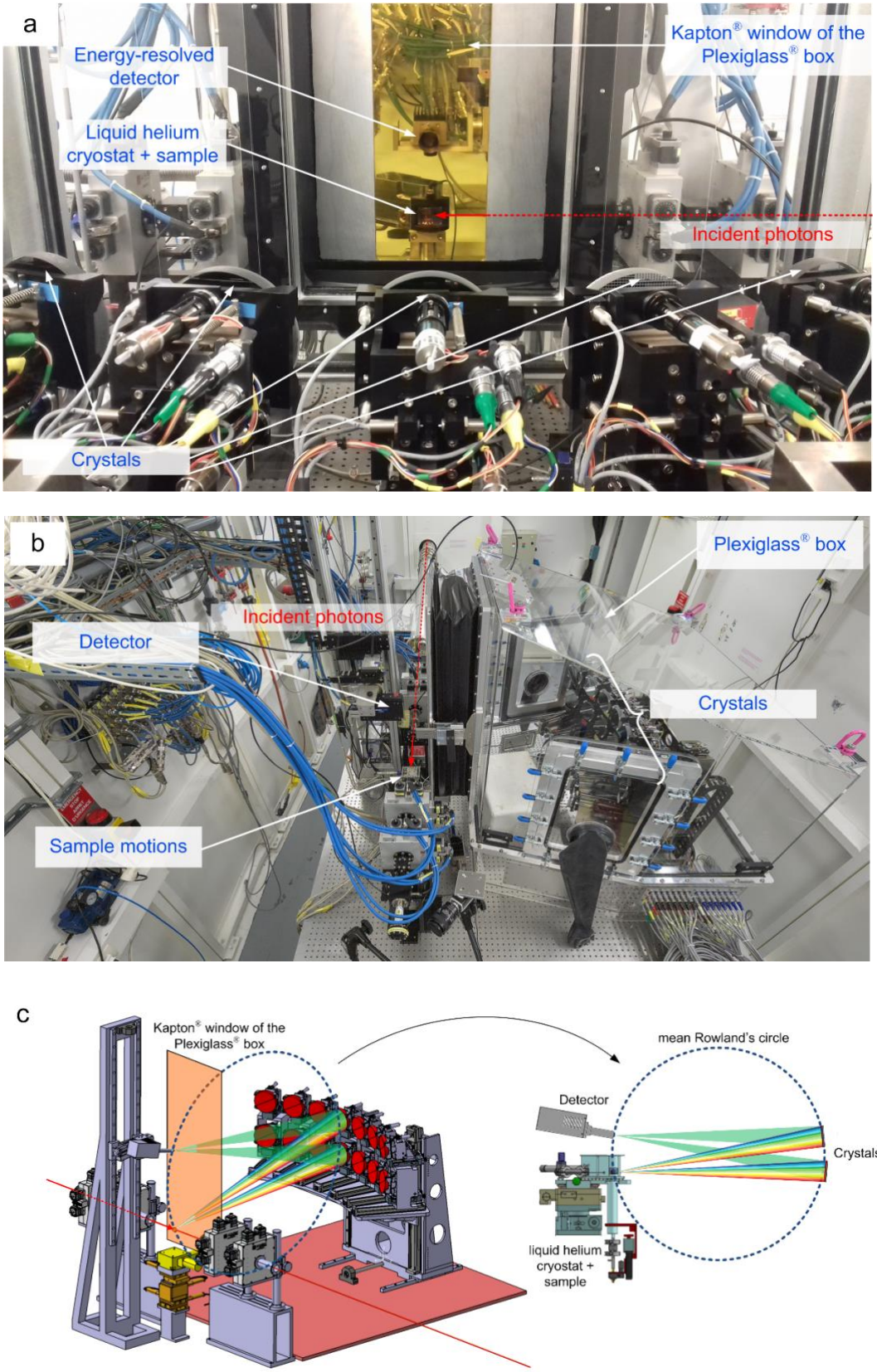

Figure S-4 HERFD-XAS experimental set-up. Photos of the setup **(a)** during an experiment and **(b)** during preparation and alignment stage. **(c)** Schematic view of the crystal analysers and setup overall geometry.

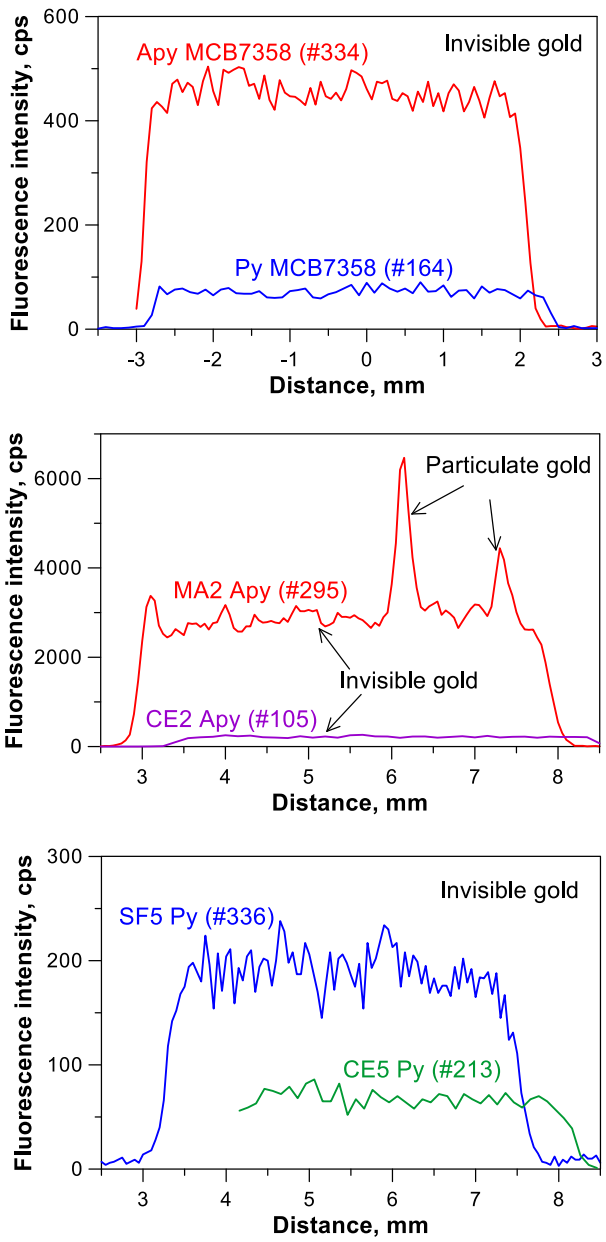

Figure S-5 Examples of typical X-ray fluorescence intensity scans at 12.00 keV (above Au L_3-edge, in counts per second, cps) through the sample height for representative Au-bearing arsenopyrite and pyrite samples (see Tables S-1 to S-3 for sample characteristics). The sharp intense peaks are due to large Au particles which could easily be avoided; the relatively flat regions correspond to invisible gold (both nano-particulate and chemically bound) that could accurately be probed by positioning the beam spot at these regions.

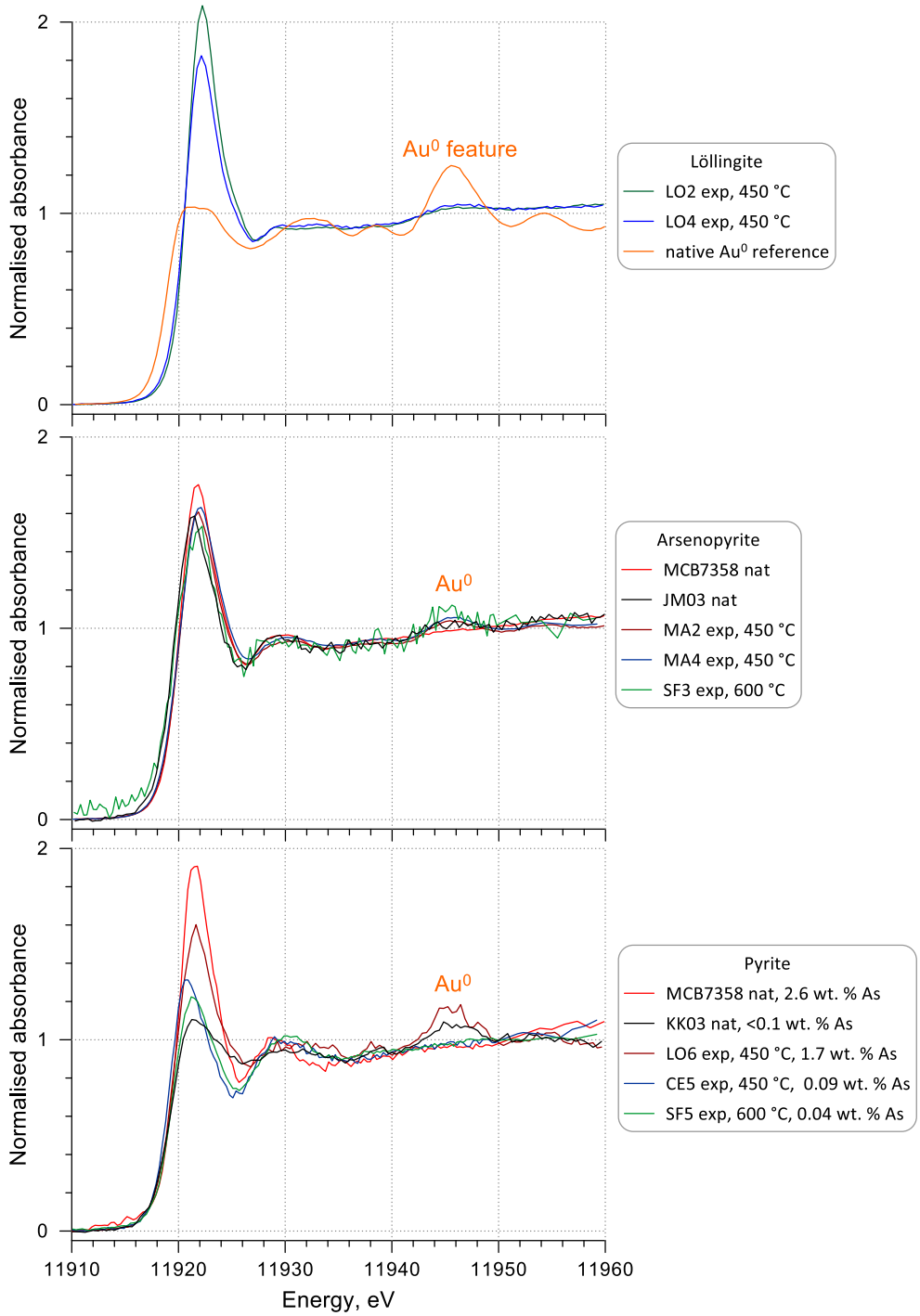

Figure S-6 Examples of Au L_3-edge normalised HR-XANES original spectra of representative samples, complementary to Figure 1 (main text). Note the contribution of metallic gold (Au^0) in some spectra, in particular the intense feature at 11945 eV. The Au^0 contribution could be accurately estimated based on LCF analyses (Fig. S-7, Tables S-1 to S-3) and was subtracted from the original spectra to better analyse the Au-bound environment in the experimental and natural samples shown in Figures 1 and 2 (main text).

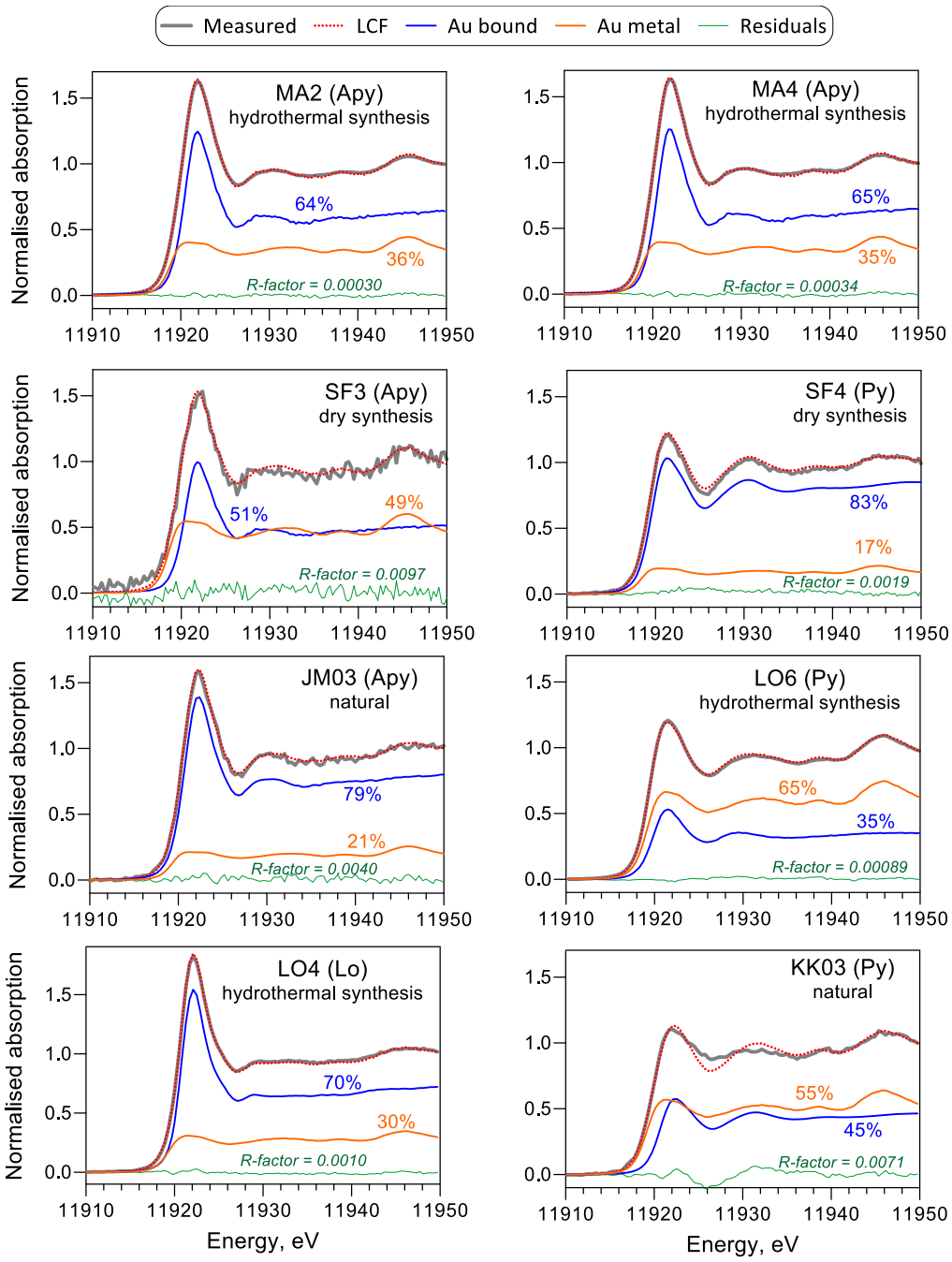

Figure S-7 Examples of Linear Combination Fits (LCF) of HR-XANES spectra of experimental and natural samples of Au-bearing arsenopyrite (Apy), pyrite (Py) and löllingite (Lo) using reference compounds for native gold (Au metal) and chemically bound gold (natural Apy MCB7358 for MA2, MA4, SF3, and JM03; natural Py MCB7358 for LO6; synthetic Au_2S for SF4 and KK03; synthetic Lo LO2 for LO4 sample). Also reported are mole % of metallic and chemically bound Au and the *R*-factor which is a measure of fit quality (*i.e.* the squared difference between the experimental and fitted signals (=residuals) normalised to the experimental signal). A good fit is usually considered to have an *R*-factor value $\leq$0.01 (Ravel and Newville, 2005). The uncertainty of Au^0 fraction determination is ±5 %, and the detection limit is as low as 3 % owing to very contrasting spectral features of Au^0 compared with chemically bound Au, amplified by the high-resolution mode. Note that because of those contrasting features, in particular at 11945 eV, the resulting Au^0 fraction from the LCF is little sensitive to the choice of the second Au-bound standard that does not have such a feature.

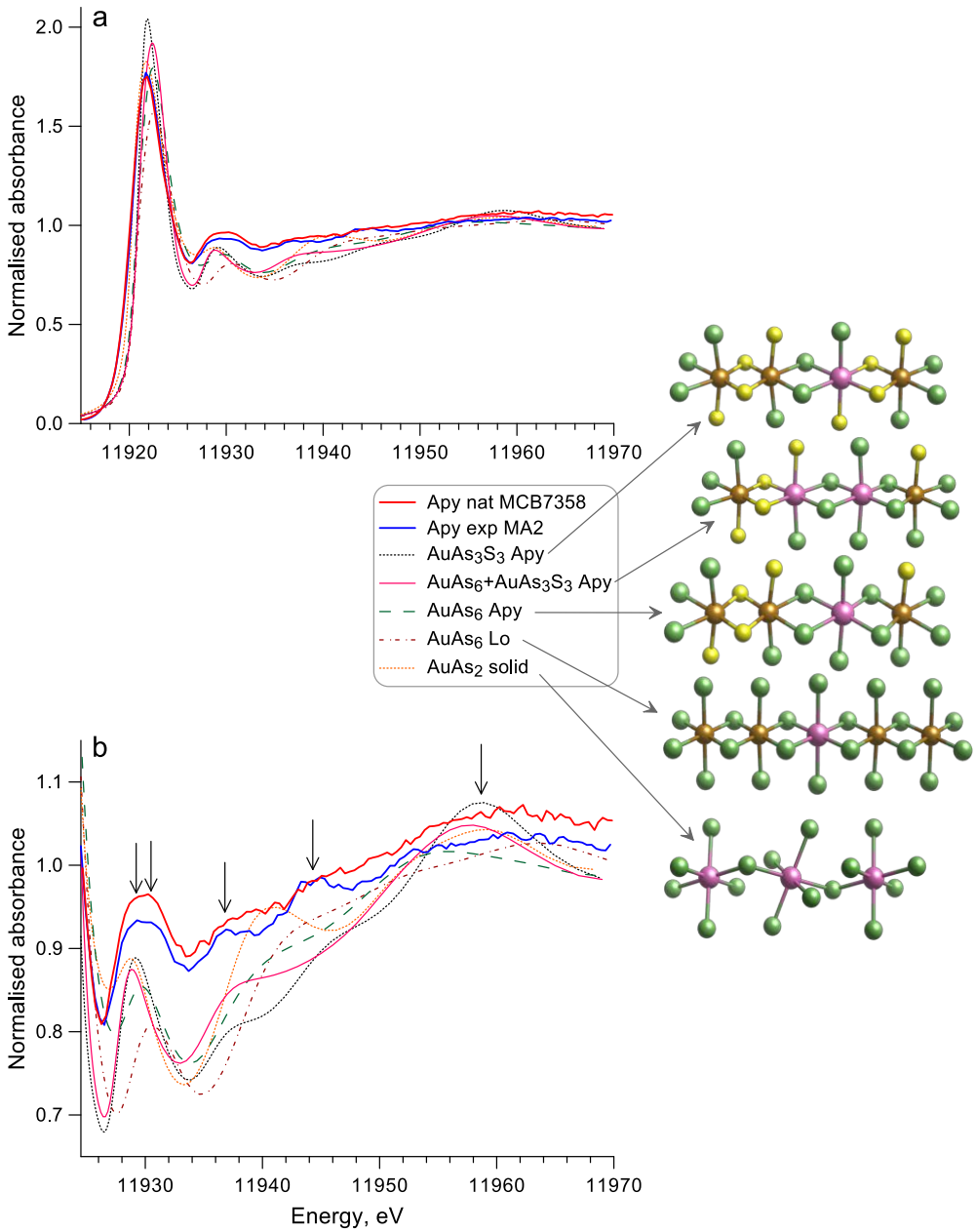

Figure S-8 Comparison of Au L_3-edge HR XANES spectra (complementary to Fig. 2 of the main text) of the best representative experimental (exp) and natural (nat) arsenopyrite samples (MA2 and MCB7358), containing dominantly chemically bound gold, with FDMNES simulated spectra of relaxed crystal structures with different substitution models of Au in the Fe crystallographic site of arsenopyrite, löllingite and gold diarsenide pictured by the corresponding atomic clusters (Au, pink; Fe, brown; S, yellow; As, green). **(a)** Normalised measured and simulated spectra showing a very good match of the position, amplitude and shape of the white line, demonstrating that bound Au is in an octahedral geometry entering the Fe-site. **(b)** Zoom on the post-edge region of the measured and simulated spectra from **(a)**, demonstrating that none of the Au unique positions in the Fe site matches the post-edge features in the experimental spectra (shown by vertical arrows). The ensemble of these features would be compatible with a mixed Au environment in Fe octahedral sites, both arsenopyrite-type and löllingite-type, most likely such as $AuAs_3S_3$ and $AuAs_6$ adjacent clusters simultaneously present in the arsenopyrite mineral structure. The average number of As and S atoms in the first Au shell derived by EXAFS fitting (Table S-4) is in excellent agreement with this structural model.

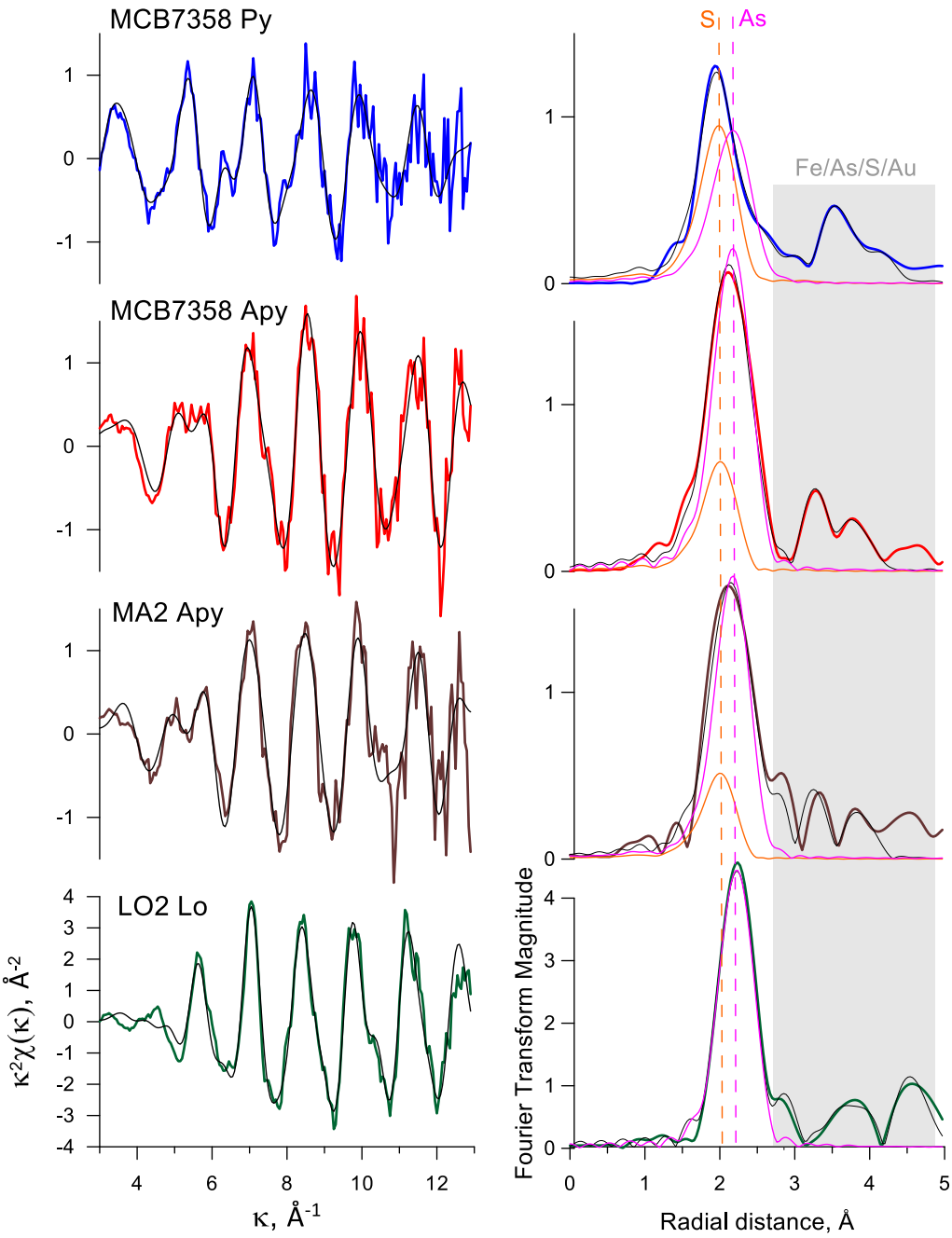

Figure S-9 Au L_3-edge k^2-weighted EXAFS spectra of the indicated natural and experimental pyrite, arsenopyrite and löllingite samples (left panels) and their corresponding Fourier Transforms (not corrected for phase shift, right panels). Note the excellent signal-to-noise spectral statistics allowing their exploitation to at least 13 $Å^{-1}$. Fits are shown by thin black curves. The contributions of the As and S first-shell neighboring atoms to the spectrum are shown by vertical dashed lines in the right-side panels. Note that the nearest Au shell in arsenian pyrite and arsenopyrite contains both S and As atoms with a total coordination number of 6, but with more As atoms than imposed by the mineral stoichiometry. The second shell may contain Fe and/or As (in As-bearing Py), Fe and/or Au (in Apy), and Fe (in Lo), and more distant shells (>3.5 Å) contain multiple overlapping contributions from Fe, As and/or S atoms (shown by the grayed band), in reasonable agreement with the mineral stoichiometry. Our EXAFS data thus confirm the XANES analyses showing that Au substitutes for Fe in octahedral As-enriched sites of the minerals. See Table S-4 for numerical values.

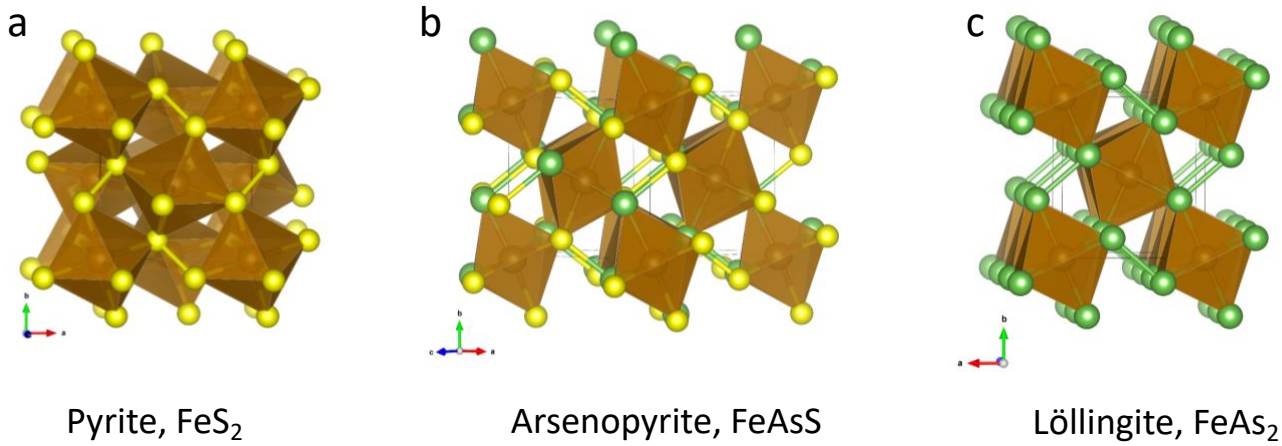

Figure S-10 Structures of **(a)** pyrite, **(b)** arsenopyrite and **(c)** löllingite represented in polyhedral style with the Vesta software (Momma and Izumi, 2011). Iron is in the octahedron center, S and As atoms are yellow and green, respectively.

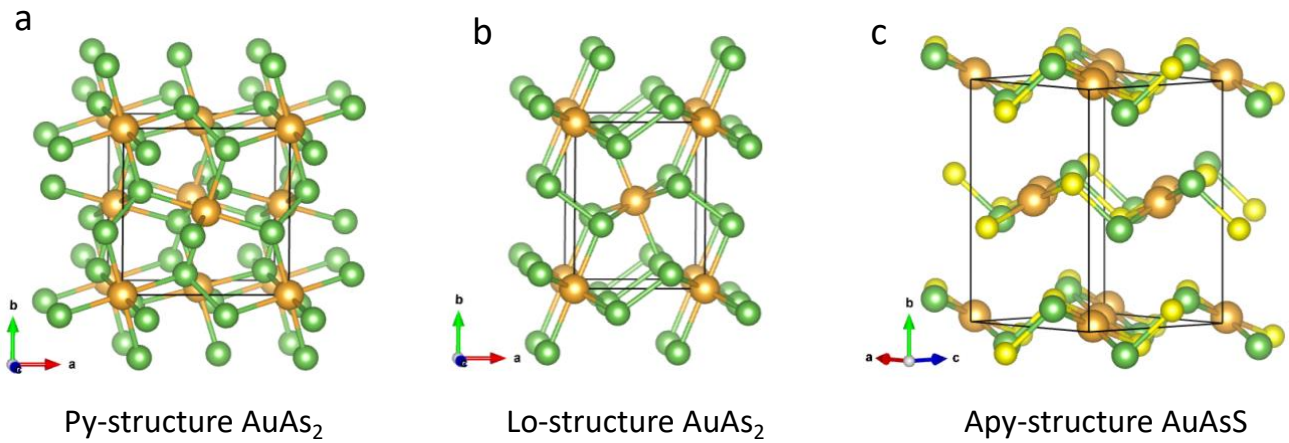

Figure S-11 Structures of $AuAs_2$ and AuAsS fictitious solids built from **(a)** pyrite, **(b)** löllingite and **(c)** arsenopyrite structures, represented in ball-and-stick style with the Vesta software (Momma and Izumi, 2011). Gold, As and S atoms are brown, green and yellow, respectively.

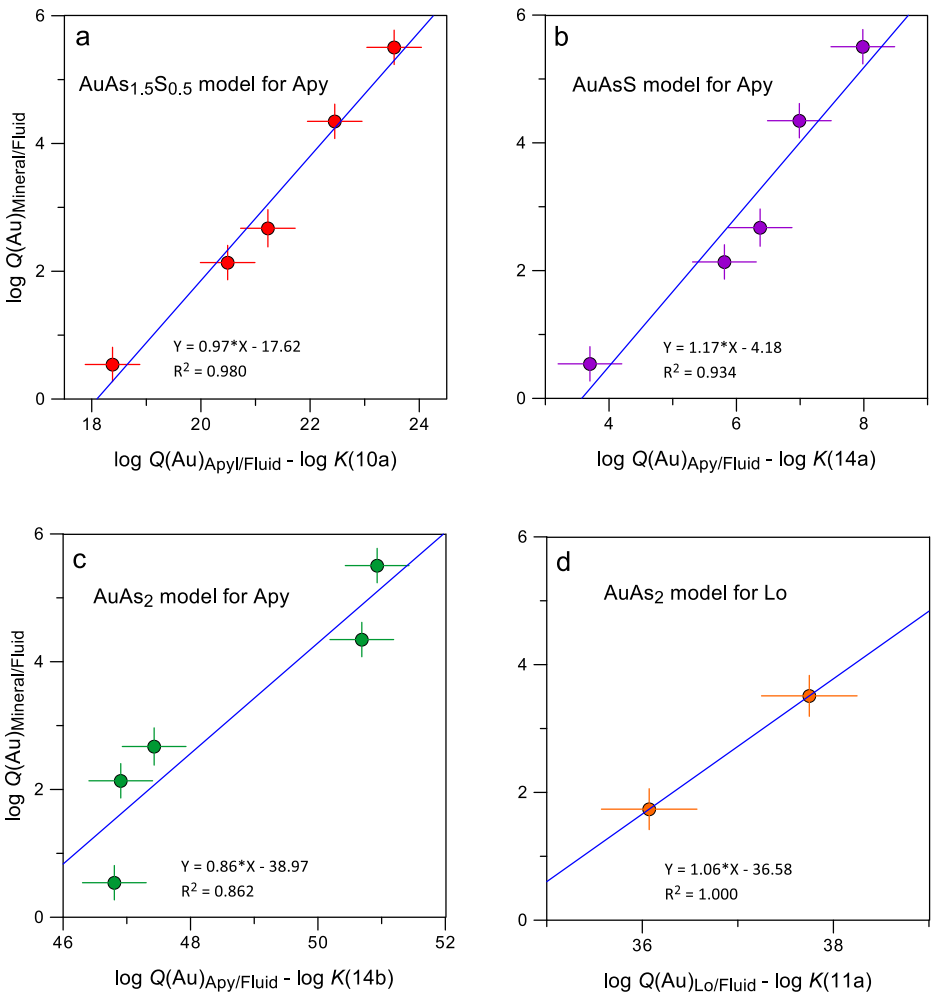

Figure S-12 Comparison of the most relevant thermodynamic models of the equilibrium partitioning of bound gold between arsenopyrite (Apy) or löllingite (Lo) and aqueous fluid at 450 °C and 700 bar. **(a)** The double-site model for Apy (adopted in this study) with two Au atoms in adjacent Fe sites with arsenopyrite-like $AuAs_3S_3$ and löllingite-like $AuAs_6$ environment, which is equivalent to the average Au-bearing end-member of $AuAs_{1.5}S_{0.5}$. **(b)** Simple AuAsS model for Apy in which Au is in a stoichiometric Fe site of arsenopyrite $AuAs_3S_3$, as postulated by Trigub *et al*. (2017). **(c)** Löllingite-like model $AuAs_2$ for Apy in which Au^I is in the Fe site, but surrounded by 6 As atoms as proposed by Merkulova *et al*. (2019). **(d)** A similar $AuAs_2$ model for Lo, in which Au^{II} is surrounded by 6 As atoms in the Fe^{II} site of löllingite as found in this study. Symbols correspond to experimental datapoints for thermodynamic arsenopyrite-fluid and löllingite-fluid partition coefficients and the corresponding reaction constants, calculated using the data of Tables S-9 and S-10 (see section 3.4), whereas the line represents a linear regression through those data points. Compared to the other models **(b, c)**, model **(a)** yields by far the best fit quality of the experimental data points (R^2 = 0.98) and a regression slope (0.97) very close to the theoretical slope of 1. This agreement provides an independent support of the structural XANES and EXAFS data of this study that demonstrate a mixed 'arsenopyrite-löllingite' environment for chemically bound Au in arsenopyrite. Similarly, the $AuAs_2$ model for Lo **(d)** proposed in this study provides the best correspondence with the two experimental datapoints in S-bearing systems from this study, with the regressed slope (1.06) very close to the theoretical slope of 1.

Supplementary Information References

Akinfiev, N.N., Diamond, L.W. (2003) Thermodynamic description of aqueous nonelectrolytes at infinite dilution over a wide range of state parameters. *Geochimica et Cosmochimica Acta* 67, 613–627.

Allibone, A., Teasdale, J., Cameron, G., Etheridge, M., Uttley, P., Soboh, A., Appiah-Kubi, J., Adanu, A., Arthur, R., Mamphey, J., Odoom, B., Zuta, J., Tsikata, A., Pataye, F., Famiyeh, S., Lamb, E. (2002) Timing and structural controls on gold mineralization at the Bogoso gold mine, Ghana, West Africa. *Economic Geology* 97, 949–969.

Amestoy, P.R., Guermouche, A., L'Excellent, J.-Y., Pralet, S. (2006) Hybrid scheduling for the parallel solution of linear systems. *Parallel Computing* 32, 136–156.

Ballo, I., Hein, K.A.A., Guindo, B., Sanogo, L., Ouologuem, Y., Daou, G., Traoré, A. (2016) The Syama and Tabakoroni goldfields, Mali. *Ore Geology Reviews* 78, 578–585.

Bartsch, T., Niehaus, O., Johrendt, D., Kobayashi, Y., Seto, M., Abdala, P.M., Bartsch, M., Zacharias, H., Hoffmann, R.-D., Gerke, B., Rodewalda, U.C., Pöttgen, R. (2015) New quaternary arsenide oxides with square planar coordination of gold(I) – structure, ^{197}Au Mössbauer spectroscopic, XANES and XPS characterization of $Nd_{10}Au_3As_8O_{10}$ and $Sm_{10}Au_3As_8O_{10}$. *Dalton Transactions* 44, 5854–5866.

Bau, R. (1988) Crystal structure of the antiarthritic drug gold thiomalate (myochrysine): A double-helical geometry in the solid state. *Journal of the American Chemical Society* 120, 9380–9381.

Bazarkina, E.F., Pokrovski, G.S., Zotov, A.V., Hazemann, J.-L. (2010) Structure and stability of cadmium chloride complexes in hydrothermal fluids. *Chemical Geology* 276, 1–17.

Benfield, R.E., Filipponi, A., Bowron, D.T., Newport, R.J., Gurman, S.J. (1994) An X-ray absorption study of gold coordination compounds: EXAFS refinements and double-electron excitation background. *Journal of Physics: Condensed Matter* 6, 8449–8468.

Berrodier, I., Farges, F., Benedetti, M., Winterer, M., Brown Jr., G.E., Deveughèle, M. (2004) Adsorption mechanisms of trivalent gold on iron- and aluminum-(oxy)hydroxides. Part 1: X-ray absorption and raman scattering spectroscopic studies of Au(III) adsorbed on ferrihydrite, goethite, and boehmite. *Geochimica et Cosmochimica Acta* 68, 3019–3042.

Bindi, L., Moelo, Y., Leone, P., Suchaud, M. (2012) Stoichiometric arsenopyrite, FeAsS, from La Roche-Balue Quarry, Loire-Atlantique, France: crystal structure and Mössbauer study. *Canadian Mineralogist* 50, 471–479.

Boiron, M.C., Cathelineau, M., Trescases, J.J. (1989) Conditions of gold-bearing arsenopyrite crystallization in the Villeranges basin, Marche-Combrailles shear zone, France. A mineralogical and fluid inclusion study. *Economic Geology* 84, 1340–1362.

Boiron, M.C., Cathelineau, M., Dubessy, J., Bastoul, A.M. (1990) Fluids in Hercynian Au veins from the French Variscan belt. *Mineralogical Magazine* 54, 231–243.

Borisova, A.Y., Pokrovski, G.S., Pichavant, M., Freydier, R., Candaudap, F. (2010) Arsenic enrichment in hydrous peraluminous melts: insights from femtosecond laser ablation - inductively coupled plasma - quadrupole mass spectrometry, and in situ X-ray absorption fine structure spectroscopy. *American Mineralogist* 95, 1095–1104.

Brostigen, G., Kjekshus, A. (1969) Redetermined crystal structure of FeS_2 (pyrite). *Acta Chemica Scandinavica* 23, 2186–2188.

Bunau, O., Joly, Y. (2009) Self-consistent aspects of x-ray absorption calculations. *Journal of Physics: Condensed Matter* 21, 345501.

Cabri, L.J., Newville, M., Gordon, R.A., Crozier, E.D., Sutton, S.R., McMahon, G., Jiang, D.-T. (2000) Chemical speciation of gold in arsenopyrite. *Canadian Mineralogist* 38, 1265−1281.

Campbell, J.L., Papp., T. (2001) Widths of the atomic K-N7 levels. *Atomic Data and Nuclear Data Tables* 77, 1–56.

Cathelineau, M., Boiron, M.-C., Holliger, P., Marion, P., Denis, M. (1989) Gold in arsenopyrites: Crystal chemistry, location and state, physical and chemical conditions of deposition. *Economic Geology Monograph* 6, 328–341.

Cepedal, A., Fuertes-Fuente, M., Martin-Izard, A., Gonzalez-Nistal, S., Barrero, M. (2008) Gold-bearing As-rich pyrite and arsenopyrite from the El Valle gold deposit, Asturias, northwestern Spain. *Canadian Mineralogist* 46, 233–247.

Chase Jr., M.W. (1998) *NIST-JANAF Thermochemical Tables*. Journal of Physical and Chemical Reference Data, Monograph No. 9, Fourth Edition, accessed 4 April 2021, available at http://webbook.nist.gov/chemistry.

Cook, N.J., Ciobanu, C.L., Meria, D., Silcock D., Wade, B. (2013) Arsenopyrite-pyrite association in an orogenic gold ore: Tracing mineralization history from textures and trace elements. *Economic Geology* 108, 1273–1283.

Curis, E., Osán, J., Falkenberg, G., Bénazeth, S., Török, S. (2005) Simulating systematic errors in X-ray absorption spectroscopy experiments: Sample and beam effects. *Spectrochimica Acta* B60, 841–849.

Deditius, A.P., Utsunomiya, S., Renock, D., Ewing, R.C., Ramana, C.V., Becker, U., Kesler, S.E. (2008) A proposed new type of arsenian pyrite: Composition, nanostructure and geological significance. *Geochimica et Cosmochimica Acta* 72, 2919–2933.

Deditius, A.P., Reich, M., Kesler, S.E., Utsunomiya, S., Walshe, J., Chryssoulis, S.L., Ewing, R.C. (2014) The coupled geochemistry of Au and As in pyrite from hydrothermal deposits. *Geochimica et Cosmochimica Acta* 140, 644–670.

Demange, M., Pascal, M.-L., Raimbault, L., Armand, J., Forette, M.C., Serment, R., Touil, A. (2006) The Salsigne Au-As-Bi-Ag-Cu deposit, France. *Economic Geology* 101, 199–234.

Deol, S., Deb, M., Large, R.R., Gilbert, S. (2012) LA-ICPMS and EPMA studies of pyrite, arsenopyrite and löllingite from the Bhukia-Jagpura gold prospect, southern Rajasthan, India: Implications for ore genesis and gold remobilization. *Chemical Geology* 326–327, 72–87.

Driesner, T., Heinrich, C.A. (2007) The system H_2O–NaCl. Part I: Correlation formulae for phase relations in temperature–pressure–composition space from 0 to 1000 °C, 0 to 5000 bar, and 0 to 1 XNaCl. *Geochimica et Cosmochimica Acta* 71, 4880–4901.

Filimonova, O.N., Tagirov, B.R., Trigub, A.L., Nickolsky, M.S., Rovezzi, M., Belogub, E.V., Reukov, V.L., Vikentiev, I.A. (2020) The state of Au and As in pyrite studied by X-ray absorption spectroscopy of natural minerals and synthetic phases. *Ore Geology Reviews* 121, 103475.

Fleet, M.E., Mumin, A.H. (1997) Gold-bearing arsenian pyrite and marcasite and arsenopyrite from Carlin Trend gold deposits and laboratory synthesis. *American Mineralogist* 82, 182–193.

Furuseth, S., Selte, K., Kjekshus, A. (1965) Redetermined crystal structures of $PdAs_2$, $PdSb_2$, PtP_2, $PtAs_2$, $PtSb_2$, α-$PiBi_2$, and $AuSb_2$. *Acta Chemica Scandinavica* 19, 735−741.

Garrity, K.F., Bennett, J.W., Rabe, K.M., Vanderbilt, D. (2014) Pseudopotentials for high-throughput DFT calculations. *Computational Materials Science* 81, 446−452.

Genkin, A.D., Bortinikov, N.S., Cabri, L.J., Wagner, F.E., Stanley, C.J., Safonov, Y.G., McMahon, G., Friedl, J., Kerzin, A.L., Gamyanin, G.N. (1998) A multidisciplinary study of invisible gold in arsenopyrite from four mesothermal gold deposits in Siberia, Russian Federation. *Economic Geology* 93, 463−487.

Giannozzi, P., Baroni, S., Bonini, N., Calandra, M., Car, R., Cavazzoni, C., Ceresoli, D., Chiarotti, G.L., Cococcioni, M., Dabo, I., Dal Corso, A., de Gironcoli, S., Fabris, S., Fratesi, G., Gebauer, R., Gerstmann, U., Gougoussis, C., Kokalj, A., Lazzeri, M., Martin-Samos, L., Marzari, N., Mauri, F., Mazzarello, R., Paolini, S., Pasquarello, A., Paulatto, L., Sbraccia, C., Scandolo, S., Sclauzero, G., Seitsonen, A.P., Smogunov, A., Umari, P., Wentzcovitch, R.M. (2009) Quantum ESPRESSO: a modular and open-source software project for quantum simulations of materials. *Journal of Physics: Condensed Matter* 21, 395502.

Goldfarb, R.J., Baker, T., Dubé, B., Groves, D.I., Hart, C.J.R., Gosselin, P. (2005) Distribution, character, and genesis of gold deposits in metamorphic terrains. In: Hedenquist, J.W., Thompson, J.F.H., Goldfarb, R.J., Richards, J.P. (Eds.) *Economic Geology 100th Anniversary Volume*. Society of Economic Geologists, Littleton, 407−450.

Guda, S.A., Guda, A.A., Soldatov, M.A., Lomachenko, K.A., Bugaev, A.L., Lamberti, C., Gawelda, W., Bressler, C., Smolentsev, G., Soldatov, A.V., Joly, Y. (2015) Optimized finite difference method for the full-potential XANES simulations. Application to molecular adsorption geometries in MOFs and metal-ligand intersystem crossing transients: *Journal of Chemical Theory Computing* 11, 4512−4521.

Guillong, M., Meier, D.L., Allan, M.M., Heinrich, C.A., Yardley, B.W.D. (2008) SILLS: A MATLAB-based program for the reduction of laser ablation ICP-MS data of homogeneous materials and inclusions. In: Sylvester, P. (Ed.) *Laser Ablation ICP-MS in the Earth Sciences: Current Practices and Outstanding Issues*. Mineralogical Association of Canada Short Course Series, Vancouver BC, 40, 328–333.

Helgeson, H.C., Kirkham, D.H., Flowers, G.C. (1981) Theoretical prediction of the thermodynamic behavior of aqueous electrolytes at high pressures and temperatures: IV. Calculation of activity coefficients, osmotic coefficients and apparent molal and relative partial molal properties to 600 °C and 5 kb. *American Journal of Science* 281, 1249–1516.

Ishikawa, K., Isonage, T., Wakita, S., Suzuki, Y. (1995) Structure and electrical properties of Au_2S. *Solid State Ionics* 79, 60–66.

Johan, Z., Marcoux, E., Bonnemaison, M. (1989) Arsénopyrite aurifère: mode de substitution de Au dans la structure de FeAsS. *Comptes Rendus de l'Académie des Sciences de Paris* 308 II, 185–191.

Johnson, J.W., Oelkers, E.H., Helgeson, H.C. (1992) SUPCRT92: A software package for calculating the standard molal thermodynamic properties of minerals, gases, aqueous species, and reactions from 1 to 5000 bar and 0 to 1000 °C. *Computers & Geosciences* 18, 899–947. [Updated version based on a series of subsequent papers reporting HKF parameters for most ions and aqueous complexes is available online at http://geopig.asu.edu/index.html#.]

Joly, Y. (2001) X-ray absorption near-edge structure calculations beyond the muffin tin approximation. *Physical Reviews* B63, 125120.

Joly, Y. (2020) *FDMNES User's Guide*, accessed 4 April 2021, http://fdmnes.neel.cnrs.fr/.

Kelly, S.D., Hesterberg, D., Ravel, B. (2008) Analysis of soils and minerals using X-ray absorption spectroscopy. In Ulery, A.L., Drees, L.R. (Eds.) *Methods of Soil Analysis Part 5–Mineralogical Methods*. Soil Science Society of America, Madison, 387–463.

Kokh, M.A., Lopez, M., Gisquet, P., Lanzanova, A., Candaudap, F., Besson, P., Pokrovski, G.S. (2016) Combined effect of carbon dioxide and sulfur on vapor-liquid partitioning of metals in hydrothermal systems. *Geochimica et Cosmochimica Acta* 187, 311–333.

Kokh, M.A., Akinfiev, N.N., Pokrovski, G.S., Salvi, S., Guillaume, D. (2017) The role of carbon dioxide in the transport and fractionation of metals by geological fluids. *Geochimica et Cosmochimica Acta* 197, 433–466.

Kokh, M.A., Assayag, N., Mounic, S., Cartigny, P., Gurenko, A., Pokrovski, G.S. (2020) Multiple sulfur isotope fractionation in hydrothermal systems in the presence of radical ions and molecular sulfur. *Geochimica et Cosmochimica Acta* 285, 100–128.

Kolb, J., Dziggel, A., Bagas, L. (2015) Hypozonal lode gold deposits: A genetic concert based on a review of the New Consort, Hutti, Hira Buddini, Navachab, Nevoria and the Granites deposits. *Precambrian Research* 262, 20–44.

Kouzmanov, K., Pokrovski, G.S. (2012) Hydrothermal controls on metal distribution in Cu(-Au-Mo) porphyry systems. In: Hedenquist, J.W., Harris, M., Camus, F. (Eds.) *Geology and Genesis of Major Copper Deposits and Districts of the World: A Tribute to Richard H. Sillitoe*. Society of Economic Geologists Special Publication, Littleton, 16, 573–618.

Kovalchuk, E.V., Tagirov, B.R., Vikentyev, I.V., Chareev, D.A., Tyukova, E.E., Nikolsky, M.S., Borisovsky, S.E., Bortnikov, N.S. (2019) "Invisible" gold in synthetic and natural arsenopyrite crystals, Vorontsovka deposit, Northen Urals: *Russian Geology of Ore Deposits* 61, 447–468.

Kusebauch C., Gleeson S.A., Oelze M. (2019) Coupled partitioning of Au and As into pyrite controls the formation of giant Au deposits. *Science Advances* 5, eaav5891.

Le Pape, P., Blanchard, M., Juhin, A., Rueff, J.-P., Manoj, D., Morin, G., Cabaret, D. (2018) Local environment of arsenic in sulfide minerals: insights from high-resolution X-ray spectroscopies, and first-principles calculations at the As K-edge. *Journal of Analytical Atomic Spectrometry* 33, 2070–2082.

Le Vaillant, M., Barnes, S.J., Fiorentini, M.L., Barnes, S.-J., Bath, A., Miller, J. (2018) Platinum-group element and gold contents of arsenide and sulfarsenide minerals associated with Ni and Au deposits in Archean greenstone belts. *Mineralogical Magazine* 82, 625–647.

Llorens, I., Lahera, E., Del Net, W., Proux, O., Braillard, A., Hazemann, J.-L., Prat, A., Testemale, D., Dermigny, Q., Gelebart, F., Morand, M., Shukla, A., Bardou, N., Ulrich, O., Arnaud, S., Berar, J.-F., Boudet, N., Caillot, B., Chaurand, P., Rose, J., Doelsch, E., Martin, P., Solari, P.L. (2012) High energy resolution five-crystal spectrometer for high quality fluorescence and absorption measurements on an x-ray absorption spectroscopy beamline. *Review of Scientific Instruments* 83, 063104.

Marion, P.H., Regnard, J.-R., Wagner, F.E. (1986) Etude de l'état chimique de l'or dans les sulfures aurifères par spectroscopie Mössbauer de ^{197}Au. *Comptes Rendus de l'Académie des Sciences (Paris)* 302 II, 571–574.

Merkulova, M., Mathon, O., Glatzel, P., Rovezzi, M., Batanova, V., Marion, P., Boiron, M.-C., Manceau, A. (2019) Revealing the chemical form of 'invisible' gold in natural arsenian pyrite and arsenopyrite with high energy-resolution x-ray absorption spectroscopy. *ACS Earth and Space Chemistry* 3, 1905–1914.

Momma, K., Izumi, F. (2011) VESTA 3 for three-dimensional visualization of crystal, volumetric and morphology data. *Journal of Applied Crystallography* 44, 1272–1276.

Monkhorst, H.J., Pack, J.D. (1976) Special points for Brillouin-zone integrations. *Physical Review* B13, 5188–5192.

Morimoto, N., Clark, L.A. (1961) Arsenopyrite crystal-chemical relations. *American Mineralogist* 46, 1448–1468.

Mumin, A.H., Fleet, M.E., Chryssoilis, S.L. (1994) Gold mineralization in As-rich mesothermal gold ores of the Bogosu-Prestea mining district of the Ashanti Gold Belt, Ghana: remobilization of 'invisible gold'. *Mineralium Deposita* 29, 445–460.

Muntean, J.L. (2018) The Carlin gold system: applications to exploration in Nevada and beyond. *Reviews in Economic Geology* 20, 39–88.

Newville, M. (2001) IFEFFIT: interactive XAFS analysis and FEFF fitting. *Journal of Synchrotron Radiation* 8, 322–324.

Obertur, T., Weiser, T., Amanor, J.A., Chryssoulis, S.L. (1997) Mineralogical siting and distribution of gold in quartz veins and sulfide ores of the Ashanti mine and other deposits in the Ashanti belt of Ghana: genetic implications. *Mineralium Deposita* 32, 2–15.

Oelkers, E.H., Benezeth, P., Pokrovski, G.S. (2009) Thermodynamic databases for water-rock interaction. *Reviews in Mineralogy and Geochemistry* 70, 1–46.

Olson, S.F., Diakité, K., Ott, L., Guindo, A., Forb, C.R.B., Winer, N., Hanssen, E., Lay, N., Bradley, R., Pohl, D. (1992) Proterozoic Syama Gold Deposit, Mali West Africa. *Economic Geology* 84, 310–331.

Ondrus, P., Vavrin, I., Skala, R., Veselovsky, F. (2001) Low-temperature Ni-rich lollingite from Haje, Pibram, Czech Republic. Rietveld crystal structure refinement. *Neues Jahrbuch für Mineralogie - Monatshefte* 4, 169–185.

Pearce, N.J.G., Perkins, W.T., Westgate, J.A., Gorton, M.P., Jackson, S.E., Neal, C.R., Chenery, S.P. (1997) A compilation of new and published major and trace element data for NIST SRM 610 and NIST SMR 612 glass reference materials. *Geostandards Newsletter* 21, 115–144.

Parra-Avila, L.A., Bourassa, Y., Miller, J., Perrouty, S., Fiorentini, M.L., McCuaig, T.C. (2015) Age constraints of the Wassa and Benso mesothermal gold deposits, Ashanti Belt, Ghana, West Africa. *Journal of African Earth Sciences* 112, 524–535.

Perdew, J.P., Burke, K., Ernzerhof, M. (1996) Generalized gradient approximation made simple. *Physical Review Letters* 77, 3865–3868.

Perfetti, E., Pokrovski, G.S., Ballerat-Busserolles, K., Majer, V., Gibert, F. (2008) Densities and heat capacities of aqueous arsenious and arsenic acid solutions to 350 °C and 300 bar, and revised thermodynamic properties of $As(OH)_3^0$(aq), $AsO(OH)_3^0$(aq), and iron sulfarsenide minerals. *Geochimica et Cosmochimica Acta* 72, 713–731.

Pokrovski, G.S., Dubessy, J. (2015) Stability and abundance of the trisulfur radical ion S_3^- in hydrothermal fluids. *Earth and Planetary Science Letters* 411, 298–309.

Pokrovski, G.S., Kara, S., Roux, J. (2002a) Stability and solubility of arsenopyrite, FeAsS, in crustal fluids. *Geochimica et Cosmochimica Acta* 66, 2361–2378.

Pokrovski, G.S., Zakirov, I.V., Roux, J., Testemale, D., Hazemann, J.-L., Bychkov, A.Y., Golikova, G.V. (2002b) Experimental study of arsenic speciation in vapor phase to 500 °C: Implications for As transport and fractionation in low-density crustal fluids and volcanic gases. *Geochimica et Cosmochimica Acta* 66, 3453–3480.

Pokrovski, G.S., Tagirov, B.R., Schott, J., Hazemann, J.-L., Proux, O. (2009a) A new view on gold speciation in sulfur-bearing hydrothermal fluids from in-situ X-ray absorption spectroscopy and quantum-chemical modeling. *Geochimica et Cosmochimica Acta* 73, 5406–5427.

Pokrovski, G.S., Tagirov, B.R., Schott, J., Bazarkina, E.F., Hazemann, J.-L., Proux, O. (2009b) An in situ X-ray absorption spectroscopy study of gold-chloride complexing in hydrothermal fluids. *Chemical Geology* 259, 17–29.

Pokrovski, G.S., Akinfiev, N.N., Borisova, A.Y., Zotov, A.V., Kouzmanov, K. (2014) Gold speciation and transport in geological fluids: insights from experiments and physical-chemical modelling. In: Garofalo, P., Ripley, E. (Eds.) *Gold-Transporting Fluids in the Earth's Crust*. Geological Society of London Special Publication, London, 402, 9–70.

Pokrovski, G.S., Kokh, M.A., Guillaume, D., Borisova, A.Y., Gisquet, P., Hazemann, J.-L., Lahera, E., Del Net, W., Proux, O., Testemale, D., Haigis, V., Jonchière, R., Seitsonen, A.P., Ferlat, G., Vuilleumier, R., Saitta, A.M., Boiron, M.-C., Dubessy, J. (2015) Sulfur radical species form gold deposits on Earth. *Proceedings of the National Academy of Sciences* 112, 13484–13489.

Pokrovski, G.S., Kokh, M.A., Proux, O., Hazemann, J.-L., Bazarkina, E.F., Testemale, D., Escoda, C., Boiron, M.-C., Blanchard, M., Ajgouy, T., Gouy, S., de Parseval, P., Thibaut, M. (2019) The nature and partitioning of invisible gold in the pyrite-fluid system. *Ore Geology Reviews* 109, 545–563.

Proux, O., Biquard, X., Lahera, E., Menthonnex, J.-J., Prat, A., Ulrich, O., Soldo, Y., Trévisson, P., Kapoujvan, G., Perroux, G., Taunier, P., Grand, D., Jeantet, P., Deleglise, M., Roux, J.-P., Hazemann, J.-L. (2005) FAME: a new beamline for X-

ray absorption investigations of very diluted systems of environmental, material and biological interests. *Physica Scripta* T115, 970–973.

Proux, O., Lahera, E., Del Net, W., Kieffer, I., Rovezzi, M., Testemale, D., Irar, M., Thomas, S., Aguilar-Tapia, A., Bazarkina, E.F., Prat, A., Tella, M., Auffan, M., Rose, J., Hazemann, J.-L. (2017) High Energy Resolution Fluorescence Detected X-ray Absorption Spectroscopy: a new powerful structural tool in environmental biogeochemistry sciences. *Journal of Environmental Quality* 46, 1146–1157.

Qian, G., Brugger, J., Testemale, D., Skinner, W., Pring, A. (2013) Formation of As(II)-pyrite during experimental replacement of magnetite under hydrothermal conditions. *Geochimica et Cosmochimica Acta* 100, 1–10.

Ravel, B., Newville, M. (2005) ATHENA, ARTEMIS, HEPHAESTUS: data analysis for X-ray absorption spectroscopy using IFEFFIT. *Journal of Synchrotron Radiation* 12, 537–541.

Reich, M., Becker, U. (2006) First-principles calculations of the thermodynamic mixing properties of arsenic incorporation into pyrite and marcasite. *Chemical Geology* 225, 278–290.

Reich, M., Kesler, S.E., Utsunomiya, S., Palenik, C.S., Chryssoulis, S.L., Ewing, R.C. (2005) Solubility of gold in arsenian pyrite. *Geochimica et Cosmochimica Acta* 69, 2781–2796.

Robie, R.A., Hemingway, B.S. (1995) Thermodynamic properties of minerals and related substances at 298.15 K and 1 bar (10^5 Pascals) pressure and at higher temperatures. *U.S. Geological Survey Bulletin*, No. 2131, 461p.

Ruben, H., Zalkin, A., Faltens, M.O., Templeton, D.H. (1974) Crystal structure of sodium gold(I) thiosulfate dihydrate, $Na_3Au(S_2O_3)_2{\cdot}2H_2O$. *Inorganic Chemistry* 13, 1836–1839.

Rutzinger, D., Bartsch, C., Doerr, M., Rosner, H., Neu, V., Doert, Th., Ruck, M. (2010) Lattice distortions in layered type arsenides $LnTAs_2$ (*Ln* = La–Nd, Sm, Gd, Tb; T = Ag, Au): Crystal structures, electronic and magnetic properties. *Journal of Solid State Chemistry* 183, 510–520.

Sack, R.O., Ebel, D.S. (2006) Thermochemistry of sulfide mineral solutions. *Reviews in Mineralogy and Geochemistry* 61, 265–364.

Saunier, G., Pokrovski, G.S., Poitrasson, F. (2011) First experimental determination of iron isotope fractionation between hematite and aqueous solution at hydrothermal conditions. *Geochimica et Cosmochimica Acta* 75, 6629–6654.

Savage, K.S., Tingle, T.N., O'Day, P.A., Waychunas, G.A., Bird, D.K. (2000) Arsenic speciation in pyrite and secondary weathering phases, Mother Lode Gold District, Tuolumne County, California. *Applied Geochemistry* 15, 1219–1244.

Schutte, W.J., De Boer, J.L. (1988) Valence fluctuations in the incommensurately modulated structure of calaverite $AuTe_2$. *Acta Crystallographica* B44, 486–494.

Shvarov, Y.V. (2008) HCh: new potentialities for the thermodynamic simulation of geochemical systems offered by Windows. *Geochemistry International* 46, 834–839.

Shvarov, Y.V. (2015) A suite of programs, OptimA, OptimB, OptimC, and OptimS, compatible with the Unitherm database, for deriving the thermodynamic properties of aqueous species from solubility, potentiometry and spectroscopy measurements. *Applied Geochemistry* 55, 17–27.

Seryotkin, Y.V., Bakakin, V.V., Pal'yanova, G.A., Kokh, K.A. (2014) Synthesis and crystal structure of silver–gold sulfide AgAuS. Four-fold interpenetrated three-dimensional $[(Au,Ag)_{10}S_8]$-networks. *CrystEngComm* 16, 1675–1680.

Simon, G., Huang, H., Penner-Hahn, J.E., Kesler, S.E., Kao, L.-S. (1999) Oxidation state of gold and arsenic in gold-bearing arsenian pyrite. *American Mineralogist* 84, 1071–1079.

Suh, I.K., Ohta, H., Waseda, Y. (1988) High-temperature expansion of six metallic elements measured by dilatation method and X-ray diffraction. *Journal of Materials Science* 23, 757–760.

Sung, Y.-H., Brugger, J., Ciobanu, C.L., Pring, A., Skinner, W., Nugus, M. (2009) Invisible gold in arsenian pyrite and arsenopyrite from a multistage Archaean gold deposit: Sunrise Dam, Eastern Goldfields Province, Western Australia. *Mineralium Deposita* 44, 765–791.

Sverjensky, D.A., Shock, E.L., Helgeson, H.C. (1997) Prediction of the thermodynamic properties of aqueous metal complexes to 1000 °C and 5 kb. *Geochimica et Cosmochimica Acta* 61, 1359–1412.

Sverjensky, D.A., Harrison, B., Azzolini, D. (2014) Water in the deep Earth: The dielectric constant and the solubilities of quartz and corundum to 60 kb and 1200 °C. *Geochimica et Cosmochimica Acta* 129, 125–145.

Sylvester, P.J., Cabri, L.J., Tubrett, M.N., McMahon, G., Laflamme, J.H.G., Peregoedova, A. (2005) Synthesis and evaluation of a fused pyrrhotite standard reference material for platinum group element and gold analysis by laser ablation-ICPMS.

In: Törmänen, T.O., Alapieti, T.T. (Eds.) *10th International Platinum Symposium: Platinum-Group Elements: From Genesis to Beneficiation and Environmental Impact: Extended abstracts*. Geological Survey of Finland, Espoo, 16–20.

Tagirov, B.R., Trigub, A.L., Kvashnina, K.O., Shiryaev, A.A., Chareev, D.A., Nickolsky, M.S., Abramova, V.D., Kovalchuk, E.V. (2016) Covellite CuS as a matrix for ‘‘invisible” gold: X-ray spectroscopic study of the chemical state of Cu and Au in synthetic minerals. *Geochimica et Cosmochimica Acta* 191, 58–69.

Tarnocai, C.A., Hattori, K., Cabri, L.J. (1997) Invisible gold in sulfides from Campbell mine, Red Lake greenstone belt, Ontario: Evidence for mineralization during the peak metamorphism. *Canadian Mineralogist* 35, 805–815.

Tella, M., Pokrovski, G.S. (2009) Antimony(III) complexing with O-bearing organic ligands in aqueous solution: an X-ray absorption fine structure spectroscopy and solubility study. *Geochimica et Cosmochimica Acta* 73, 268–290.

Teo, B.K. (1986) *EXAFS: Basic Principles and Data Analysis*. Springer-Verlag, Berlin, Heidelberg, New York, Toronto.

Testemale, D., Brugger, J., Liu, W., Etschmann, B., Hazemann, J.-L. (2009) In-situ X-ray absorption study of iron (II) speciation in brines up to supercritical conditions. *Chemical Geology* 264, 295–310.

Trigub, A.L., Tagirov, B.R., Kvashnina, K.O., Chareev, D.A., Nickolsky, M.S., Shiryaev, A.A., Baranova, N.N., Kovalchuk, E.V., Mokhov, A.V. (2017) X-ray spectroscopy study of the chemical state of “invisible” Au in synthetic minerals in the Fe-As-S system. *American Mineralogist* 102, 1057–1065.

Traoré, D.Y., Siebenaller, L., Salvi, S., Béziat, D., Bouaré, M.L. (2016) Progressive gold mineralization along the Syama corridor, southern Mali (West Africa). *Ore Geology Reviews* 78, 586–598.

Vaughan, D.J., Rosso, K.M. (2006) Chemical bonding in sulfide minerals. *Reviews in Mineralogy and Geochemistry* 61, 231–264.

Velásquez, G., Béziat, D., Salvi, S., Siebenaller, L., Borisova, A.Y., Pokrovski, G.S., de Parseval, P. (2014) Formation and deformation of pyrite and implications for gold mineralization at the El Callao mining district, Venezuela. *Economic Geology* 109, 457–486.

Wilson, S.A., Ridley, W.I., Koenig, A.E. (2002) Development of sulfide calibration standards for the laser ablation inductively coupled plasma mass spectrometry technique. *Journal of Analytical Atomic Spectrometry* 17, 406–409.

Whitney, D.L., Evans, B.W. (2010) Abbreviations for names of rock-forming minerals. *American Mineralogist* 95, 185–187.

Wu, X., Delbove, F. (1989) Hydrothermal synthesis of gold-bearing arsenopyrite. *Economic Geology* 84, 2029–2032.

Xing, Y., Brugger, J., Tomkins, A., Shvarov, Y. (2019) Arsenic evolution as a tool for understanding formation of pyritic gold ores. *Geology* 47, 335–338.

Zotov, A.V., Kuzmin, N.N., Reukov, V.L., Tagirov, B.R. (2018) Stability of $AuCl_2^-$ from 25 to 1000 °C at pressures to 5000 bar and consequences for hydrothermal gold mobilization. *Minerals* 8, 286.